Applications of Laser-Plasma Acceleration

Svendsen, Kristoffer

2022

Document Version:
Publisher's PDF, also known as Version of record

Applications of Laser-Plasma Acceleration

KRISTOFFER SVENDSEN
FACULTY OF ENGINEERING | LUND UNIVERSITY

Printed by Media-Tryck, Lund 2022 NORDIC SWAN ECOLABEL 3041 0903

LUND UNIVERSITY
Faculty of Engineering, LTH
Department of Physics
Divison of Atomic Physics

ISBN (print): 978-91-8039-143-6
ISBN (pdf): 978-91-8039-144-3
ISSN: 0281-2762
Lund Reports on Atomic Physics, LRAP 578 (2022)

Applications of Laser-Plasma Acceleration

Kristoffer Svendsen

LUND
UNIVERSITY

Akademisk avhandling som för avläggande av teknologie doktorsexamen vid tekniska fakulteten vid Lunds universitet kommer att offentligen försvaras den 11 februari 2022, kl. 9.15 i Rydbergssalen, på Fysiska institutionen, Professorsgatan 1, Lund.
Fakultetsopponent: Prof. Jean Claude Kieffer
Institut national de la recherche scientifique, Kanada

Academic dissertation which, by due permission of the Faculty of Engineering at Lund University, will be publicly defended on February 11, 2022, at 9.15 a.m. in the Rydberg Lecture Hall, at the Department of Physics, Professorsgatan 1, Lund, for the degree of Doctor of Philosophy in Engineering.
Faculty opponent: Prof. Jean Claude Kieffer
Institut national de la recherche scientifique, Canada

Organization
LUND UNIVERSITY

Atomic Physics
Department of Physics
P.O. Box 118
SE-221 00 Lund
Sweden

Author(s)
Kristoffer Svendsen

Document name
DOCTORAL DISSERTATION

Date of disputation
11th February 2022

Sponsoring organization

Title and subtitle
Applications of Laser-Plasma Acceleration

Abstract

This thesis is dedicated to the investigation of laser-plasma particle acceleration concepts. Some of the work was focused on improving electron and proton acceleration for future applications, in terms of maximizing the particle energy and minimizing the divergence of the X-ray beams.

In laser wakefield acceleration, a very intense laser pulse ($> 10^{18}$ W/cm^2) is focused in a gas. The leading edge of the pulse is intense enough to ionize the gas, and the main part of the pulse interacts with a plasma. Under the action of the ponderomotive force, the intense laser pulse can expel plasma electrons and form a wake in the plasma that trails the laser pulse. This charge separation leads to the formation of an ion cavity that results in electromagnetic fields several orders of magnitude stronger than those in conventional accelerators, up to TV/m. Some electrons can be accelerated to several hundred MeV over distances of less than a cm by injecting them into the plasma wake.

There are also focusing forces inside the plasma wake, and the injected electrons will oscillate transversely about the optical axis, producing multi-keV betatron X-ray radiation. This radiation is directed along the optical axis with a low divergence of a few tens of mrad.

One application investigated in this work was the possibility of using laser-wakefield-accelerated electrons for very high-energy electron (VHEE) radiotherapy. High-energy electrons can reach deep tumours with limited scattering, and have a more suitable dose-depth profile than photon beams. In this work, a VHEE beam was focused inside a phantom using electromagnetic quadrupoles to mimic stereotactic radiotherapy.

The X-ray beam generated by LWFA was used to measure the equivalent path length and 3D liquid mass distribution in commercial fuel injectors by tomographic reconstruction. It was shown that the sensitivity (in terms of the detectable liquid mass) was comparable to that possible with large synchrotron facilities.

Furthermore, the LWFA X-ray source is suitable for phase contrast imaging (PCI), a technique very sensitive to changes in the refractive index. In-line PCI was used to perform a high-resolution tomography of a small lacewing.

Key words
laser wakefield acceleration, betatron radiation, X-rays, X-ray imaging, phase-contrast imaging, VHEE, radiotherapy, radiography, fuel injector, tomography, beam focusing, atomizing sprays, nanowires, liquid mass, target normal sheath acceleration, applications, charged particles

Classification system and/or index terms (if any)

Supplementary bibliographical information

Language
English

ISSN and key title
0281-2762, Lund Reports on Atomic Physics, LRAP 578

ISBN
print: 978-91-8039-143-6
pdf: 978-91-8039-144-3

Recipient's notes

Number of pages
173

Price

Security classification

Applications of Laser-Plasma Acceleration

Kristoffer Svendsen

Doctoral Thesis
2022

LUND
UNIVERSITY

Department of Physics
Faculty of Engineering
Lund University

Lund Reports on Atomic Physics, LRAP 578 (2022)
ISBN (print): 978-91-8039-143-6
ISBN (pdf): 978-91-8039-144-3

Printed in Sweden by Media-Tryck, Lund 2022

Abstract

This thesis is dedicated to the investigation of laser-plasma particle acceleration concepts. Some of the work was focused on improving electron and proton acceleration for future applications, in terms of maximizing the particle energy and minimizing the divergence of the X-ray beams.

In laser wakefield acceleration, a very intense laser pulse ($> 10^{18}$ W/cm^2) is focused in a gas. The leading edge of the pulse is intense enough to ionize the gas, and the main part of the pulse interacts with a plasma. Under the action of the ponderomotive force, the intense laser pulse can expel plasma electrons and form a wake in the plasma that trails the laser pulse. This charge separation leads to the formation of an ion cavity that results in electromagnetic fields several orders of magnitude stronger than those in conventional accelerators, up to TV/m. Some electrons can be accelerated to several hundred MeV over distances of less than a cm by injecting them into the plasma wake.

There are also focusing forces inside the plasma wake, and the injected electrons will oscillate transversely about the optical axis, producing multi-keV betatron X-ray radiation. This radiation is directed along the optical axis with a low divergence of a few tens of mrad.

One application investigated in this work was the possibility of using laser-wakefield-accelerated electrons for very high-energy electron (VHEE) radiotherapy. High-energy electrons can reach deep tumours with limited scattering, and have a more suitable dose-depth profile than photon beams. In this work, a VHEE beam was focused inside a phantom using electromagnetic quadrupoles to mimic stereotactic radiotherapy.

The X-ray beam generated by LWFA was used to measure the equivalent path length and 3D liquid mass distribution in commercial fuel injectors by tomographic reconstruction. It was shown that the sensitivity (in terms of the detectable liquid

mass) was comparable to that possible with large synchrotron facilities.

Furthermore, the LWFA X-ray source is suitable for phase contrast imaging (PCI), a technique very sensitive to changes in the refractive index. In-line PCI was used to perform a high-resolution tomography of a small lacewing.

Populärvetenskaplig sammanfattning

Denna avhandling beskriver förbättringen och användningen av en ny typ av partikelaccelerator, baserad på interaktionen mellan en kraftfull laser och ett plasma. Dessa acceleratorer kan uppnå samma partikelenergier som konventionella acceleratorer, men över avstånd 10 000 gånger kortare.

Konventionella partikelacceleratorer är baserade på elektriska fält i en metallisk struktur, och starkare fält kommer att resultera i en större acceleration, men om fältet är för starkt kan strukturen förstöras. Istället måste accelerationssträckan ökas för att få partiklar med högre energi. Det elektriska fältet är i det här fallet som en motor i en bil, en kraftfullare motor (ett starkare fält) gör att bilen kan accelerera till sin toppfart på kortare sträcka. I en laser-plasma-accelerator kan de elektriska fälten bli mycket starka eftersom det inte finns någon struktur som kan förstöras, och accelerationssträckan kan vara så kort som några millimeter istället för flera hundra meter som i en konventionell accelerator. Detta gör laser-plasma-acceleratorer mer utrymme- och kostnadseffektiva än konventionella acceleratorer. Tillgången på partikelacceleratorer är för närvarande mycket begränsad och utvecklingen av laser-plasma-acceleratorer kan lösa detta problem, vilket gynnar både forskarvärlden och allmänheten.

Ett av användningsområdena för partikelacceleratorer är att accelerera elektroner och sedan använda dessa för att producera röntgenstrålning. I konventionella acceleratorer görs detta genom att skicka elektronerna genom magnetfält. Fördelen med en laser-plasma-accelerator är att röntgenproduktionen sker naturligt inuti plasmat, och det finns inget behov av externa magneter.

Huvudfokus för det arbete som beskrivs i denna avhandling ligger på tre viktiga tillämpningar av laser-plasma-acceleration.

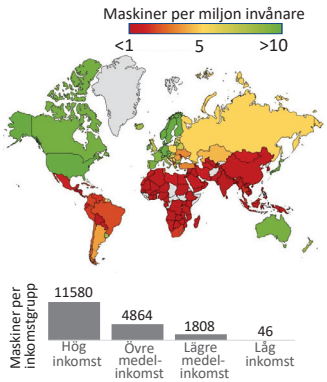

Figur 1. *Antal strålbehandlingsapparater per miljon invånare, tillsammans med antalet radioterapimaskiner för länder av olika inkomstnivå. Data från IAEA (DIRAC).*

Figur 2. *Tomografi av en spray från en bränsleinjektor.*

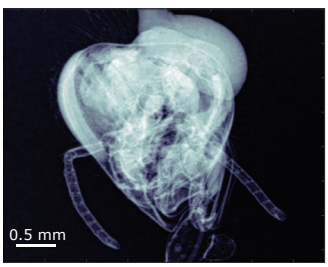

Figur 3. *Faskontrastbild av huvudet på ett bi.*

Strålbehandling - Tillgången av strålbehandling, som är en mycket viktig del av cancerbehandlingen, bestäms till stor del av ett lands ekonomiska status, som visas i Figur 1 med hjälp av data från IAEA (DIRAC). Framtida behandlingsanläggningar baserade på laser-plasma-acceleratorer skulle kunna öka tillgängligheten för denna typ av behandling. Dessutom kan strålbehandling med högenergielektroner vara en bättre behandlingsmetod än röntgen, som idag används för att behandla tumörer djupt inne i kroppen. Elektronenergierna i nuvarande terapimaskiner måste dock ökas med minst 400 % för att göra detta möjligt. Arbetet som presenteras i denna avhandling visar att en laser-plasma-accelerator har potential att användas för denna applikation, särskilt för att behandla små tumörer nära känsliga organ.

Röntgenbild - Cirka 90 % av bilarna på vägarna idag drivs av förbränningsmotorer. För att förbättra deras effektivitet och minska mängden föroreningar som produceras av motorererna måste vi kunna mäta hur bränslet fördelar sig när det sprutas in i cylindern. Studier som ingår i denna avhandling visar möjligheten att utföra högupplösta 3D-mätningar av bränslefördelningen med hjälp av en laser-plasma-accelerator. Figur 2 visar ett exempel på en bränsleinsprutningstomografi från detta arbete.

Faskontrastavbildning - Röntgenstrålar används ofta för att avbilda täta material omgivna av lättare material, såsom ben omgivet av vävnad. Om källan till röntgenstrålningen är tillräckligt liten och mycket intensiv, kan en teknik som kallas faskontrastavbildning användas för att avbilda material som har liknande densitet, såsom tumörer och frisk vävnad. I det arbete som beskrivs i denna avhandling visas det att en laser-plasma-accelerator är lämplig för denna uppgift då röntgenkällan är mycket liten, vanligtvis mindre än en mänsklig blodkropp. Ett exempel på en faskontrastbild, som visar huvudet på ett bi, visas i Figur 3.

Popular scientific summary

This thesis describes the improvement and use of a new type of particle accelerator based on the interaction between a powerful laser and a plasma. These accelerators can achieve the same particle energies as conventional accelerators, but over distances that are 10,000 times shorter.

Conventional particle accelerators are based on electric fields in a metallic structure, and stronger fields will result in greater acceleration, but if the field is too strong, the structure may be destroyed. Instead, the acceleration distance must be increased to obtain particles of higher energy. The electric field in this case is like the engine of a car, a more powerful engine (a stronger field) means that the car can accelerate to its top speed in a shorter distance. In a laser-plasma accelerator, on the other hand, the electric fields can become much stronger since there is no structure that can be destroyed, and the acceleration distance can be as short as a few millimetres instead of several hundreds of metres. This makes laser-plasma accelerators more space and cost efficient than conventional accelerators which may cost tens of millions of Euros. The availability of particle accelerators is currently very limited and the development of laser-plasma accelerators may solve this problem, benefitting both the research community and the general public.

One of the uses of particle accelerators is to accelerate electrons and then use these to produce bright X-rays. In conventional accelerators, this is done by sending the electrons through magnetic fields. The advantage of a laser-plasma accelerator is that X-ray production takes place naturally inside the plasma, and there is no need for external magnets.

The main focus of the work described in this thesis was on three important applications of a laser-plasma accelerator, as outlined below.

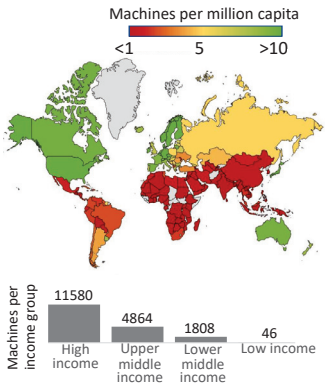

Figure 1. *Number of radiotherapy machines per million citizens, together with the number of machines in countries with different income level.*

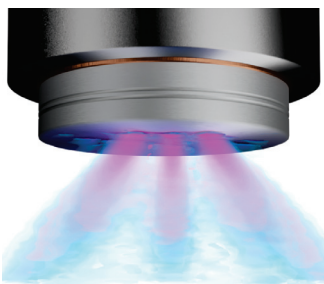

Figure 2. *Rendition of a tomographic reconstruction of a fuel injector spray.*

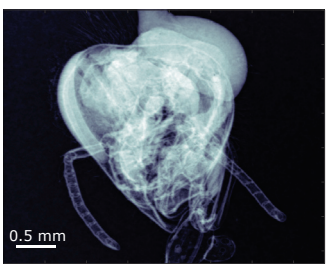

Figure 3. *Phase-contrast image of the head of a bee.*

Radiation therapy - The availability of radiation therapy, which is a very important part of cancer treatment, is largely determined by a country's economic status, as shown in Figure 1 using data from IAEA (DIRAC). Future treatment facilities based on laser-plasma accelerators could increase the availability of this kind of treatment. Furthermore, radiotherapy using high-energy electrons could be a better method of treatment than X-rays, which is today used to treat tumours deep in the body. However, the electron energies in current therapy machines must be increased by at least a factor of 4 to make this possible. The work presented in this thesis shows that a laser-plasma accelerator has the potential to be used for this application, especially to treat small tumours near sensitive organs.

X-ray imaging - About 90 % of the cars on the roads today are driven by combustion engines. In order to improve their efficiency and reduce the amount of pollution produced by these engines, we need to be able to measure how the fuel is distributed when it is injected into the cylinder. Studies included in this thesis demonstrate the possibility of performing high-resolution 3D measurements of the fuel distribution using a laser-plasma accelerator. Figure 2 shows an example of a fuel injection tomography from this work.

Phase-contrast imaging - X-rays are often used to image dense materials surrounded by lighter materials, such as bone surrounded by tissue. If the source of the X-rays is small enough and very bright, a technique known as phase-contrast imaging can be used to image materials that are similar in density, such as tumours and healthy tissue. In the work described in this thesis, it was shown that a laser-plasma accelerator is suitable for this task as the X-ray source is very small, usually smaller than a human blood cell. An example of a phase-contrast image, showing the head of a bee, is shown in Figure 3.

List of Publications

This thesis is based on the following publications, which are referred to by their Roman numerals.

I **Optimization of soft X-ray phase-contrast tomography using a laser wakefield accelerator**
K. Svendsen, I. Gallardo González, M. Hansson, J. Björklund Svensson, H. Ekerfelt, A. Persson and O. Lundh.
Optics Express, **26**, 33930 (2018).

II **A focused very high energy electron beam for fractionated stereotactic radiotherapy**
K. Svendsen, D. Guénot, J. Björklund Svensson, K. Petersson, A. Persson and O. Lundh.
Scientific Reports **11**, 5844 (2021).

III **Liquid mass distribution of transient sprays measured using laser-plasma-driven X-ray tomography**
D. Guénot, K. Svendsen, B. Lenhert, H. Ulrich, A. Persson, A. Permogorov, L. Zigan, M. Wensing, O. Lundh and E. Berrocal.
Submitted to Physical Review Applied.

IV **Simultaneous laser-driven X-ray and two-photon fluorescence imaging of atomizing sprays**
D. Guénot, K. Svendsen, J. Björklund Svensson, H. Ekerfelt, A. Persson and E. Berrocal.
Optica **7**, 131 (2020).

V **Low-divergence femtosecond X-ray pulses from a passive plasma lens**
J. Björklund Svensson, D. Guénot, J. Ferri, H. Ekerfelt, I. Gallardo González, A. Persson, K. Svendsen, L. Veisz and O. Lundh.
Nature Physics **17**, 639 (2021).

VI **Enhanced laser-driven proton acceleration using nanowire targets**
S. Vallières, M. Salvadori, A. Permogorov, G. Cantono, K. Svendsen, Z. Chen, S. Sun, F. Consoli, E. d´Humières, C.-G. Wahlström and P. Antici.
Scientific Reports **11**, 2226 (2021).

All papers are reproduced with permission of their respective publishers.

Other publications by the author not included in this thesis:

Analysis of liquid spray structures using two-photon fluorescence laser sheet imaging
H. Ulrich, B. Lenhert, D. Guénot, K. Svendsen, O. Lundh, S. Will, M. Wensing, E. Berrocal and L. Zigan.
ICLASS **1**, 402 (2021).

Dosimetry in environments surrounding a laser-plasma accelerator
O. Lundh, K. Svendsen, Y. Ranebo.
Svenska Strålsäkerhetsmyndigheten **04**, 2000-0456 (2019).

Abbreviations

VHEE	Very High Energy Electron
ASE	Amplified Spontaneous Emission
CPA	Chirped Pulse Amplification
OAP	Off-Axis Parabolic mirror
FWHM	Full Width at Half Maximum
LWFA	Laser-Wakefield Acceleration
OBI	Over-the-Barrier Ionization
PCI	Phase-Contrast Imaging
PIC	Particle-In-Cell
TNSA	Target Normal Sheath Acceleration
MTLF	Multi-Terawatt Laser Facility
DPM	Double Plasma Mirror
MPI	Multi-Photon Ionization
TI	Tunnel Ionization
EMQ	ElectroMagnetic Quadrupole
SNR	Signal-to-Noise Ratio
2-p LIF	2-Photon Light Induced Fluorescence
TCP	Tumour Control Probability
NTCP	Normal Tissue Complication Probability
CCD	Charge-Coupled Device

Contents

Papers

Chapter 1

Introduction

1.1 Applications of accelerated particles

There are more than 30,000 particle accelerators worldwide (IAEA) and several important discoveries have been made possible thanks to these machines. The most well-known discovery in recent times is probably that of the Higgs Boson. However, 59 new particles have been discovered at the Large Hadron Collider (LHC) alone, over the past 13 years, which has helped us confirm the Standard Model, the best theory of the universe to date. Particle accelerators have also made synchrotron facilities available. These generate very bright X-ray beams, and are used in several fields of research such as the life sciences and materials science. Despite their importance, accelerators dedicated to research constitute only about 3 % of the total number of accelerators; the other 97 % are being used in industry and hospitals. Accelerators are used to produce radioactive isotopes for medical applications such as PET scanning, and in cancer treatment in the form of radiotherapy. In the materials industry, accelerators are used to cross-link polymers, in order to change their material properties, for example, to increase their heat resistance, tensile strength or insulation properties. Examples of this are the manufacture of shrink-wrap, hardening of car tyre rubber, and the insulation of wire tubing. Electron beams produced by accelerators are used in electron beam welding, ion-implantation in semi-conductors, for sterilizing equipment and in food preservation. Accelerators are also used to produce X-rays that are used in medical facilities, security screening at airports and other sensitive facilities.

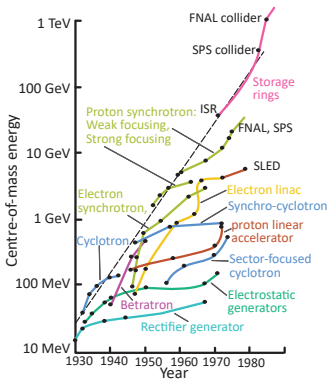

Figure 1.1. *Livingston chart showing the collision energy achieved during the early years of particle accelerator development.*

1.2 A history of particle acceleration

One of the first reasons for accelerating particles was to "split the atom", following the experiments performed by Rutherford in 1917, in which he performed the first nuclear reaction with natural alpha particles. One of the first accelerators was constructed a few years later in 1932, the Cockcroft-Walton generator, which could accelerate protons to 400 keV allowing the lithium atom to be split for the first time. The Van der Graaff electrostatic generator was developed in parallel. This concept was later developed into the tandem accelerator, which could generate potentials up to 10 MV.

The limitations of static fields were discovered early on, and a different approach was suggested by the Swedish scientist Gustav Ising in 1924. His design used alternating electromagnetic fields instead of static fields, and is the technique on which linear particle accelerators are based today. The longitudinal fields in each cavity oscillate between positive and negative electric fields. As the velocity of the particles increases, the distance between each cavity must be increased to keep the particles in phase with the accelerating field, or more conveniently, the frequency of the electromagnetic field is increased. Ising's original design had no enclosed cavities (simply exposed cylindrical electrodes), and this design element was a later addition to minimize the losses that result from increasing the frequency of the electromagnetic field.

Seven years later, in 1931, the first cyclotron is demonstrated by accelerating protons to 80 keV. The cyclotron accelerates particles using alternating electric fields in a spiral path inside a static magnetic field. Just a few weeks after the first atom was split using the Cockcroft-Walton generator, Ernest O. Lawrence uses the cyclotron to also split the atom. In the cyclotron, the radio waves were maintained at the same frequency, which limited the energy gain as the particles become out of phase with the field. This problem was solved with the introduction of the synchrocyclotron in which the radio wave frequency is varied to account for relativistic effects and the first synchrocyclotron was inaugurated in 1945.

In both cyclotrons and synchrocyclotrons, the force exerted by the radio waves also defocuses the beam transversely. In order to reach higher energies the beam must thus be focused. The first attempt to do this was made using a weak radial gradient and heralded the birth of the synchrotron. This was followed by alternating gradient focusing, which could be much stronger and led to the matrix formulation of magnetic elements that is still used today.

As early as 1923, Rolf Widerøe sketched a design in his notebook. This consisted of two magnetic poles such that the particle is accelerated in a circle via a varying magnetic field and is now known as the betatron accelerator. Widerøe built a prototype in 1927 but it did not work and he never published his idea. Several years later, Donald William Kerst had the same idea as Widerøe and in 1940 he built the first working betatron accelerator. In 1950 he was able to accelerate electrons to an energy of 300 MeV. These accelerators were not further developed but they demonstrated that electrons performing oscillatory motion generated radiation. This is why it is today called betatron radiation and is the foundation of the radiation generated at modern synchrotron facilities.

Figure 1.1 shows a Livingston chart of the different accelerator technologies and the centre-of-mass energy achieved during the early years [1]. It should be noted that in the case of colliders where two particle beams are present, the centre-of-mass energy is the sum of the beam energies. This illustrates in a clear way how different technologies have been developed and then stagnated over time, only to be replaced by more modern solutions.

1.3 Plasma-based accelerators

One of the problems associated with the radio-frequency-based accelerators described in the previous section is that they are limited by the field strength that can be sustained in the accelerating structure. If the fields are too high (typically $50 - 100$ MV/m) this will result in electrical arcing which can damage the structure. In 1956, Budker and Veksler suggested using a plasma to accelerate the particles which could, theoretically, support much stronger accelerating fields. The theory of plasma wakefield acceleration was later developed in 1979 by Tajima and Dawson [2], who suggested using a laser to produce a plasma wave. The plasma wave was intended to act as an accelerator cavity, with field strengths reaching several GV/m. However, the lasers available at that time were not powerful enough to prove this theory. In 1985, Strickland and Mourou demonstrated chirped pulse amplification (CPA) [3], for which they were awarded the Nobel prize in 2018. This made it possible to achieve the power required for laser-driven wakefield acceleration.

Investigations of the possibility of using a particle beam as a driver instead of a laser pulse started at the beginning of the 1990s. Figure 1.2 shows an updated Livingston plot, including

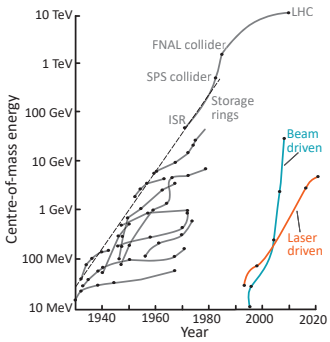

Figure 1.2. *Livingston chart including the Large Hadron Collider, beam driven wakefield acceleration and laser wakefield acceleration*

the Large Hadron Collider and some major wakefield experiments [4–8], both particle beam driven and laser driven. The maximum collision energy achieved with plasma acceleration has increased rapidly in recent years, while the energy reached in colliders has tended to stagnate. The increase in maximum beam energy for laser wakefield acceleration (LWFA) has been smaller. However, some claim that the advantage of such systems lies in the relatively small scale of these accelerators, and they could improve or replace currently employed accelerators in many of the applications mentioned in Section 1.1.

For example, a 45 TW laser can fit on a 2×4 m^2 table and accelerate electrons to more than 200 MeV over a distance of a few millimetres. To achieve the same energy with a radio-frequency-based linear accelerator would require a tunnel tens of metres long, and several metres wide to house all the equipment. For example, at the NSLS2 accelerator at the Brookhaven National Laboratory in the USA, a 60 m long and 4 m wide tunnel is used to host the linear accelerator that can accelerate electrons to 200 MeV.

1.4 Thesis outline

Chapter 2 describes the equipment and set-ups used in the experiments presented in this thesis. The laser system is also described, together with radiation safety at the Lund multi-terawatt laser facility (MTLF).

Chapter 3 describes the acceleration mechanisms in laser wakefield acceleration. It also introduces the concepts of plasmas and ionization, ending with a section on electron beam focusing and the application of very high energy electron radiation therapy.

Chapter 4 describes the generation of betatron X-rays in a wakefield accelerator along with methods for characterising the X-ray source size and spectrum. It ends by describing some applications of laser-plasma generated betatron X-rays, such as radiography, phase-contrast imaging and X-ray tomography.

The principle of target-normal sheath acceleration (TNSA) for ion acceleration is discussed in Chapter 5, together with a discussion on the use of ions for radiotherapy and possible ways of improving the ion source to achieve this goal.

The thesis ends with a discussion and outlook in Chapter 6 on the applications covered here.

Chapter 2

The Lund Multi-Terawatt Laser Facility

2.1 High-power lasers

The power of a laser is defined by the amount of energy it delivers per unit of time $P = E/\tau$, where τ is the pulse duration. Two different categories of high-power lasers can be distinguished. The first includes lasers with high average power, i.e. the energy content is very high over a long time. The second type is lasers with high peak power, which were used in the work described in this thesis. In a high-peak-power laser, the aim is to significantly reduce the pulse duration, so that all the energy is concentrated in time. This allows the generation of laser pulses with a very high peak intensity, as the intensity is $I = 2P/\pi w^2$, where w is the beam waist. These are the intensities needed for laser wakefield acceleration.

Mode locking is crucial to achieve ultra-short laser pulses. An optical cavity can support a large number of different longitudinal modes, which will oscillate independently of each other. Mode locking makes these independent modes oscillate in phase, such that they interfere constructively, producing a single, short high-amplitude pulse, as illustrated in Figure 2.1. The more modes that can be combined, the narrower the pulse will be in the time domain. For a beam with a Gaussian temporal profile the pulse duration is $\tau = \frac{0.44}{N\Delta\omega}$, where N is the number of modes, and $\Delta\omega$ is the frequency separation between each mode. It is therefore desirable to find a gain medium with a very large gain bandwidth that can support many modes. For example, a crystal of sapphire doped with

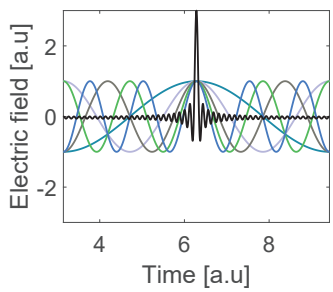

Figure 2.1. *Illustration of mode locking, showing the constructive interference between 50 modes (black) along with the first 5 modes (green and blue) with normalised amplitudes.*

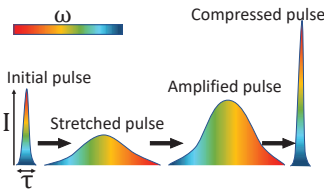

Figure 2.2. *Working principle of chirped pulse amplification. An initial short pulse is stretched in time to a longer duration, i.e. different frequencies, ω, arrive at different times. The stretched pulse (which now has a reduced intensity) is amplified and then compressed into a short, high-intensity pulse.*

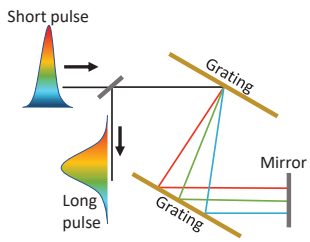

Figure 2.3. *An initially short pulse enters from the left through a beam splitter. As the grating diffracts frequencies at different angles, lower frequencies (red) will travel a longer path length than the higher frequencies (blue), introducing a linear chirp.*

titanium ions ($Ti : Al_2O_3$), commonly called Ti:sapphire, can support tens of thousands of modes. Achieving mode locking in practice means only allowing modes that are in phase with each other to survive, while all other modes are suppressed. Various methods can be used to do this, categorized as active, passive or hybrid mode locking. The shortest pulses are produced by passive mode locking, and this is also the most common method.

All methods of passive mode locking are based on the concept that cavity losses are intensity dependent. At the start of lasing, a large number of modes will be present, distributed randomly in phase, producing a continuous beam. Some of these modes will, by chance, be in phase, and thus have a slightly higher intensity. As a higher intensity results in smaller losses and, in particular, the gain is higher than the loss, these modes will be amplified and survive. Modes that are out of phase will experience losses that are greater than the gain, and thus be suppressed.

One way of achieving an intensity-dependent cavity loss is by the Kerr lens effect, known as Kerr lens mode locking. Kerr lensing is a non-linear effect where the refractive index changes depending on the laser intensity inside an optical medium. A spatially Gaussian pulse will experience a Gaussian refractive index and be focused. It is now only necessary to intentionally suppress any unfocused parts of the beam. This can be done by constructing the cavity in such a way that it only supports a beam of a certain divergence, by adapting the curvature of the end mirrors or by introducing an aperture. Another, more common, method is to pump a concentrated part of the medium. As the unfocused beam will have a smaller overlap with the pumped medium, the gain will be less while the focused, high-intensity beam will experience a high gain.

Pulses in the femtosecond regime can be obtained by mode locking. However, since the peak power of the laser is drastically increased by mode locking, any optical equipment in the beam that is not highly reflective might be damaged. For this reason, CPA is necessary to achieve today's high-power lasers. The principle of CPA is illustrated in Figure 2.2. The first step is to stretch the pulse in time. In high-power lasers, this is done using optical gratings to introduce a chromatic dispersion. This results in a linear chirp, i.e. the frequency components will be spread out in time (see Figure 2.3). A positive chirp (also known as up-chirp), corresponds to the group velocity decreasing as the frequency increases, i.e. the low optical frequencies will be at the leading edge of the pulse. The illustration in Figure 2.3 shows a case that introduces negative

chirp as the high frequencies (blue) have a shorter path length and will afterwards be at the leading edge of the pulse.

After the pulse has been amplified, it must be compressed to reduce the pulse duration. This corresponds to introducing an equal amount of opposite chirp. If the pulse is stretched by introducing a negative chirp, an equal amount of positive chirp will have to be introduced to compress the pulse. A positive chirp can be obtained by adding a telescope between the two gratings in Figure 2.3.

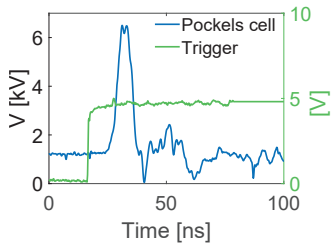

Figure 2.4. *The voltage V that is sent to a Pockels cell (blue) by the trigger pulse (green). A feedback loop adjusts the trigger signal delay so that the Pockels cell voltage matches the optical pulse in time.*

2.2 The Lund multi-terawatt laser

All the experiments described in this thesis were carried out at the Lund multi-terawatt laser facility (MTLF). This Ti:sapphire laser has been continuously upgraded for over two decades, and currently has a peak power of about 50 TW, with a pulse duration of $\sim$ 30 fs and an energy of 1.5 J. The laser is commonly operated at a slightly lower energy to spare the optical equipment, and more typical operating conditions is a pulse duration of 37 fs and a pulse energy of 1.3 J.

A mode locked oscillator generates a 5 nJ, 80 MHz pulse train with a central wavelength of 800 nm and a bandwidth of about 40 nm. A Pockels cell is used to extract pulses at 10 Hz, which are further amplified in a pre-amplifier to 1 μJ, and then stretched to about $\sim$ 400 ps using two gratings. The electro-optical crystal in the Pockels cell requires a high voltage to be applied in a very short time, which is stabilized by a trigger from a feedback loop that corrects for any drift in the timing (see Figure 2.4). Immediately before the stretcher, the spectral phase of the pulse is optimized by an acousto-optic modulator, together with compensation for gain narrowing.

The selected pulses are amplified in a regenerative amplifier and extracted at an energy of approximately 5 mJ. In order to minimize the amplified spontaneous emission or any pre-pulses, two Pockels cells are used as a polarization gate as these are only open for a few ns. The pulse is further amplified in a multi-pass amplifier, passing through the gain medium 5 times, after which the pulse energy is about 400 mJ.

The pulse is focused through a spatial filter with a 450 μm pinhole to obtain a clean and nearly Gaussian spatial profile. At this stage, the pulse is split and directed to two different experimental halls. The beam used in the work described in this thesis is amplified one last time in a 6-pass amplifier. The gain medium is a Ti:sapphire crystal cooled to -180 °C which is optically pumped by five frequency-doubled Nd:YAG lasers.

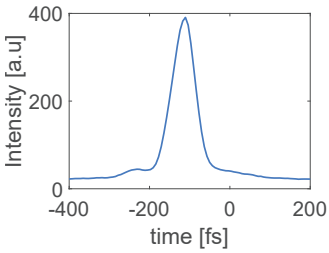

Figure 2.5. *Second-harmonic intensity profile from the autocorrelator, multiplied by the deconvolution factor, resulting in a pulse duration of 32 fs full-width-half-maximum (FWHM).*

After this final amplification the pulse can reach an energy of 2.5 J.

The beam is then spatially expanded by a factor ~ 6 to 65 mm in diameter, and compressed by two gratings to a pulse duration of ~ 30 fs. At this point the beam is too intense to propagate in air and is kept in vacuum (10^{-6} mbar). A mirror can be inserted to extract the attenuated beam for diagnostics, such as pulse duration measurements using second- and third-order autocorrelators. The second-order autocorrelator splits the pulse, after which the two pulses are recombined at an angle in a non-linear crystal to generate a second-order harmonic signal. The width of the pulse corresponds to the product of a deconvolution factor depending on the pulse shape, and the harmonic signal (see Figure 2.5). A third-order autocorrelator is used to measure the laser pulse contrast (see Figure 2.7). The laser pulse contrast is discussed in the next section.

The beam wavefront is optimized by a deformable mirror to minimize aberrations and to achieve an optimal focal spot in the experimental chamber. Due to a number of mirrors in the compressor and the transport beamline from the deformable mirror to the target, the transmission from the final amplification to the target area is normally $\sim$ 60 %. The beam can be sent to one of two interaction chambers. The first is the chamber used for ion acceleration, which is preceded by a double plasma mirror (DPM), while the second is the electron acceleration chamber.

2.3 Double plasma mirror

The laser pulse contrast is an important parameter in laser wakefield acceleration as a low contrast, i.e. a high amplified spontaneous emission (ASE) pedestal or pre-pulses, can affect the electron beam pointing stability and energy stability. For electron acceleration, a contrast ratio of about $I_{min}/I_{max} = 10^{-8}$ is generally sufficient for a stable electron beam [9] and can be achieved in most laser systems. However, for a more efficient interaction with solid targets (ion acceleration), the laser contrast needs to be improved further as a pre-pulse or ASE pedestal can significantly alter the initial conditions by forming a pre-plasma, deforming the target, or if strong enough, destroying the target before the main pulse arrives. The target is usually a foil, the thickness of which is generally limited to that which can withstand the ASE intensity, typically a few μm. However, as discussed in Section 5.1, thinner targets can accelerate particles to higher energies. This

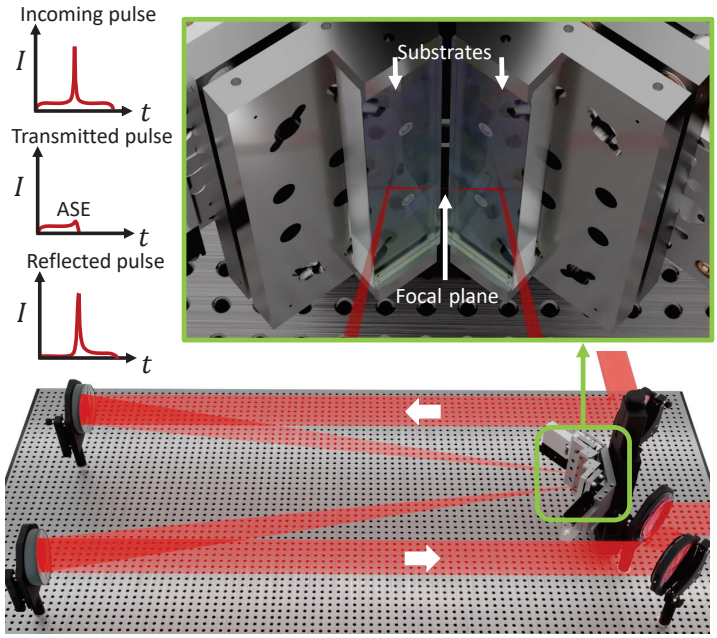

Figure 2.6. *A schematic view of the DPM. Top left: the incoming pulse with an ASE pedestal. Under ideal conditions, the ASE will be transmitted and discarded, while the DPM will activate at the leading edge of the pulse to reflect as much as possible of the main pulse.*

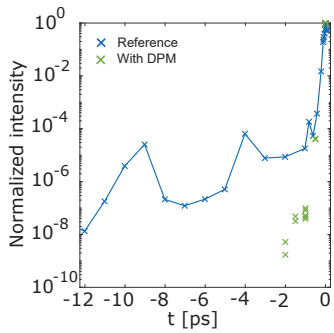

Figure 2.7. *Comparison of the laser pulse contrast with (green) and without (blue) a DPM.*

motivates the improvement of the laser pulse contrast to allow the use of even thinner targets.

A DPM is utilized to further improve the laser pulse contrast for ion acceleration at the Lund MTLF. The S-polarized laser pulse is focused by an $f/13$ off-axis parabolic mirror (OAP) between two anti-reflective-coated glass substrates, as illustrated in Figure 2.6. The reflectivity of the glass substrate is highly dependent on the incident laser intensity. At low intensities the substrate is transparent, while at intensities $> 10^{14}$ W/cm^2 [10] the substrate rapidly ionizes and forms an over-dense, reflective, plasma (see Section 3.2). The plasma mirror is activated by the leading edge of the pulse and remains active for a few ps but the reflectivity falls over a few hundred fs [11, 12] as the plasma starts to expand. The main pulse is thus reflected, while the preceding ASE pedestal and any prepulses are transmitted through the substrate and discarded. This process is repeated once more at the second substrate, which improves the contrast even further. The pulse is then collimated with an identical $f/13$ OAP and sent to the ion

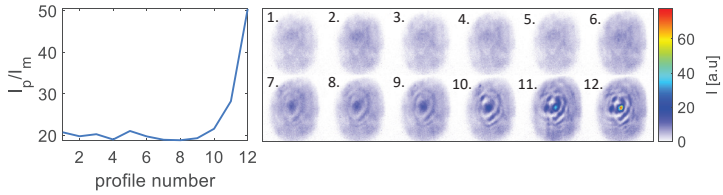

Figure 2.8. *Left: the peak intensity, I_p, normalized to the mean intensity, I_m, of the beam profile for each profile shown on the right. The fluence on the substrate was increased for each profile (numbered 1-12), and the beam profile was imaged after being re-collimated by the second OAP. Higher fluence results in earlier activation of the DPM which significantly reduces the quality of the output beam.*

acceleration chamber. It should be noted that, after the laser pulse has been reflected by the substrates, the substrate surface at the point of interaction is destroyed. To have a clean surface for the next pulse the substrates have to be moved, while maintaining the distance between the substrate surface and focal plane to have the same fluence at the substrate.

One of the main challenges with a DPM is to optimize the time of activation. This is done by controlling the fluence on the substrate by varying the laser spot size at the substrates. Ideally, the plasma mirror should be activated immediately before the main pulse arrives, but if the fluence is too low it will only reflect part of the main pulse. If the fluence is too high, the plasma mirror will be activated too early, resulting in a non-flat surface as the plasma has time to expand. This can distort the laser pulse wavefront and degrade the beam quality. This, in turn, will result in a non-optimal focal spot in the interaction chamber along with the generation of intensity hot spots in the transverse beam profile that can damage the optics in the beamline (see Figure 2.8).

Under optimal conditions, the DPM will increase the contrast by 2 orders of magnitude (see Figure 2.7), with a reduction in laser pulse energy of $\sim$ 50 %. This allows for the use of thinner foils, which increases the maximum ion energy, as discussed in Section 5.1.

2.4 Electron acceleration chamber

The typical set-up for accelerating electrons (laser wakefield acceleration) is depicted in Figure 2.9. As the laser beam enters the chamber, a small leak is extracted through a dielectric mirror to image the near-field and far-field of the beam (not shown

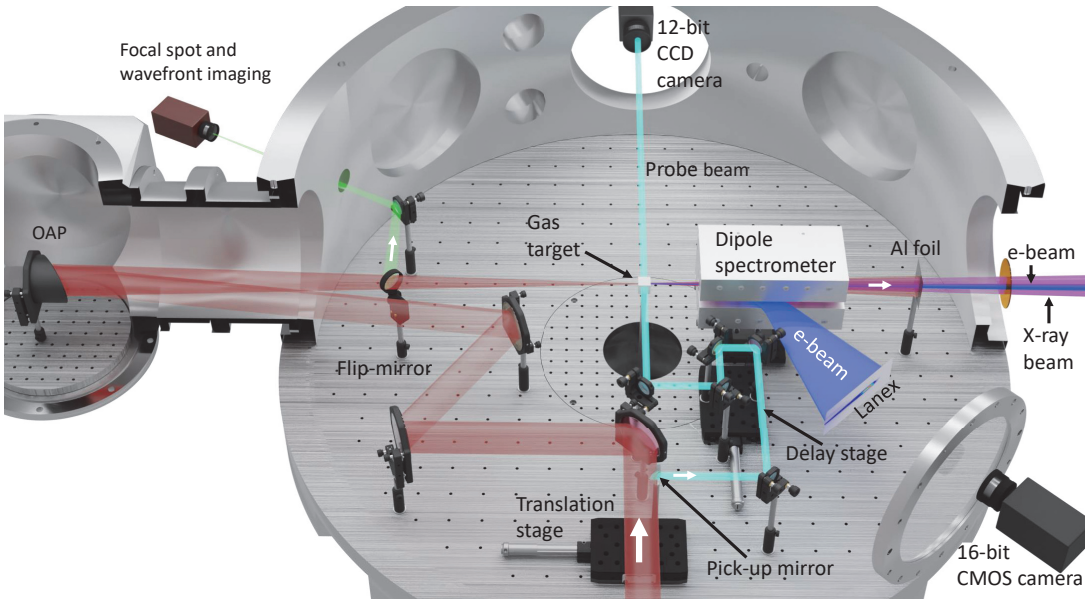

Figure 2.9. *Typical set-up in the electron acceleration chamber.*

here). For experiments requiring highly accurate beam pointing, this can be monitored and corrected in a PID-regulated feedback-loop using a piezo-controlled mirror positioned right after the deformable mirror. The main beam is focused to a spot size of 12 μm full-width-half-maximum (FWHM) with a peak intensity of 5×10^{18} W/cm^2 using an $f/12$ OAP. Figure 2.10 shows a typical focal spot.

A small pick-up mirror takes a small part from the edge of the beam ($\sim$ 8 mJ), which is used as a transverse probe to image the plasma channel.

A silver mirror on a motorized flip-mount (flip-mirror) can be inserted in the attenuated beam path after the OAP to image the focal spot and the wavefront. The focal spot is imaged using a 12-bit charge-coupled device (CCD) camera while the wavefront is analysed using a wavefront sensor (Phasics SID4). The wavefront is optimized in a feedback-loop using the wavefront sensor and the deformable mirror.

2.4.1 Gas targets

Two types of gas targets were used in the studies presented in this thesis. A 6 mm long windowless gas cell was used in

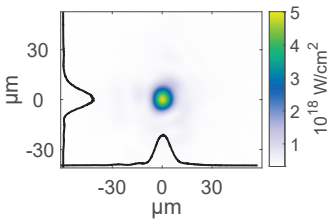

Figure 2.10. *Laser focal spot with a focal spot size of 12 μm (FWHM) inside the electron acceleration chamber.*

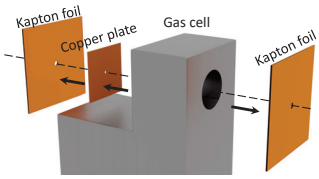

Figure 2.11. *Illustration of the gas cell used in the experiment described in Papers I, III. The laser pulse enters from the right.*

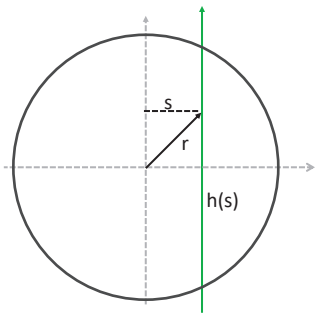

Figure 2.12. *Geometrical illustration of the Abel transform.*

the studies described in Papers I and III, depicted in Figure 2.11. The size of the entrance and exit of a gas cell is generally of importance, as a large entrance or exit opening will result in a significant longitudinal density gradient due to the gas leakage. As the laser pulse refracts in the gas it also tends to ablate the edges of the exit opening significantly, widening it. For this reason, the front and back surface of this cell are covered with a thin Kapton foil and a thicker copper plate at the exit which are regularly replaced. The Kapton foil and copper plate are carefully aligned and perforated to allow the laser pulse to enter without clipping. In the studies described in Papers II, IV and V, a supersonic gas jet was used instead of a cell, which has the advantage of easier alignment and a sharp, almost top-hat, density profile (see Figure 2.13). It also allows for shock-front injection as it requires a sharp density gradient which can be generated by inserting a razor blade in the supersonic jet (see Section 3.7.3 and Paper V).

Gas jet characterization

The plasma density is of great importance in electron acceleration as it depends on the gas density, which is discussed further in Chapter 3. However, measurements typically provide information on the integrated, or projected, gas density while the density along the optical axis is of main interest. This can be obtained by the Abel transform if the density is radially symmetric. The Abel transform:

$$f(r) = -\frac{1}{\pi}\int_r^R \frac{dh(s)}{ds}\cdot\frac{1}{\sqrt{s^2-r^2}}ds \qquad (2.1)$$

is closely related to the Radon transform, which is discussed in Section 4.4. The radially symmetric function $f(r)$ is reconstructed from $h(s)$, which is the projected value, i.e. the line integral a distance s from the centre of symmetry, as illustrated in Figure 2.12. There are several methods of solving this numerically but they are generally very sensitive to noisy data. It should be noted that noisy projection data should not be smoothed prior to applying the Abel transform as this reduces the reconstruction accuracy. One of the more robust methods, especially when dealing with noisy projection data, is a Fourier-based method [13] that was used in preparation for the study described in Paper V to obtain estimates on the electron densities from a supersonic gas jet for use in supporting simulations. Measurements were recorded using a helium-neon laser and wavefront sensor (Phasics SID4), using a reference

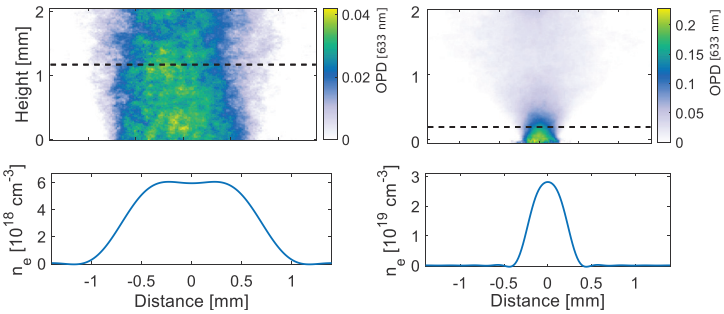

Figure 2.13. *Above: Measured optical path difference (OPD) together with the calculated electron densities (below) using the Abel transform and Equation 2.3 of a supersonic, 1.5 mm wide gas jet (left) and a subsonic 400 μm wide gas jet (right). The OPD is given in units of the probing wavelength (633 nm). The location of the Abel transform is indicated by the dashed lines. During the electron density calculation, complete ionization of the gas was assumed.*

image without any gas present. The data obtained show the optical path difference (see Figure 2.13).

As there is no way of accurately estimating the error introduced by asymmetric data [13] (as stated above, the Abel transform assumes radial symmetry), all projections were made symmetrical by taking the average of the projection and the inverted projection.

Once the optical path difference is known, the molecular number density can be calculated. The relative permittivity of a material, ϵ_r, can be related to the particle density, N_p, according to the Clausius-Mossoti equation:

$$\frac{\epsilon_r - 1}{\epsilon_r + 2} = \frac{N_p \alpha_p}{3\epsilon_0} \tag{2.2}$$

which depends on the polarizability, α_p, of the atoms. This can be rewritten using Maxwell's relation, $n^2 = \epsilon_r$ and at non-extreme pressure the refractive index will be $n \approx 1$ and Equation 2.2 simplifies to:

$$N_p = \frac{2\Delta n}{\alpha_p} \tag{2.3}$$

where Δn is the difference between the refractive index and a reference (vacuum in this case). Figure 2.13 shows the calculated electron density, assuming complete ionization, for a supersonic gas jet and a smaller subsonic gas jet (Paper V). As He gas has a very low refractive index, another monatomic gas,

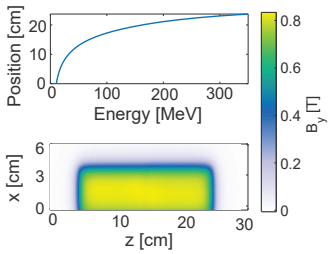

Figure 2.14. *Above: dispersion curve of the large dipole spectrometer, showing the position on the scintillating screen as a function of energy. Below: a top view of the measured magnetic field.*

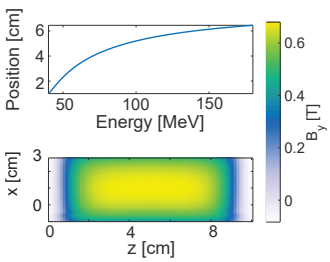

Figure 2.15. *Above: dispersion curve of the small dipole spectrometer together with a top view of the measured magnetic field (below). The dispersion shows the lateral position in mm from the optical axis 10 cm behind the dipole.*

Ar, was used in this measurement to increase the sensitivity as Ar has a higher refractive index.

2.4.2 Electron beam spectrometer

To obtain the electron energy spectrum, the accelerated electrons are sent through a dipole magnet, which disperses them horizontally on a scintillating screen, which is imaged by a camera. As the dispersion distance depends on the electron energy, the position on the scintillating screen can be translated into an energy, provided the magnetic field and geometry, i.e. the distance and angle between the dipole and the screen. A NdFeB dipole magnet with a peak magnetic field of 0.8 T (see Figure 2.14) is mounted on a translation rail and can be inserted immediately after the gas target to disperse the electron beam onto a 25 cm wide scintillating screen. The angle between the optical axis and the scintillating screen normal is 60°. The dipole magnet has a pole gap of 15 mm and a length of 20 cm (excluding the external aluminium spacers), resulting in a detectable energy range of $10 - 350$ MeV in the currently used geometry. Due to the combination of the energy-dependent dispersion angle and horizontal focusing of a dipole magnet, the energy resolution $\Delta E/E$ decreases approximately linearly with energy, ranging from 0 to 1.5 %/mrad for energies between 0 and 350 MeV.

In the study presented in Paper II, an additional electron spectrometer was used to compare the electron spectrum before and after focusing the electron beam using an electromagnetic quadrupole (EMQ) triplet (see Section 3.9.2). This spectrometer has a length of 10 cm and a peak magnetic field of ~ 0.65 T. The detectable energy range is 40 - 180 MeV, the dispersion curve and the magnetic field are shown in Figure 2.15.

2.4.3 X-ray detector

The X-ray detector used in the studies described in this thesis was an Andor Ikon-L SO, which is a 16-bit, back-illuminated, deep-depletion CCD. This technology is based mainly on the photoelectric effect and Compton scattering (commonly using a silicon layer), where the latter process dominates for photon energies above 40 keV. For energies up to a few keV the process is almost exclusively due to the photoelectric effect [14]. As a photon interacts with the silicon layer, a number of electron-hole pairs are formed, which is proportional to the energy of the incoming photon. An electric field will accelerate the charge cloud towards the nearest potential well, where the charge can

be collected. Over this drift distance, the charge cloud will expand due to diffusion and inter-charge repulsion. If this drift distance is significant, it can lead to the charge collected in one pixel bleeding over to another pixel, known as pixel cross-talk which results in a loss in spatial information. There are several ways to limit this but for back-illuminated CCDs (i.e. the readout electrodes are positioned behind the silicon substrate) the silicon layer is made thin to reduce the drift distance. This limits the efficiency in the detection of high-energy X-ray photons as they may pass through the substrate without interacting. To improve the performance, doped silicon is commonly used which increases the depth of depletion, allowing for a thin substrate to be used while not sacrificing as much detection efficiency in the higher photon energy region. Figure 2.16 shows the quantum efficiency of the CCD used in this work.

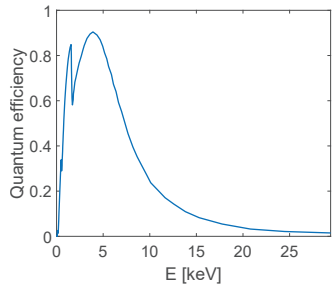

Figure 2.16. *Quantum efficiency for the Andor Ikon-L SO X-ray CCD camera.*

A pre-amplifier increases the signal strength by a factor $\times 1$,$\times 2$, or $\times 4$ depending on the settings, after which a high-speed digital counter stores the information. As this operation takes some time (usually about 100 ns), photons arriving within this time will be summed and counted as a single event. In low-intensity scenarios it is possible to perform single-photon counting, i.e. every pixel collects at most 1 photon per 100 ns. In this case, the count will be proportional to the photon energy, and the device will function as an imaging spectrometer.

The Andor Ikon-L SO detector has 2048×2048 pixels, each 13.5×13.5 μm^2 with a total imaging area of 27.6×27.6 mm^2. Due to its high sensitivity to dark currents, the camera is cooled to -70 °C, and the chip must therefore be in vacuum to avoid the formation of ice crystals on the sensitive substrate during operation. A 250 μm thick beryllium filter is mounted on the camera to form a vacuum-tight window, transmitting X-rays above ~ 2 keV.

2.5 Ion acceleration chamber

The typical set-up in the ion acceleration chamber is shown in Figure 2.17. A small leak from a dielectric mirror is extracted for near- and far-field imaging of the laser pulse (not shown here), in a similar fashion to the electron acceleration chamber. The laser pulse enters the chamber P-polarized, the influence of polarization in ion acceleration is briefly discussed in Section 5.1. The pulse is focused using an $f/3$ OAP to a spot size of 2.5 μm (FWHM) at a solid target in the centre of the chamber. As the Rayleigh length is very short in this set-up,

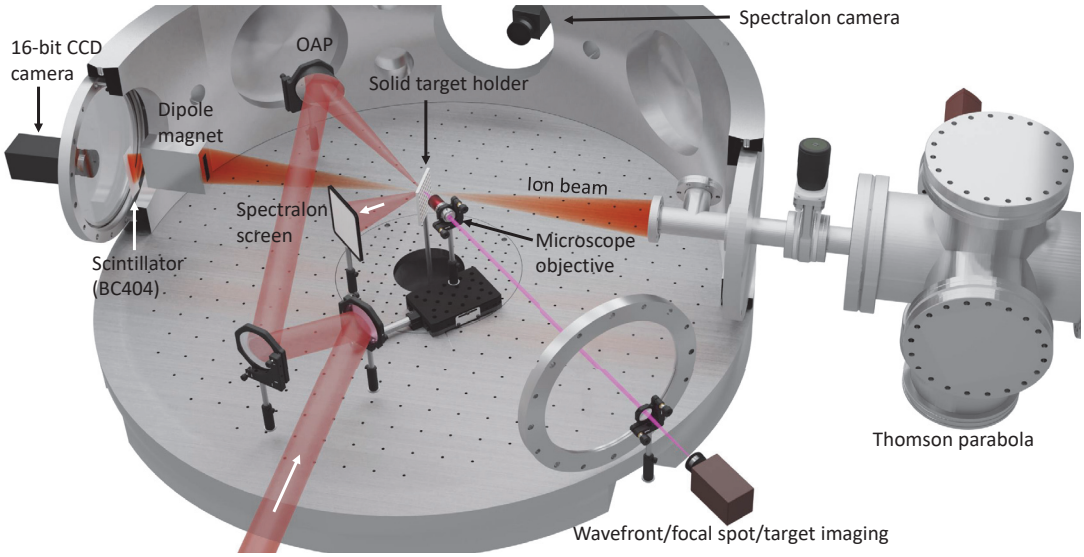

Figure 2.17. *Illustration of the typical set-up in the ion acceleration chamber.*

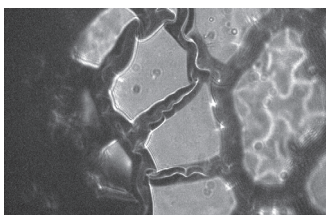

Figure 2.18. *Microscope image of a 250 nm thick carbon-foil target (10× magnification).*

$Z_R = w_0^2\pi/\lambda \approx 18$ µm, the longitudinal alignment of the target in relation to the laser focal point is very important. Alignment is performed by imaging the laser spot and target in the same plane using a ×10 magnification, long working-distance microscope objective in a relay imaging configuration. Figure 2.18 shows a microscope image of a 250 nm thick carbon foil target using this imaging configuration. The foils usually have some wrinkles, seen as dark areas in Figure 2.18 which affect the ion beam pointing, thus, the laser pulse is focused on the flat areas. The same imaging set-up is used to image the laser wavefront using a wavefront sensor (Phasics SID4). The foil is sandwiched between two perforated plates which is mounted on a XYZ translation stage. As the foil is locally destroyed where the laser pulse hits, a new area of the foil needs to be aligned for the next laser pulse. Finally, a diffuse Spectralon screen that scatters more than 99 % in the near-infrared region is imaged and used to measure the laser energy reflected off the target.

2.5.1 Ion spectrometers

The first spectrometer is a magnetic dipole with a small entrance slit, similar to that used in the gas target interaction

chamber. The dipole is used to analyse the backward directed ion beam and disperses it vertically on a scintillating screen that is imaged using a 16-bit camera (see Figure 2.17).

A Thomson parabola spectrometer, which allows for separation of the different ion species, is used to analyse the forward directed ion beam. In a Thomson parabola spectrometer, an electric field parallel to the magnetic field, is introduced (in addition to the constant magnetic field), that is used to spatially separate ions based on their charge-to-mass ratio. The dispersed ion beam is imaged using a micro-channel plate with a phosphor screen and a 12-bit CCD camera. The detectable energy range is 1 - 10 MeV for protons, with an energy resolution of $\Delta E/E = 5$ % at 10 MeV. Figure 2.19 shows a typical ion beam spectrum together with the traces from the Thomson parabola spectrometer.

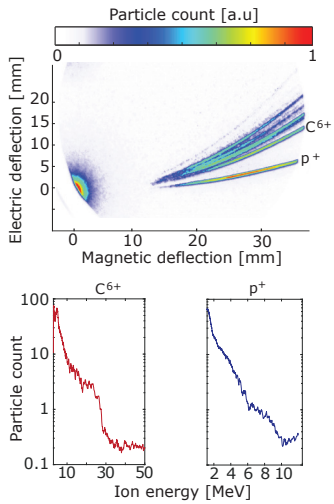

Figure 2.19. *Above: Thomson parabola traces where the proton trace and C^{6+} trace are indicated, the other traces are different carbon and oxygen ions. The vertical axis shows the deflection due to the electric field, while the horizontal axis shows the deflection due to the magnetic field. Below: the energy spectrum for C^{6+} together with the proton spectrum, p^+. (Courtesy of A. Permogorov)*

2.6 Radiation safety

The environment surrounding a particle accelerator will always be subject to radiation of one form or another. This is commonly managed with radiation shielding and dosimeter alarm systems together with a stringent safety procedure. During the course of this work, a study was performed for the Swedish Radiation Safety Authority to characterize the radiation environment surrounding the laser-plasma accelerator at the Lund MTLF [15].

Several simulations were performed using FLUKA [16–19], a general-purpose Monte Carlo code for particle transport. The code includes the physics necessary to calculate secondary radiation, such as low-energy neutron transport, heavy-fragment transport, thermal-energy-neutron transport, scattering, electromagnetic-field interactions, heavy-particle bremsstrahlung and pair production. The quantity simulated was the ambient dose equivalent, which is the dose equivalent at a depth of 10 mm in soft tissue for the expanded and aligned radiation field. This quantity is commonly used to characterize the radiation in an area, and includes conversion coefficients for particle flux to effective dose, as some particle species are more harmful than others. According to the International Commission on Radiological Protection, the yearly ambient dose equivalent should be less than 1 mSv/year to the general public, while for trained personnel working in radioactive environments it is recommended to be below 20 mSv/year.

To obtain a yearly ambient dose equivalent, it was assumed that 30,000 electron beams were generated over a year, each

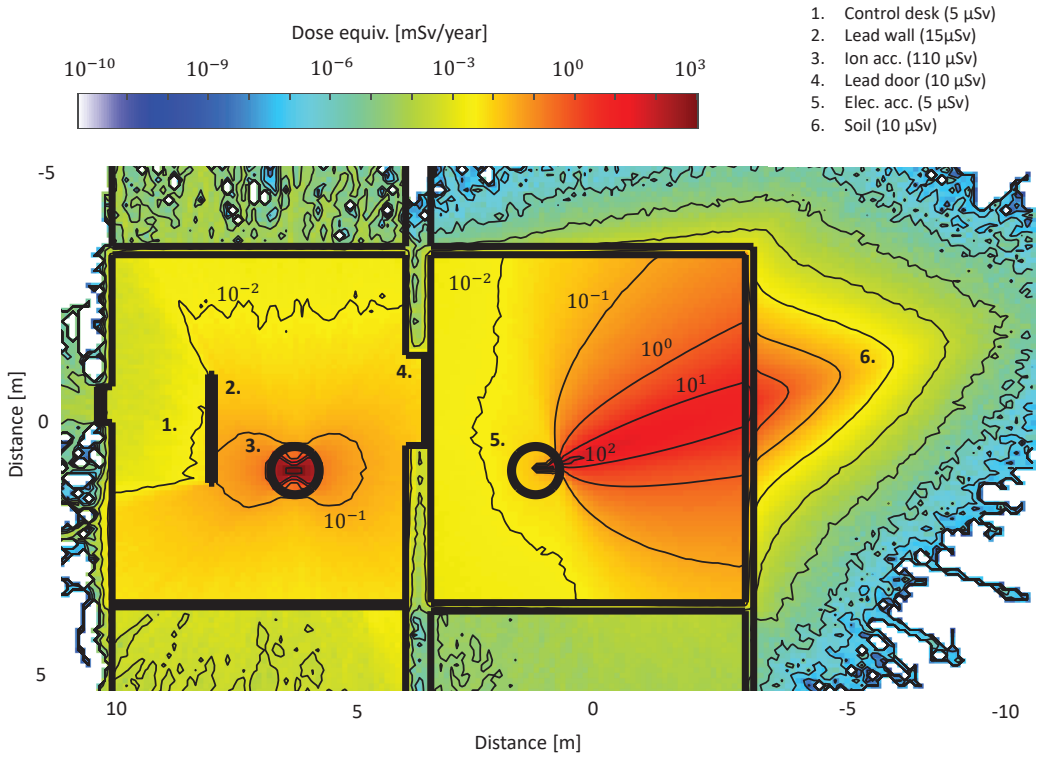

Figure 2.20. *Simulated annual ambient dose equivalent at the Lund MTLF.*

beam containing a charge of 32 pC with an average energy of 120 MeV. Additionally, the generation of 2,000 ion beams per year was assumed, each beam containing 10^{12} particles, of which 67 % were electrons. The electrons were assumed to follow a Maxwell-Boltzmann distribution, and the ions follow an exponentially decreasing spectrum based on previous experiments, with a maximum energy of 8 MeV.

In the electron acceleration chamber, mainly electrons are accelerated, however, secondary gamma and neutron radiation is also generated, mostly due to bremsstrahlung and (γ, n) reactions. The beam is pointing towards the rear wall of the room, behind which is a large soil mound on the outside of the building. The beta radiation is highly directed, and most of it is deposited in the rear wall and the dirt mound. The simulations took into account the dispersion of the electron beam by the dipole spectrometer, after which the beam passes through

a scintillating screen and the chamber wall. The secondary gamma radiation is less directed and shielding is more difficult, although the peak annual dose equivalent due to gamma radiation is about 10 times lower than the beta radiation. Most of the gamma radiation is shielded by the lead door and wall, see Figure 2.20, reducing it by 4 orders of magnitude. The distribution of neutron radiation is spherical and constitutes a very small contribution, about 10^{-9} mSv/year immediately outside the interaction chamber

The main contribution from the ion acceleration chamber is secondary gamma radiation, as the accelerated ions (and electrons) are efficiently stopped by the chamber walls. The particles produced in this chamber have lower energy than those produced in the electron acceleration chamber, thus, almost no neutron radiation is generated here.

The choice of materials used in the interaction chambers is of importance with regard to induced radioactivity. The main form of induced radioactivity in this case arises from neutron activation, with a very minor contribution from photodisintegration. Figure 2.21 shows the simulated induced activation immediately after a high-charge electron beam has been accelerated. Due to the short half-life of the activated isotopes (ms to s), most will have decayed significantly after 10 s. Only common materials in or around the interaction chamber, such as silicon, concrete, copper, iron, lead, tantalum, PMMA and beryllium were included in this simulation.

Even though the radiation level surrounding the ion acceleration chamber is below 1 mSv/year, efforts must be made to minimize the radiation exposure as much as possible. Therefore, all personnel in the lab are required to wear personal dosimeters to monitor the radiation exposure, and the attending personnel must be situated behind the lead wall during particle acceleration. The simulations show that the generated radiation reaching the control desk area is well within the safety limits. Furthermore, the lab is located under ground with thick, shielding, concrete walls, making the surrounding area outside the lab safe in terms of radiation exposure.

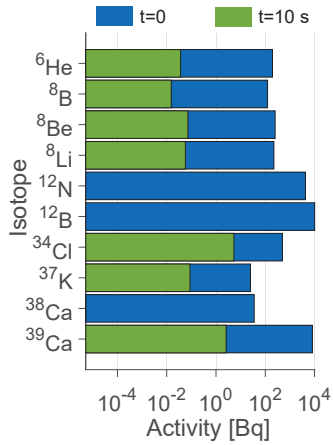

Figure 2.21. *The induced activity immediately after an electron beam has been accelerated (blue) for the 10 most radioactive isotopes. The activity 10 seconds after an electron beam has been accelerated is shown in green.*

Chapter 3

Electron acceleration and applications

This chapter is divided into two parts, one regarding electron acceleration and the other regarding applications. The first provides an introduction to under- and over-dense plasmas. Some important concepts in wakefield acceleration are introduced, such as the ponderomotive force, the dephasing length, the depletion length, self focusing and self-compression. A description of the different ionization mechanisms then follows. The section on electron acceleration ends with the concept of trapping electrons in the plasma wake, and a presentation of three different trapping schemes, namely, self-injection, ionization injection and shock-front injection.

The second part of this chapter starts with a description of electron beam focusing using either electromagnetic quadrupoles (EMQ) or plasma lenses. This is followed by a theoretical discussion on electron interactions with matter, and the chapter ends with a section on very-high energy electron radiotherapy.

3.1 Plasma

Plasma is often referred to as the 4th state of matter, which is created when sufficient energy is deposited into matter of another state (solid, liquid or gas). This results in some, or all, of the orbital electrons being stripped from the atoms. The overall charge of a plasma is neutral, but may locally be non-charge neutral. The plasma tends to shield these charge distributions, through a mechanism known as Debye shielding. Since the ions

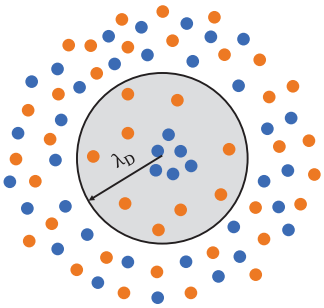

Figure 3.1. *The Debye length is the radius of a sphere over which charge distributions can be shielded from the surrounding plasma. Electrons are depicted as blue dots while ions are orange.*

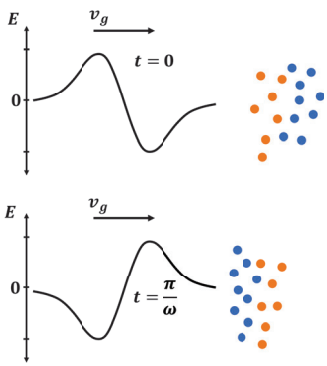

Figure 3.2. *A plasma frequency higher than the external field frequency means that the plasma can effectively shield the external field, thus it can not propagate.*

in the plasma are considerably heavier than electrons, their motion during the time interval of interest for laser-plasma acceleration can be neglected and the Debye length can be written as:

$$\lambda_D = \sqrt{\frac{\epsilon_0 k_B T_e}{n_e e^2}} \tag{3.1}$$

where T_e is the electron temperature, n_e the electron density, k_B the Boltzmann constant, ϵ_0 is the vacuum permittivity and e is the elementary charge. The Debye length, λ_D, is the radius of a Debye sphere, which describes the distance over which the electrostatic effect of any inhomogeneities in a plasma persists (see Figure 3.1). For laser-produced plasmas such as those discussed here, the electron density generally ranges from 10^{18} to 10^{24} cm^{-3} and the electron temperature from 0.01 to 1 keV.

There are different ways of describing a plasma, but in general, one can assume a fluid-like behaviour if the plasma parameter $g \equiv 1/(n_e \lambda_D^3) \ll 1$. All plasmas discussed in this thesis are assumed to be in this regime. This essentially means that there is significantly more than one particle within a Debye sphere at any given location, which guarantees that the collective effects of the plasma are much greater than the electron-ion collision effects.

3.2 Under- and over-dense plasmas

Due to the fluid-like behaviour of a plasma, an electron plasma frequency can be defined that describes the frequency at which the plasma can react to external electromagnetic forces:

$$\omega_p \equiv \sqrt{\frac{e^2 n_e}{\epsilon_0 m_e}} \tag{3.2}$$

where m_e is the electron mass. If the plasma frequency, ω_p, is higher than the frequency of the external field ω, there will be sufficient time for the charge distributions to re-arrange to completely shield the external electromagnetic field. This makes it impossible for the field to propagate in the plasma; the critical frequency being $\omega_p = \omega$. Thus, a critical density can be defined as:

$$n_c = \frac{\epsilon_0 m_e}{e^2} \cdot \omega^2 \tag{3.3}$$

above which the plasma is called over-dense ($n_e > n_c$), and below which it is under-dense ($n_e < n_c$). For example, a plasma with an electron density $n_e > 1.7 \times 10^{21}$ cm^{-3} will be over-dense (typically generated by ionizing solid matter) for a

Ti:sapphire-generated laser pulse with a central wavelength of 800 nm, while for $n_e < 1.7 \times 10^{21}$ cm^{-3} the plasma will be under-dense (typically generated by ionizing a gas).

The refractive index of a plasma is given by the Maxwell relation to be:

$$n = \sqrt{1 - \frac{\omega_p^2}{\omega^2}} \tag{3.4}$$

which further demonstrates the distinction between under- and over-dense plasmas. The refractive index is imaginary for $\omega < \omega_p$ (over-dense), i.e. light cannot propagate beyond the skin depth $l_s = c/\omega_p$, and the external electromagnetic field will be reflected upon incidence.

3.3 Ponderomotive force

A charged particle in an oscillating homogeneous electric field will undergo harmonic motion, moving back and forth in a straight line in the direction of the electric field. However, in an inhomogeneous field such as that of a laser pulse of finite size, particles also drift towards regions of lower intensity. Consider the situation in Figure 3.3 where an electron will move towards the right until the field has switched direction. The electron will then move in the opposite direction, but as the field is lower at this position the electron does not reach its initial position. This process is repeated until the electron is located in the region with the lowest intensity. This is known as the ponderomotive force. It should be noted that a positively charged particle will experience the same sort of motion (but it will be out of phase compared to an electron as it will decelerate when the electron accelerates, and vice versa). The ponderomotive force for a non-relativistic particle is given by [20]:

$$\mathbf{f}_p = -\nabla \Phi_p = -\frac{e^2}{2m_e\omega^2} \nabla \langle \mathbf{E} \rangle^2 \tag{3.5}$$

where Φ_p is known as the ponderomotive potential, $\mathbf{E}$ is the electric field and $\langle . \rangle$ denotes the time average over one cycle. In a plasma, a laser pulse will therefore expel charged particles from the high-intensity region. From Equation 3.5 it is evident that an ion will move considerably slower than an electron as the force scales inversely with the particle mass. Therefore, on the timescale of interest during wakefield acceleration, the ions can be considered to be stationary, while the electrons will

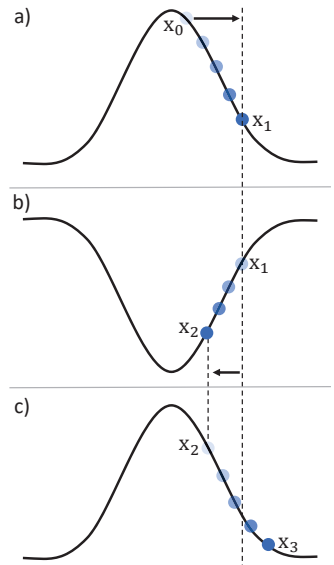

Figure 3.3. *Illustration of the ponderomotive force. The black line shows the amplitude of the electric field. a) The electron (blue) starts at position x_0 and moves to the right, to position x_1 due to the electric field. When the field changes sign, b), the electron moves to position x_2, which is just short of its starting position as the field is at x_1. When the field switches again, c), the electron moves to position x_3. In time, the electron gradually drifts towards the position of the lowest intensity.*

be expelled by the ponderomotive force. This creates a cavity, void of electrons, that travels in the wake of the laser pulse.

In very strong electric fields, an electron undergoes harmonic motion and quickly approaches the speed of light, becoming relativistic. Thus, it is useful to introduce the normalized vector potential:

$$\mathbf{a} = \frac{e\mathbf{A}}{m_e c} \tag{3.6}$$

where $-\partial\mathbf{A}/\partial t = \mathbf{E}$ and the normalized peak vector potential, which is given by:

$$a_0 = |\mathbf{a}_{max}| = \frac{eE_0}{\omega m_e c} = \sqrt{\frac{e^2\lambda^2 I}{2\pi^2\epsilon_0 m_e^2 c^5}} \tag{3.7}$$

For $a_0 > 1$, an electron will be relativistic within one oscillation and the intensity is said to be relativistic. At relativistic intensities ($I > 2 \times 10^{18}$ W/cm^2 for $\lambda = 800$ nm) the ponderomotive force takes a more complicated and non-linear form as the increase in electron inertia must be taken into account. (See, for example [20] for further derivations.) At these intensities, the ponderomotive force can be strong enough to completely expel all the electrons close to the laser pulse and this is known as the "blow-out" regime or "bubble" regime.

In the linear (non-relativistic) case for a linearly polarized laser pulse, the electrostatic wake potential ϕ is described by [21]:

$$\frac{\partial^2\phi}{\partial\xi^2} = k_p^2\left(\frac{a^2}{4} - \phi\right) \tag{3.8}$$

where $\xi = z - ct$ and $k_p = \omega_p/c$. This holds for an initially homogeneous plasma and small perturbations in electron density, $\delta n \ll n_0$, where n_0 is the initial electron density. Equation 3.8 can be solved analytically with Green's functions and has the following solution [22].

$$\phi = \frac{k_p}{4}\int_{\xi}^{0} \sin(k_p(\xi' - \xi))a^2(\xi')d\xi' \tag{3.9}$$

In the non-linear (relativistic) case, the wake potential is described by [22]:

$$\frac{\partial^2\phi}{\partial\xi^2} = \frac{k_p^2}{4}\left(\frac{1 + a^2}{(1+\phi)^2} - 1\right) \tag{3.10}$$

which has analytical solutions for a square laser pulse spatial profile. The longitudinal electric field is related to the wake potential by:

$$E_z = \frac{m_e c^2}{e} \frac{\partial \phi}{\partial \xi} \tag{3.11}$$

and the electron density is:

$$n_e = n_0 \left(\frac{1}{k_p^2} \frac{\partial^2 \phi}{\partial \xi^2} + 1 \right) \tag{3.12}$$

A numerical solution to the linear case is shown in Figure 3.4, where the longitudinal electric field and electron density are sinusoidal. The non-linear case is shown in Figure 3.5. In the non-linear case, the electron density decreases to zero, and is highly localised at the back of the bubble, indicating the blow-out regime. The fluid model is inadequate for a more complete description of the interaction and kinetic theory must be used, which describes the particle velocity distribution at every point in the plasma. The equation of motion for each particle can be solved numerically in particle-in-cell (PIC) codes, either 2D or 3D. Figure 3.6 shows the results given by the 3D PIC code Calder-Circ.

In the expelled region, the resulting space charge forces will point inwards toward the centre of the bubble. The outward pushing force is the ponderomotive force, so the size of the bubble, see Figure 3.6, can be estimated from the following relation [21].

$$r_b \approx 2\sqrt{a_0} \frac{c}{\omega_p} \tag{3.13}$$

For $a_0 = 2$, this corresponds to a bubble radius of $r_b \approx \lambda_p/2$. Note that it is assumed that the plasma is driven under resonance conditions, i.e. the root-mean-square (RMS) of the laser pulse duration is [21]:

$$\tau_{rms} \approx \frac{\lambda_p}{c 2\pi} \tag{3.14}$$

It should be noted that the optimal pulse duration depends on the temporal shape of the pulse, and if the plasma wave is driven in the linear or the non-linear regime. Here, it is given for a pulse with a Gaussian temporal profile and a wake driven in the non-linear regime.

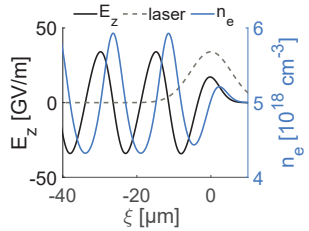

Figure 3.4. *Longitudinal electric field and electron density for a linear wave, driven by a pulse with an intensity of* 10^{16} W/cm^2 *in a plasma with* $n_e = 5 \times 10^{18}$ cm^{-3}.

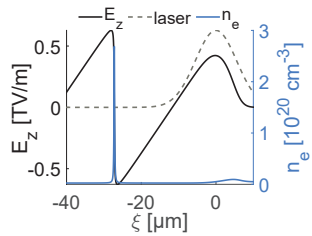

Figure 3.5. *Longitudinal electric field and electron density for a non-linear wave, driven by a pulse with an intensity of* 10^{18} W/cm^2 *in a plasma with* $n_e = 5 \times 10^{18}$ cm^{-3}.

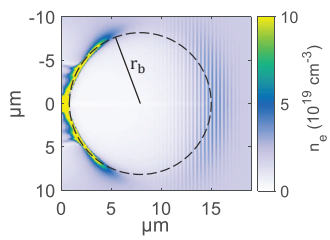

Figure 3.6. *Result from a 3D PIC simulation in the blow-out regime, the dashed circle indicates the bubble radius,* r_b, *and the laser is located at the front of the bubble, propagating from left to right. (Courtesy of H. Ekerfelt)*

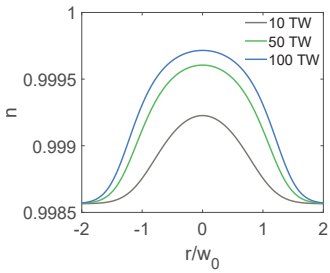

Figure 3.7. *The refractive index in a plasma with $n_e = 5 \times 10^{18}\ cm^{-3}$ for different laser powers. The refractive index scales with the laser pulse intensity which in turn results in a focusing laser beam.*

3.4 Self-focusing

As the laser pulse diffracts, the cross-sectional area of the beam doubles after one Rayleigh length, $Z_R = \pi w^2/\lambda$. This would limit the interaction length to a few Rayleigh lengths as the peak intensity decreases rapidly. However, inside the plasma, the laser pulse will self-focus due to the Gaussian-like refractive index, which can lead to an interaction length much longer than the Rayleigh length.

The refractive index is given by Equation 3.4 for the non-relativistic case. However, for relativistic intensities, the relativistic mass of the electrons, m_{rel}, must be taken into account. As $\omega_p \propto 1/\sqrt{m_{rel}}$, and $m_{rel} = \gamma m_e$, the refractive index of the plasma is instead given by [4, 22]:

$$n(r) \approx 1 - \frac{\omega_p^2}{2\omega^2} \frac{n_e(r)}{n_0 \gamma(r)} \tag{3.15}$$

In the case of a linearly polarized laser pulse, the relativistic factor of the electrons, γ, and electron density, n_e, is not constant in the radial direction, r. As the electrons are mainly driven in the polarization direction, $\gamma(r) \approx \sqrt{1 + a(r)^2}$, where $a(r)$ is the laser pulse profile, $a(r)^2 = a_0^2 \exp(-2r^2/w^2)$ for a Gaussian pulse with a radius r. Figure 3.7 shows the refractive index (assuming a homogeneous electron density). This shows that the refractive index is higher in high-intensity regions, i.e. the laser pulse phase velocity $v_{ph} = c/n$ decreases on-axis and increases off-axis. This results in a focusing beam as the wave front gains curvature. It should be noted that, in order for the laser pulse to self-focus, the focusing has to be larger than the diffraction. Therefore, there exists a critical power, above which self-focusing can occur. This is commonly estimated from the expression below [23].

$$P_c = \frac{8\pi\epsilon_0 m_e^2 c^5 \omega^2}{e^2 \omega_p^2} \tag{3.16}$$

For a central laser wavelength of $\lambda = 800$ nm and electron density of $n_e = 5 \times 10^{18}$ cm^{-3} this correspond to a critical power of $P_c \approx 6$ TW.

3.5 Self-compression

The refractive index in the plasma does not only change radially, but also longitudinally. Therefore, the head of the laser pulse will have a lower group velocity while than the tail of the pulse. Thus, the pulse will self-compress, leading to a shorter

temporal duration. As the intensity increases due to self-compression, this will results in stronger self-focusing, which further enhances self-compression, as the pulse-compression rate is proportional to the inverse square of the laser spot size [24]. As stated in Section 3.3, the optimal condition for driving the plasma wave occurs at a certain pulse duration, given by Equation 3.14. However, this condition is slightly relaxed due to the self-compression as the duration of the pulse decreases towards approximately half the period of the plasma wave.

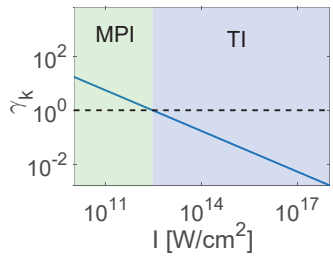

Figure 3.8. *Keldysh parameter, γ_k, for different orders of magnitude of the laser intensity. When $\gamma_k \gg 1$ the ionization is mainly MPI, while for $\gamma_k \ll 1$ it is mainly TI.*

3.6 Ionization

An atom can be ionized through several different physical processes, largely depending on the laser intensity. For intensities of $\sim 10^9 - 10^{13}$ W/cm^2 the process is described by perturbation theory, and is called multiphoton ionization (MPI) which is a non-linear process. An electron in a bound state may absorb several photons in rapid succession while moving through intermediate virtual states until its energy is high enough to escape the Coulomb potential. Although plasma breakdown has been observed at intensities as low as 10^9 W/cm^2, the ionization processes at these low intensities are not well understood and, for noticeable MPI, the intensity generally has to be above 10^{11} W/cm^2 [25].

At intensities higher than 10^{13} W/cm^2, the description by perturbation theory breaks down and a quasi-static electric field must be assumed that distorts the potential well of the atom. In this region, ionization takes place through tunnel ionization (TI). There is no sharp transition between the two regimes but at intensities resulting in a Keldysh parameter $\gamma_k \gg 1$, one can safely assume MPI, while for $\gamma_k \ll 1$ one can assume tunnel ionization. The Keldysh parameter is given by [26]:

$$\gamma_k = \sqrt{\frac{I_p}{2U_p}} \tag{3.17}$$

where $U_p = E^2 e^2 / 4 m_e \omega^2$ is the non-relativistic ponderomotive energy of an electron, i.e. the average quiver energy over one cycle in the electromagnetic field E, and I_p is the ionization potential of the atom. Figure 3.8 shows the Keldysh parameter for hydrogen at intensities of different orders of magnitude.

Higher field strengths result in greater barrier distortion. If it is sufficiently distorted, an electron may tunnel through the potential well and escape the attractive force of the atomic core, as shown in Figure 3.9. At even higher intensities, the

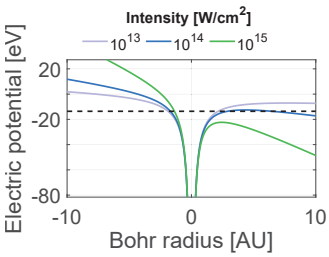

Figure 3.9. *Potential well of a hydrogen atom in the electromagnetic field of a laser at laser intensities 10^{13} W/cm^2 (bright blue), 10^{14} W/cm^2 (blue) and 10^{15} W/cm^2 (green). The black dashed line indicates the ionization potential.*

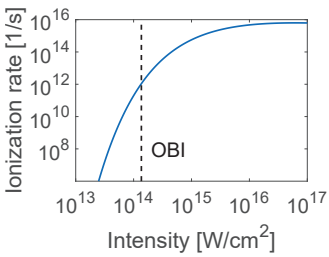

Figure 3.10. *ionization rate of hydrogen for varying intensities. The dashed line shows the transition from tunnel ionization to over-the-barrier ionization.*

electric field may be strong enough to distort the potential well such that it falls below the lowest bound state, leading to instantaneous complete ionization of the atom. This is known as over-the-barrier ionization (OBI) or barrier suppression ionization.

The ionization rate of hydrogen as a function of laser intensity is shown in Figure 3.10, obtained using the Ammosov-Delone-Krainov formula (not shown here) [27]. It is evident that the ionization rate increases rapidly with increasing intensity. At intensities above 10^{14} W/cm^2, the ionization rate stagnates as the intensity is high enough for OBI. The vertical dashed line in Figure 3.10 indicates the intensity that distorts the potential barrier to the same level as the lowest bound state. This is known as the "appearance intensity" and is given by [28]:

$$I_{app} = \frac{c}{128\pi}\left(\frac{4\pi\epsilon_0}{e^2}\right)^3 \frac{I_p^4}{Z^2} \tag{3.18}$$

where Z is the charge of the atomic core. Note that this model does not take into account the AC Stark shift or reflections, i.e. electrons that escape the potential well and reverse in the oscillating electric field, accelerating back towards the core [27].

3.7 Electron trapping

The terms trapping or injection are commonly used to describe the process of an electron being trapped inside the electrostatic potential inside the plasma wake. This process can be described in phase space using the Hamiltonian [29]:

$$\mathcal{H}(\gamma, \xi) = \gamma(1 - \beta\beta_p) - \phi(\xi) = const, \tag{3.19}$$

where $\beta_p = \tilde{v}_p/c$ is the normalized plasma-wave phase velocity and $\beta = \sqrt{1 - 1/\gamma^2}$. A trapped electron will form a closed orbit in phase space as it is periodically moving back and forth inside the wake, gaining and losing momentum. Figure 3.11 shows the phase space for electrons in the linear plasma wave shown in Figure 3.4. For an electron to be trapped, its initial velocity needs to be close to that of the plasma wave velocity $\tilde{v}_p$, i.e. $\gamma/\gamma_p \approx 1$, where $\gamma_p = 1/\sqrt{1 - \beta_p^2}$. All other electrons escape the potential, and instead form the bulk of the plasma wave. The orbit that separates the non-trapped and trapped electrons is called the separatrix, which is given by $\mathcal{H}_s = 1/\gamma_p - \phi(\xi_{min})$, indicated by the black dashed line in

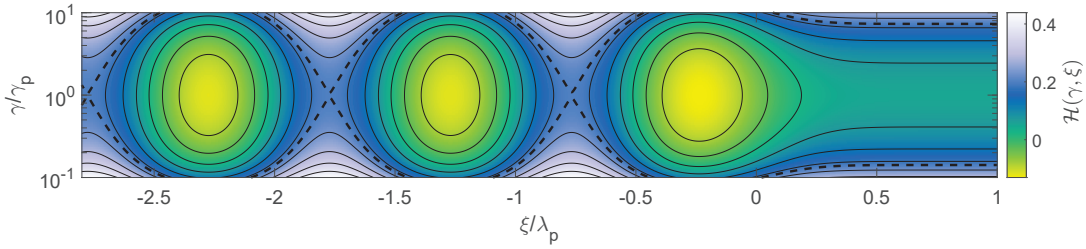

Figure 3.11. *Phase space for electrons of different γ in a linear plasma wave. A closed orbit in phase space corresponds to a trapped electron, which is more likely to occur if $\gamma \approx \gamma_p$. The separatrix is indicated by the dashed line.*

Figure 3.11. Here, ξ_{min} is the value that minimizes the potential, i.e. $\phi_{min} = \phi(\xi_{min})$.

As the energy gain in Equation 3.26 depends on the acceleration length, an electron trapped at an early stage of the acceleration process will gain more energy than an electron trapped at a later stage. This illustrates the need for different injection schemes, where in some, electrons are injected in a short time window, resulting in a quasi-monoenergetic beam, while in others the electrons are continuously injected, producing high-charge broadband beams.

3.7.1 Self-injection

The first injection mechanism used was self-injection, where electrons from the plasma wake become trapped in the wake potential. This is a highly non-linear process that is not yet fully understood but, due to historical reasons, one common picture is that of "wavebreaking". When the oscillation velocity of the plasma electrons is higher than the phase velocity, the plasma wave breaks, such that some plasma electrons can be trapped in the wake potential. Plasma wavebreaking is itself a field of research and includes different kinds of wavebreaking, such as geometrical breaking (also known as transversal wavebreaking), cold plasma wave breaking, fluid-like breaking in a warm plasma, kinetic wave breaking and resonant (wave) breaking [25]. Several different attempts have been made to explain the phenomenon in the blow-out/bubble regime, and to identify threshold for when it occurs [30–33]. In the bubble regime, an almost spherical ion cavity is formed with a thin, dense electron sheath around its surface. One explanation is that some of the electrons from the sheath may be channelled

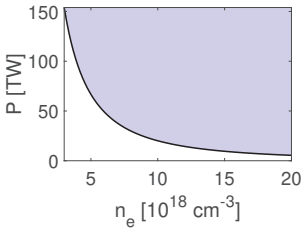

Figure 3.12. *Laser power required for self-injection (blue region) in the bubble regime.*

to the back of the bubble, where they quickly become accelerated to the velocity of the plasma wake and become entrapped [34]. In the electron density range of $3 - 20 \times 10^{18}$ cm^{-3} it has been shown experimentally that the self-injection threshold can be estimated using the expression [35]:

$$\frac{\alpha P}{P_c} > \frac{1}{16}\left(\ln\left(\frac{2n_c}{3n_e}\right) - 1\right)^3 \tag{3.20}$$

where α is the fraction of laser power within the FWHM laser spot size. Figure 3.12 shows the laser power required for self injection using $\alpha = 1/2$ which is the theoretical maximum for a beam with a Gaussian spatial profile.

3.7.2 Ionization injection

Self-injection is notoriously difficult to both predict and control as minor fluctuations can change the electron beam significantly. A popular and much more stable injection scheme is ionization injection, which takes advantage of the different ionization thresholds [36]. This usually involves a low-Z gas doped with a high-Z gas, such as He doped with N. Figure 3.13 shows the different ionization levels for He and N. The He atoms are fully ionized together with the 5 outer most electrons of N by the leading edge of the pulse, as the ionization threshold for these species are comparatively low. This generates the bulk of the plasma. The dopant should be chosen so that it is ideally fully ionized at, or above, the peak laser intensity (relying on self-compression and self-focusing). Thus, the last two electrons of N^{5+} will be ionized at the intensity peak of the laser pulse which results in a spatially localised electron injection. This allows electrons to be trapped in the potential more easily, Figure 3.13 shows the trapping of an on-axis electron together with an off-axis electron that does not gain enough momentum and slips away from the wake. The peak intensity can be above the dopant ionization threshold for a large part of the propagation distance, continuously injecting electrons, especially due to self compression and self focusing. This results in high beam charge but also a continuous electron energy spectrum.

As stated in the previous section, for an electron to be trapped, the Hamiltonian in Equation 3.19, must be smaller than the separatrix $\mathcal{H}_s$. From the plasma wake potential, ϕ, it is possible to find the location where an electron needs to be ionized in order to be trapped for a given electron density and a_0. This is depicted in Figure 3.14 where the location of

Ion	I_p [eV]	I [W/cm^2]
He	24.6	1×10^{15}
He^+	54.4	9×10^{15}
N	14.5	2×10^{14}
N^{1+}	29.6	8×10^{14}
N^{2+}	47.4	2×10^{15}
N^{3+}	77.5	9×10^{15}
N^{4+}	97.9	1×10^{16}
N^{5+}	552	1×10^{19}
N^{6+}	667	2×10^{19}

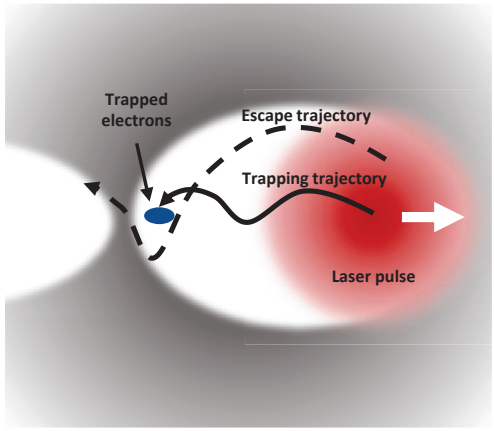

Figure 3.13. *The ionization potentials I_p of helium and nitrogen are given on the left. The laser intensity, I, required for OBI can be calculated using Equation 3.18 and is given in the right-hand column. The two most inner-bound electrons (N^{5+}, N^{6+}) in nitrogen will only be released at the peak intensity of the laser pulse. Some electrons ionized at the peak of the laser pulse (red) can be trapped (solid black line), while others will not have sufficient momentum and will undershoot the bubble (black dashed line).*

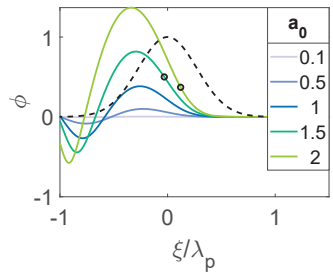

Figure 3.14. *Position in phase where ionized electrons can be trapped (black rings) assuming an electron density of $n_e = 5 \times 10^{18}\ cm^{-3}$.*

trapping is indicated by the black rings. Note that no trapping occurs for $a_0 < 1.5$ in this case, and for higher values of a_0, the trapping occurs close to the peak of the laser pulse which is shown as a dashed line with arbitrary amplitude.

3.7.3 Shock-front injection

One way of limiting the duration of injection to obtain a more narrow banded electron beam is to control the plasma density. Introducing a steep downward density gradient will cause the wake to expand rapidly, trapping some electrons in the potential [37, 38]. This density gradient can be produced using a gas jet with a supersonic gas flow and partially inserting a razor blade into the gas flow to create a shock front. Figure 3.15 shows an example of such a density gradient together with an illustration of the bubble expansion.

It is also possible to use a combination of shock-front injection and ionization injection. Upon introducing a density gradient, electrons ionized during the expansion of the plasma bubble will be trapped as they have time to gain sufficient energy and be trapped due to the increased length of the accelerating field [39]. This method was used to produce two spatially separated electron bunches in the experiment described

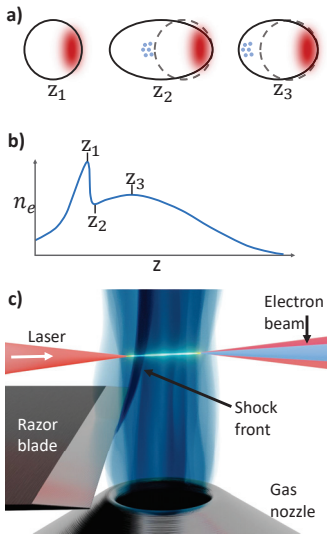

Figure 3.15. *Illustration of the shock-front injection scheme. As $r_b \propto 1/\sqrt{n_e}$), a sharp downward density gradient, see b), will cause the plasma bubble to expand rapidly, as illustrated in a), and if the gradient is sufficiently short, i.e. shorter than the plasma wavelength, some electrons at the tail of the original bubble will be trapped and accelerated [37]. A sharp density gradient can be achieved by inserting a razor blade in a supersonic gas jet, as seen in c).*

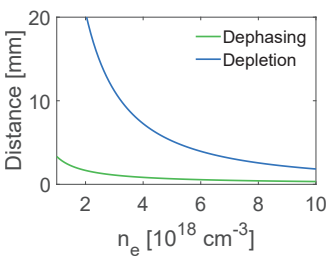

Figure 3.16. *Linear dephasing- and depletion lengths for a 32 fs, 800 nm laser pulse as a function of electron density.*

in Paper V. The shock front was positioned during the density up-ramp while the laser parameters were such that it still allowed for regular ionization injection later in the plasma. As the shock-front-injected electrons are injected earlier they gain more energy than the ionization-injected bunch.

3.8 Dephasing and depletion lengths

The velocity of a laser pulse inside the plasma is given by the group velocity v_g. Using the refractive index from Equation 3.4, this gives the following expression.

$$v_g = c\sqrt{1 - \frac{\omega_p^2}{\omega^2}} \tag{3.21}$$

The velocity of the electrons will quickly approach c as they are accelerated by the strong field gradients in the bubble. From Figures 3.4 and 3.5 it is evident that electrons will decelerate if they are located in the front half of the wake. This leads to a maximum acceleration length, i.e. the distance over which electrons reach the front half of the bubble and start decelerating, known as the dephasing length. In the linear case, the dephasing length is given by [21]:

$$L_{dp} = c\pi\frac{\omega^2}{\omega_p^3} \tag{3.22}$$

while in the non-linear case, it is [21]:

$$L_{dp} = ca_0\sqrt{2}\frac{\omega^2}{\omega_p^3} \tag{3.23}$$

In the non-linear case, the dephasing length scales with a_0 and in both cases it rapidly decreases with increasing electron density, as can be seen in Figures 3.16 and 3.17.

Another factor limiting the electron energy gain is pump depletion. As energy is required to excite the plasma wave, the driving beam will eventually be depleted. This is described by the pump depletion length which is given by [21, 40]:

$$L_p = \frac{4\pi c}{a_0^2}\frac{\omega^2}{\omega_p^3} \tag{3.24}$$

in the linear regime. In the linear case, the pump depletion length is much longer than the dephasing length (see Figure 3.16). The same is true in the non-linear case, in which the pump depletion is given by [21, 40]:

$$L_p = 2\sqrt{2}ca_0\frac{\omega^2}{\omega_p^3} \tag{3.25}$$

and the limiting term is, in general, the dephasing length (Figure 3.17). It should be noted that the non-linear case is more efficient as the dephasing and depletion lengths are better matched in this regime.

The energy gained by an electron is thus $\Delta E = eE_zL$, where E_z is the longitudinal electric field and L is the distance over which the electron is accelerated. Maximum energy is reached when $L = L_{dp}$ in the non-linear case. Using the average longitudinal electric field over the dephasing length, the approximate energy gain for a 3D non-linear case is given by [41]:

$$\Delta E = eE_zL \approx \frac{2a_0m_e^2c^2\omega^2\epsilon_0}{e^2n_e} \tag{3.26}$$

and is dependent on the normalized peak vector potential (or laser strength), a_0, and the electron density, as illustrated in Figure 3.18.

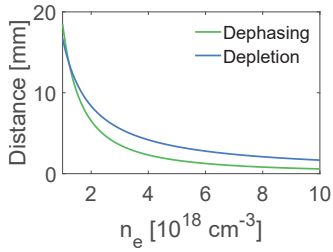

Figure 3.17. *Non-linear dephasing- and depletion lengths for a 32 fs, 800 nm laser pulse with $a_0 = 2.2$ as a function of electron density.*

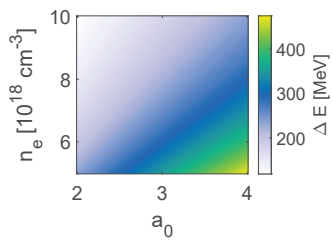

Figure 3.18. *Estimated energy gain, ΔE, as a function of a_0 and electron density n_e, with a central laser wavelength of 800 nm.*

3.9 Electron beam focusing

3.9.1 Plasma lenses

The electromagnetic forces acting on the trapped electrons inside the plasma wake point radially towards the centre of the bubble. This means that there is a focusing force present which, in principle, could focus an electron beam and act as a plasma lens. This has been demonstrated in beams generated by linear accelerators [42] and plasma accelerators [43]. The focusing fields depend strongly on the radial shape of the wakefield and the velocity of the plasma electrons, as both the beam itself and radial plasma electrons will induce a magnetic field [44]. Therefore, focusing will not be linear in general and may lead to some focusing aberrations. The focusability of the plasma wake can be improved by tailoring the plasma density profile. The wake in the plasma lens may be driven either by the electron bunch itself, if it is sufficiently intense, or by an external driver, such as a laser or another particle beam (Paper V). Due to the very high focusing field, 150 MT/m for an electron density of $n_e = 5 \times 10^{18}$ cm^{-3} [45], an electron beam may be significantly focused over a very short distance which helps preserve the emittance. The emittance is a quantity that describes the beam quality. In this thesis, the emittance used

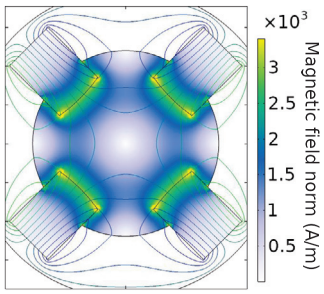

Figure 3.19. *Simulated magnetic field lines and the magnetic field norm at the cross-section of an EMQ.*

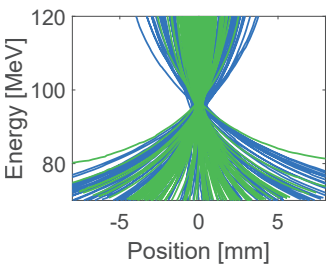

Figure 3.20. *Simulated transverse positions, (blue for horizontal and green for vertical), of electrons in the focal plane for different electron energies. In this case, 90 MeV electrons are focused correctly while electrons with other energies are either under- or over focused.*

is the RMS emittance: $\epsilon_{rms} = \sqrt{\langle x^2 \rangle \langle x^{2\prime} \rangle - \langle x x' \rangle^2}$ where $\langle x \rangle$ is the variance in the position of the electron and $\langle x' \rangle$ is the variance in the angle of the particle relative to the direction of propagation.

It is also possible to focus the beam using an active plasma lens, which can achieve focusing fields > 3000 T/m [46]. This principle is based on a plasma-filled discharge capillary where the discharge current induces the strongly focusing magnetic field.

3.9.2 Electromagnetic quadrupoles

An EMQ consists of 4 magnetic poles, symmetrically arranged around the beam axis with alternating polarities. The magnetic field norm is proportional to the distance from the central axis, and is zero on-axis (see Figure 3.19). Thus, an electron further off-axis experiences a greater force than an electron closer to the central axis, resulting in a focusing effect. Due to the plane symmetry of the field lines (see Figure 3.19), a single EMQ will focus in one plane but defocus in the other plane. By combining three EMQs, it is possible to focus in both planes, in an arrangement commonly known as a FODO lattice (focus - drift - defocus - drift - focus). The resulting focus is chromatic and only the electrons with the nominal energy will be correctly focused. For all other energies, the focus will be transversely elongated in one direction or the other as illustrated in Figure 3.20.

In beam physics, it is convenient to use the Twiss-, or Courant-Snyder parameters as they describe the collective behaviour of the beam and are related by:

$$\tilde{\gamma}\tilde{\beta} - \tilde{\alpha}^2 = 1 \tag{3.27}$$

These parameters describe different characteristics of the beam; $\tilde{\gamma}$ describes the beam size in relation to the energy spread. A high value of $\tilde{\gamma}$ corresponds to a small beam size, but a large energy spread. $\tilde{\alpha}$ describes the divergence; for a converging beam $\tilde{\alpha} > 0$ and for a diverging beam $\tilde{\alpha} < 0$, while $\tilde{\alpha} = 0$ at the focus. The betatron function $\tilde{\beta}$ describes the size of the beam envelope. Figure 3.21 shows the simulated beam size, σ, through the EMQ triplet at the Lund MTLF. Here, the beam was simulated using a flat, polychromatic spectrum with 7 mrad divergence, 2 mm in diameter (FWHM) beam. Figure 3.22 shows the beta function of the beam. The focus is located at 1.8 m (where $\tilde{\alpha} = 0$) and the beam is at its largest at 0.9 m, which is at the centre of the EMQ lattice. Due to

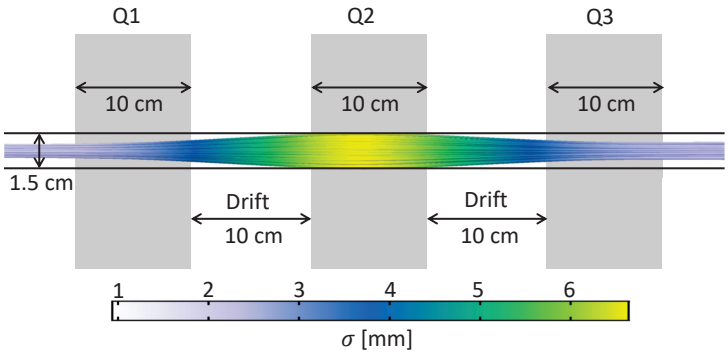

Figure 3.21. *Beam size* $\sigma = \sqrt{\tilde{\beta}\epsilon_{rms}}$ *through the EMQ triplet used in Paper II with an initial beam energy of 90 MeV. Initially, the beam size is 2 mm, with a divergence of 7 mrad, corresponding to* $\epsilon_{rms} \approx 3.2$ *μm. The beam size is at a maximum in the second quadrupole Q2 and lower energy electrons will exhibit a greater excursion from the central axis than higher-energy electrons and will be lost in collisions with the wall of the beamline.*

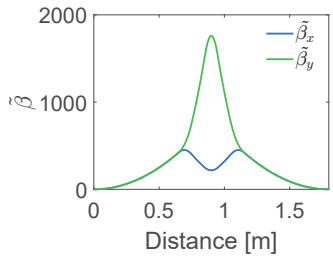

Figure 3.22. *Betatron function for a matched case with* $\tilde{\alpha} = 0$ *at 1.8 m from the source.*

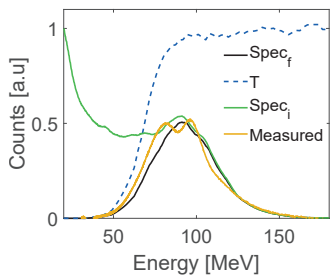

Figure 3.23. *Simulated transmission function T for the EMQ triplet (blue) Applying the transmission function on a measured spectrum,* $Spec_i$ *(green), results in the final transmitted spectrum,* $Spec_f$ *(black). This is compared to the experimentally measured spectrum (yellow).*

the expansion of the beam in the EMQs, some electrons might be lost due to wall collisions in the beamline which is only 15 mm in diameter. For a polychromatic beam, this results in a change in the final spectrum, as shown in Figure 3.23.

In the work described in this thesis, an EMQ triplet was used in a 1-to-1 imaging configuration to perform stereotactic dose deposition in a phantom (Paper II). The set-up was found to be independent of variations in the beam divergence and improved the stability of the beam, both in terms of beam charge and beam pointing. This can be seen in Figure 3.24, which shows the results when the beam area, A, and radial distance to the laser axis, r, were monitored in 8 consecutive shots.

3.10 Electron interactions with matter

When an electron passes through material it loses energy through various processes. Collisional losses are due to inelastic collisions with atomic electrons, while radiative losses result from inelastic collisions with nuclei, resulting in bremsstrahlung. Electrons can also scatter through elastic collisions, mainly with nuclei, but also with atomic electrons. Thus, as an electron beam propagates through a material, the mean energy will decrease and the beam divergence will increase. The mass scattering power of an electron describes the

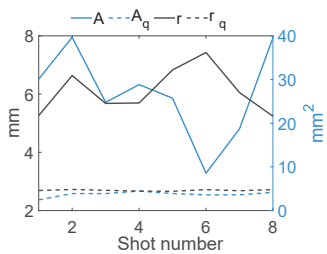

Figure 3.24. *Beam area (blue) and pointing (black) with the EMQ triplet (dashed lines) and without (solid lines).*

mean square scattering angle per unit mass thickness which is proportional to $(\tau_k+1)^2/(\tau_k(2+\tau)^2$ and to Z [47]. Here, τ_k is the kinetic energy normalized to the electron rest mass energy, $\tau_k = E_K/m_ec^2$. For high-energy electrons, i.e. $\tau_k \gg 1$, the mass scattering power is approximately proportional to $1/E_K^2$, thus high-energy electrons will scatter considerably less than low-energy electrons.

The attenuation of an electron beam is related to the total mass stopping power: $S_{tot} = S_{col} + S_{rad}$, which describes the energy lost per unit length in a certain material. The total mass stopping power consists of two parts, one of which is the collisional mass stopping power [48]:

$$S_{col} = \frac{N_A Z \pi r_e^2 2 m_e c^2}{A\beta^2}\left(\ln\left(\frac{E_K}{I_e}\right) + \ln(1+\tau_k/2) + F(\tau_k) - \delta\right) \tag{3.28}$$

where

$$F(\tau_k) = (1-\beta^2)(1+\tau_k^2/8 - (2\tau_k+1)\ln 2) \tag{3.29}$$

Here, I_e is the mean excitation potential, A is the atomic mass [g/mol], and N_A is Avogadro's constant. The correction term δ (density effect correction) takes into account the Coulomb force shielding of distant atoms due to polarization.

The second part of the total mass stopping power is the radiative mass stopping power S_{rad} [47]:

$$S_{rad} = \frac{\alpha r_e^2 N_A Z^2}{A}(E_{K_0} + m_e c^2) B_{rad} \tag{3.30}$$

which is due to electron - nuclei interactions, resulting in bremsstrahlung. E_{K_0} is the initial kinetic energy of the electron, α is the fine structure constant and the parameter B_{rad} takes different forms depending on the electron kinetic energy and ranges from 5 to 15 for electrons in the energy range of $10-100$ MeV [47].

The absorbed dose is:

$$D = \Phi S_{col} = -\frac{\Phi}{\rho}\frac{dE}{dx} \tag{3.31}$$

where Φ is the fluence (number/unit area). Note that only the collisional stopping power, and not the total stopping power contributes to the dose as the photons produced via bremsstrahlung tend to leave the region of interest and generally do not contribute to the local dose.

As the electrons continuously lose energy as they propagate through a material, the concept of range is convenient. The continuous slowing down approximation (CSDA) [47]:

$$R_{CSDA} = \int_0^{E_{K_0}} \frac{1}{S_{tot}(E)} dE \tag{3.32}$$

is the mean path length along an electron's trajectory. As stated above, the mass scattering power of an electron is proportional to Z, and the mean path length will be a good approximation of the range of an electron in materials with a low Z. For high-Z materials, the approximation will be poorer (and may differ by up to a factor 2) due to multiple scattering at large angles, resulting in irregular trajectories.

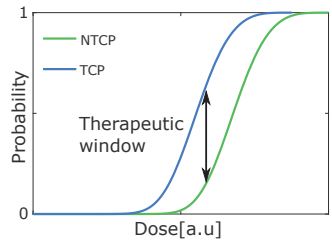

Figure 3.25. *The therapeutic window is the region between the tumour control probability (TCP) and the normal tissue complication probability (NTCP). Having a large therapeutic window corresponds to a large probability to control the tumour growth while simultaneously having a low probability for normal tissue complications. As such, the therapeutical window is different in each case, depending on tumour location, size, type and treatment method.*

3.11 Very high-energy electron radiotherapy

Radiotherapy is currently an important method of treating cancer, with more than 14,000 accelerators in 151 different countries [49]. This kind of treatment is based on the principle that healthy cells have a more effective DNA repair mechanisms than cancerous cells, thus, healthy cells can recover from radiation damage provided it is not too severe, while cancerous cells will die. Figure 3.25 illustrates the therapeutic window, which is the gap between the tumour control probability (TCP) and normal tissue complication probability (NTCP). It is obviously desirable to have a large therapeutic window, but simply increasing the dose tends to increase both TCP and NTCP, so other methods are required to widen the window. This is especially difficult for deep-seated tumours which are surrounded by healthy tissue.

Previously, electron therapy has mainly been used to treat superficial tumours and skin cancer due to the limited dose deposition depth of low-energy electrons. Deeply seated tumours are commonly treated with photon radiotherapy and, in sensitive cases, hadron therapy. While ions have a very energy dependent and localised dose deposition, it is very sensitive to inhomogeneities and there is a risk of shifting the Bragg peak position, depositing a large dose in healthy tissue. Radiotherapy machines are also very expensive, and their availability is thus limited. Treatment with very high-energy electrons (VHEE) has some advantages over conventional photon radiotherapy, such as less scattering due to the $1/E_K^2$ scaling of the scattering power, which limits the lateral spread of the beam. Furthermore, VHEE beams are almost insensitive to heterogeneities in the beam path. The dose deposited by a

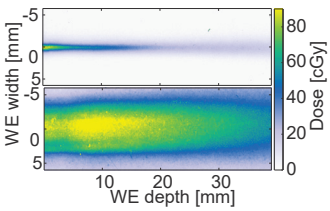

Figure 3.27. *Electron beam dose profile in an approximately water equivalent (WE) phantom (Perspex acrylic glass) with 90 MeV electrons focused at 30 mm (above) compared with an unfocused beam (below).*

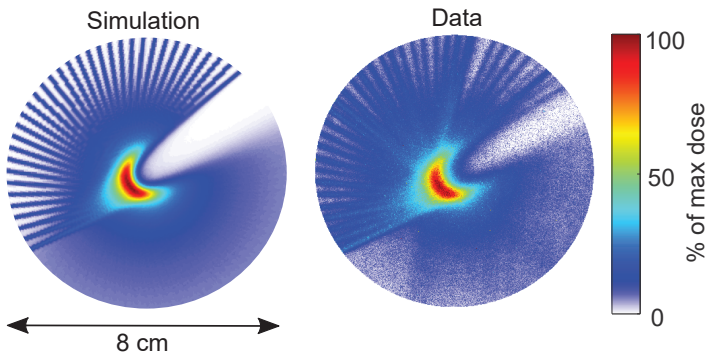

Figure 3.26. *Dose deposition in a cylindrical phantom using a focused VHEE beam. A FLUKA simulation is shown to the left, while the results from the experiment is shown to the right. The maximum dose is 2.72 Gy in the centre region while the doses in the beam entrance paths are about 0.3 Gy.*

photon beam at the interface of tissue or organs of different densities will change significantly due to electronic disequilibrium [50]. The same is true for ion beams, where a low-density cavity (such as air) will shift the longitudinal position of the Bragg peak deeper, while a denser medium (bone) will shift it to a shallower position [51]. One of the greatest advantages of VHEE may be the possibility to perform electromagnetic beam steering together with beam focusing. Beam steering allows for pencil beam scanning techniques while beam focusing has been shown to not only reduce the beam size significantly, but also allow tailoring of the dose depth profile [52, 53] to achieve concentrated dose distributions at greater penetration depths.

Several studies have demonstrated the potential of VHEE radiotherapy in the treatment of lung cancer [54, 55], prostate cancer [55–57], paediatric brain tumours and head and neck cancer [55, 58]. This motivated the study described in Paper II, where a focused VHEE beam was used to demonstrate fractionated stereotactic dose deposition in a cylindrical phantom using 36 beamlets at different angles.

A preliminary simulation performed using the Monte Carlo based particle transport code FLUKA is shown on the left in Figure 3.26, together with the experimental data on the right. In the simulation, the electron beam size was 2 mm in the focal plane, with a Gaussian spectrum with a FWHM energy spread of 40 MeV and a central energy of 120 MeV. In the experiment, the spectrum had a central energy of approximately 90 MeV with a FWHM energy spread of 50 MeV and a slightly larger

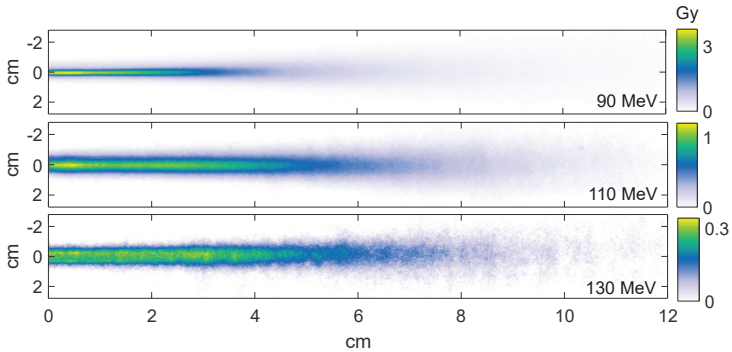

Figure 3.28. *Radiochromic films (EBT3) irradiated with electron beams (accumulation of 10 beams on each film) for different focusing energies. The EMQ triplet was set to focus 90 MeV (top), 110 MeV (middle) and 130 (MeV) at 11 cm behind the front edge of the film.*

focal spot size.

The phantom used to obtain the results shown in Figure 3.26 is cylindrical and 8 cm in diameter, with stacked disks of radiochromic film (EBT3). Spacers of Perspex acrylic glass (water equivalence of 1.045), 2 mm in thickness, were used between the outermost layers. The laser-plasma-accelerated electron beam was controlled with the EMQ triplet in a 1-to-1 imaging configuration as described in Section 3.9.2. This resulted in a charge uncertainty of less than 1 %, a spatial uncertainty of 0.1 mm and a spatial size of 2.3×2.6 mm^2 (at the phantom), while still propagating over 20 cm in air before reaching the phantom. Figure 3.27 shows the dose distribution for a focused electron beam and an unfocused beam, illustrating the much smaller beam size. The improved charge stability compared to an unfocused beam can probably be attributed to the the fact that only electrons of a certain energy can pass through the EMQ triplet. Due to the high spatial accuracy, the target volume region could be kept very small, about 100 times smaller than in a typical stereotactic treatment, larger volumes can be radiated by scanning the pencil beam.

The effect on the dose deposited for various electron energies focused at a certain distance is shown in Figure 3.28. In each case, the beams are focused 11 cm behind the front edge of the phantom. This focal distance was set for either 90, 110 or 130 MeV electrons. In each case, data were accumulated from 10 electron beams, accelerated using shock-assisted ionization injection [39], resulting in a spectral peak at ~ 80 MeV (see Figure 3.29) and a FWHM energy spread of 20 MeV. The

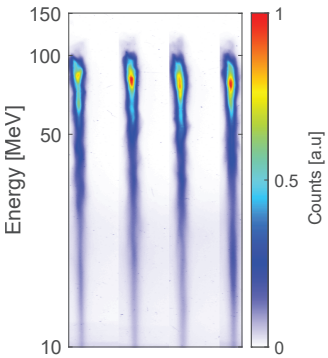

Figure 3.29. *Electron spectra by shock-assisted ionization injection from four consecutive laser shots.*

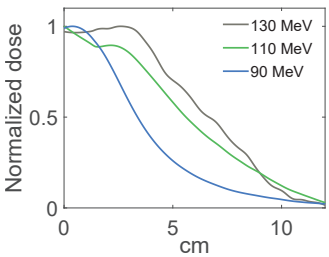

Figure 3.30. *Longitudinal dose on-axis of the electron beams show in Figure 3.28.*

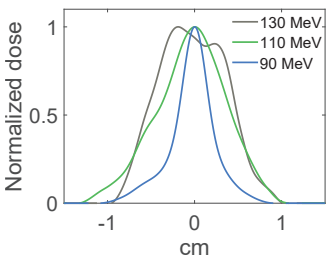

Figure 3.31. *Transverse dose at a depth of 2 cm (Figure 3.28). When focusing 130 MeV electrons the spatial distribution is almost top-hat shaped.*

beam widens at the front edge of the phantom when focusing 110 and 130 MeV as different energies are focused in different planes. For the 130 MeV beam, the spatial distribution is almost top-hat shaped for the first 3 cm in the phantom (see Figure 3.30 and 3.31). One possible explanation of this is that lower-energy electrons are focused earlier in the phantom. As these also scatter more (as the angular scattering power is proportional to $1/E_K^2$) this stronger focusing might help mitigate the overall beam divergence in the phantom. However, the statistics were poor in this case, as there are very few electrons with an energy of 130 MeV and further studies together with simulations will be required to make a more complete analysis.

In the study described in Paper II, a more continuous electron spectrum was used (ionization injection). The point at which 50 % of the total dose was deposited, R_{50}, could be controlled longitudinally by changing the position of the longitudinal focal point of the electron beam. Note that in this case, the energy being focused was constant but not the focal point position, i.e. the opposite to the case shown in Figure 3.28.

As mentioned above, any reasonable fluctuation in electron beam pointing or change in divergence will be mostly corrected for by the 1-to-1 imaging configuration of the EMQ triplet. The electron beam pointing (measured as the distance from the laser axis) improved by a factor 20 using this configuration while the beam area at the phantom was decreased by a factor 8 (Paper II). The combination of an increased R_{50}, high spatial accuracy and small beam size allowed a considerable difference between the dose deposition in the target volume and the organ-at-risk volume of ~ 50 Gy at 25 fractions in the phantom (see Paper II and Figure 3.26).

3.11.1 Dose calibration

Radiochromic film, which consist of an active layer that darkens when exposed to radiation between two transparent polyester substrates, is commonly used to measure dose deposition. To reliably measure the change in optical density due to exposure of the radiochromic film to radiation, a flatbed scanner was used with 16-bit colour channels. Furthermore, a large scanning area is desirable to avoid any gradients that may arise from the lamps in the scanner. All scanners (even of the same model) vary slightly in their colour response so each individual scanner should be calibrated. This is done by exposing radiochromic film with a known dose to obtain a calibration curve that relates the net optical density in a certain colour

channel (red, green or blue), $OD_{net} = -\log_{10}(\frac{I}{I_0})$ to the dose. I_0 is the intensity obtained from an unexposed film and I that from an exposed film, preferably from the same batch. As the optical density increases, the sensitivity changes depending on which colour channel is used. For dose ranges between 0 and 6 Gy, the red channel is more sensitive, while the green channel is more sensitive at 6-35 Gy and the blue channel for 35 Gy and above [59]. Radiochromic films were irradiated using an ELEKTA Precise linear accelerator calibrated with an ion chamber according to the IAEA standard [60]. The red channel of the irradiated films are shown on the right in Figure 3.32. For each dose value, 3 irradiated films were averaged. The calibration curve obtained for the red channel of an Epson V800 photo-scanner using the calibration films is shown on the left in Figure 3.32. The calibration was used to obtain absolute values of the dose in Paper II.

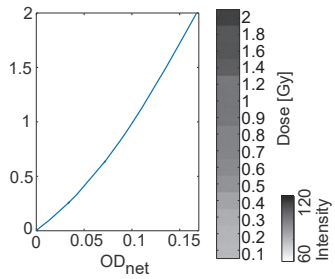

Figure 3.32. *Right: montage of irradiated radiochromic films, note that the y-axis is not linear, showing the intensity obtained by scanning the films. Left: calculated calibration curve for the red channel of an Epson V800 photo-scanner, obtained by the logarithm of the ratio between radiated films and the non-irradiated reference films (not shown).*

Chapter 4

Betatron X-ray generation, characterization and applications

X-rays have properties that make them useful in many applications. The most well-known property is probably their ability to pass through matter that is opaque to visible light, a property used in several areas, such as medical clinics and airport security. Furthermore, as X-rays scatter much less than visible light, the amount of X-rays absorbed in an object is directly related to the density and chemical composition of that object which is generally not true for visible light. This allows for a direct measurement of the density, something utilized in the studies described in Paper III and IV where the density of atomizing sprays is analysed. Furthermore, a very small X-ray source allows for density measurements in objects that have little absorption. This may seem counter-intuitive, but an object with very low absorption can still disturb the phase of the X-ray wavefront. This can be measured in phase-contrast imaging (PCI) and the magnitude of the phase shift is related to the refractive index of the object, from which the density can be calculated.

Many applications require a pulsed X-ray source, typically when something dynamic needs to be measured to avoid motion blur. Furthermore, it is generally desirable to have a small X-ray source as this results in a better spatial resolution, and a brighter X-ray source typically results in better contrast. However, all of these characteristics are generally inter-connected. A smaller X-ray source is dimmer than a larger source, a con-

tinuous source is brighter on average than a pulsed source and so on. Synchrotron facilities provide an X-ray source that is simultaneously small, bright and pulsed while laser-plasma accelerators are unique in the sense that they can produce a similar X-ray source (although with at a lower repetition rate) on a much smaller scale. The X-ray pulses from laser-plasma accelerators are also much shorter compared to synchrotron X-ray pulses.

This chapter briefly describes the electron motion in the plasma wake. First by assuming a constant longitudinal momentum, while later including a linearly increasing momentum. This is followed by a section regarding betatron radiation and its typical characteristics.

Two common methods to characterize a LWFA X-ray source are described, together with some experimental results. The first is a method to experimentally determine the X-ray spectrum from a wakefield accelerator using a Ross filter. The second method is used to measure the X-ray source size which relies on measuring the diffraction pattern created by a very thin object in the X-ray beam path. From this, the source size may be derived. This is accompanied with source size measurements performed at the Lund MTLF.

The final part of this chapter is dedicated to applications. It starts with radiography of fuel injector sprays, using betatron X-rays to obtain the liquid mass distribution, followed by a brief description of a complementary optical technique known as two-photon light induced fluorescence (2-p LIF) imaging.

A section on tomography follows, including both theory and experimental results. It shows the 3D liquid mass distribution from the fuel injector spray mentioned above, obtained by tomography, along with a tomogram based on phase-contrast images of a small lacewing. It ends with a short discussion on artefacts in tomography.

4.1 Generation of betatron X-rays

An off-axis electron inside the plasma wake experiences a focusing force towards the axis due to the transverse electromagnetic field. The equation of motion for an electron in a cylindrically symmetric cavity is governed by the relativistic Lorentz equation. Assuming the longitudinal moment to be constant, the electron orbit is given by [61]:

$$r \approx x_\beta \sin(k_\beta c t) \tag{4.1}$$

and

$$z \approx z_0 + \beta_k \left(1 - \frac{r_\beta^2 k_\beta^2}{4}\right) ct - \beta_k \frac{r_\beta^2 k_\beta^2}{8} \sin(2k_\beta ct) \qquad (4.2)$$

where $k_\beta = k_p/\sqrt{2\gamma}$. Here, r_β is the oscillation amplitude of the electron and β_k is the betatron wave number. For large oscillations, this results in a Lissajous trajectory, i.e. a figure-of-eight pattern in the moving frame which is analogous to an electron riding a plane wave with relativistic intensity [62].

A more realistic model can be obtained by including a longitudinal electric field, thus, the longitudinal momentum of the electron is no longer constant. This leads to an expanded equation of motion which can be solved analytically [63]. Figure 4.1 shows the electron trajectory for an initial transverse position of 1 µm, an electron density of 5×10^{18} cm^{-3}, an initial relativistic factor $\gamma_0 = 200$ and zero initial transverse momentum in the lab frame. Due to the longitudinal acceleration of the electron in this model, the oscillation amplitude decreases during propagation and the betatron frequency decreases.

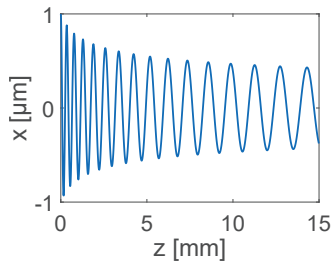

Figure 4.1. *Betatron oscillation of an electron, assuming a constant longitudinal electric field of 200 GV/m, i.e. the electron is experiencing a constant longitudinal acceleration over the distance shown here, linearly gaining energy.*

A charged particle under acceleration generates electromagnetic radiation. The oscillating electron in the plasma wake will thus radiate, and for non-relativistic particles, this radiation would be similar to that of a dipole antenna. However, due to time dilation for a relativistic particle, the radiation is folded into a forward-directed, narrow cone. Each particle radiates in a cone with an opening angle $\tilde{\theta} = 1/\gamma$, while the angle between the radiation cone and the electron path is $\theta = K/\gamma$ [61], resulting in a total divergence $D \approx K/\gamma$ (see Figure 4.2). The betatron strength parameter, K, is analogous to the undulator or wiggler parameter commonly used for insertion devices and is related to the plasma parameters by: $K = \gamma \omega_\beta r_\beta / c$.

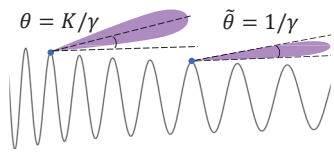

Figure 4.2. *The radiation forms an angle $\theta = K/\gamma$ with the electron trajectory and the radiation has an opening angle of $\tilde{\theta} = 1/\gamma$. Thus, radiation from higher-energy electrons is more collimated and forwardly directed.*

As a consequence of the radiation being forwardly directed, it will undergo a large Doppler upshift into the X-ray region. The trajectory in Figure 4.1 also indicates that the size of the X-ray source will be smaller for higher-energy electrons and the spectrum generated will likely contain more low-energy photons than high-energy photons (as the electron betatron frequency is higher for low-energy electrons, thus generating more radiation per unit time).

For a single electron, the energy spectrum of the radiation is given by [61]:

$$\frac{d^2 I}{dE d\Omega} = N_\beta \frac{3he^2}{\pi^3 c} \frac{\gamma^2 \zeta^2}{(1+\gamma^2\theta^2)} \left(\frac{\gamma^2\theta^2}{(1+\gamma^2\theta^2)} \kappa_{1/3}^2(\zeta) + \kappa_{2/3}^2(\zeta) \right) \qquad (4.3)$$

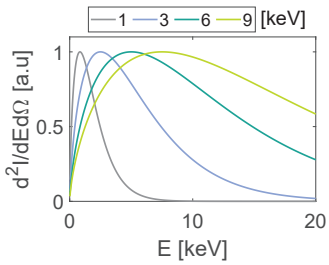

Figure 4.3. *Betatron radiation for critical energies of 1, 3, 6 and 9 keV.*

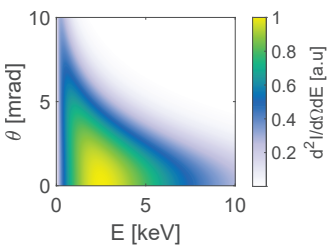

Figure 4.4. *Betatron radiation for different angles for an electron with $\gamma = 200$, corresponding to a critical energy of 3 keV.*

This is the radiation emitted within a photon energy bandwidth dE over the solid angle $d\Omega$. This assumes the observation angle $\theta \ll 1$ and $K \gg 1$. Here, $\zeta = (E/2E_c)(1+\gamma^2\theta^2)^{3/2}$, N_β is the number of betatron periods, κ is the modified Bessel function of the second kind and E is the photon energy. The critical energy is given by [61]:

$$E_c = \frac{3}{2}\frac{\omega_\beta^2 r_\beta \gamma^3 \hbar}{c} \tag{4.4}$$

Energy spectra for different critical energies are shown in Figure 4.3. The radiated energy for a single electron (assuming $\gamma \gg 1$) can be estimated from [61]:

$$W = \frac{2\pi r_e m_e}{3c} N_\beta \gamma^4 \omega_\beta^3 r_\beta^2 \tag{4.5}$$

where r_e is the classical electron radius.

As an electron will radiate at each oscillation peak, the duration of the pulse is related to the duration that the radiation cone is directed towards the observer, which in turn depends on the radius of curvature, ρ, of the electron oscillation and the electron velocity. For a single electron, the pulse duration for a single oscillation can be approximated by $\tau_e \approx \rho/24\gamma^3 c$ [64] which is typically a very short duration. For an electron bunch, each electron will contribute a pulse of this duration. Therefore, the total pulse duration will be the convolution of the temporal profile of the electron bunch (typically of the order of a few fs) and the contribution from each electron (which is several orders of magnitude shorter). Therefore, a good approximation is that the radiation pulse duration is similar to the electron bunch duration, typically a few fs [64, 65].

As the electrons will be randomly distributed in space in the plasma wake, the radiation will add incoherently, i.e. the energy spectrum from an electron bunch of N_e electrons will be the sum of the radiation from each electron, and Equation 4.3 is simply multiplied by N_e [64].

4.2 X-ray source characterization

4.2.1 X-ray spectrum

As discussed in Section 2.4.3, the X-ray spectrum can be obtained by single-photon counting provided the X-ray intensity is sufficiently low. However, a simpler and more common method is to use a Ross filter [66]. This method requires an assumption regarding the shape of the spectrum, which has been shown to be synchrotron-like and well defined by the critical

energy [67]. For a specific material with known transmission (referred to as a filter here), the integrated spectrum should therefore match the experimentally measured transmission for that filter. The best estimated critical energy is thus the critical energy that minimizes the expression:

$$\delta(E_c) = \sum_i (\tilde{T}_{i,E_c} - \hat{T}_i)^2 \tag{4.6}$$

where $\hat{T}_i$ is the measured normalized transmission for filter i and $\tilde{T}_{i,E_c}$ is the normalized theoretical transmission of filter i for different critical energies:

$$\tilde{T}_{i,E_c} = \frac{\int_0^\infty N(E) Q_E T_t T_i dE}{\int_0^\infty N(E) Q_E T_t dE} \tag{4.7}$$

and T_i is the theoretical transmission of filter i. The normalized energy spectrum on-axis is given by:

$$N(E) = \left(\frac{E}{2E_c} \kappa_{2/3} \left(\frac{E}{2E_c} \right) \right)^2 \tag{4.8}$$

which follows from Equation 4.3 by assuming $\theta = 0$. The transmission between the source and detector, T_t, is also taken into account. This includes all materials (including air), such as windows, foil substrates etc, but not the transmissions of filter T_i. Finally, Q_E is the quantum efficiency of the detector.

Experiment at the Gemini laser

An experiment aiming to generate and probe warm dense matter using X-ray absorption near edge structure was performed using the Gemini laser (a 15 J, 30 fs Ti:sapphire system) at the Rutherford Appleton Laboratory, UK. Data analysis from this experiment is still ongoing, however, some preliminary X-ray spectra analysis was performed remotely based on the method mentioned above.

Figure 4.5 shows an X-ray image of a Ross filter obtained with a single X-ray pulse using the Gemini laser. The filter is made from different materials arranged in a grid, namely, V, Fe, Co, Zn, Mo, Pd and Sn. Note that there are two filters of each material. In order to obtain the normalized transmission, several sample points are taken in the areas between the filters in Figure 4.5 and the background is interpolated to obtain a beam profile as it is generally not uniform. Using Equation 4.6, the critical energy that minimizes $\delta(E_c)$ was found to be 15.6 keV for the shot shown in Figure 4.5 (see Figure 4.6). The obtained normalized spectrum is shown in Figure 4.7.

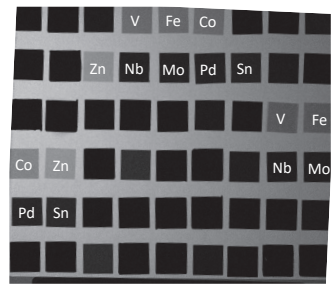

Figure 4.5. *An X-ray image of a Ross filter.This particular filter has some additional transmission filters used in a different analysis. The Ross filter includes* 10.8 *μm vanadium (V),* 6.4 *μm iron (Fe),* 5.3 *μm cobalt (Co),* 4.7 *μm zinc (Zn),* 125 *μm niobium (Nb),* 100 *μm molybdenum (Mo) and* 69 *μm palladium (Pd).*

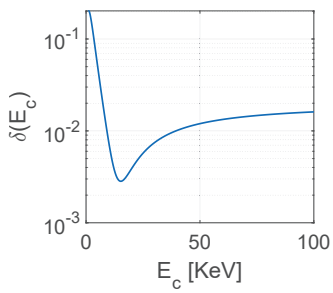

Figure 4.6. *Total residual $\delta(E_c)$, showing a minimum for $E_c = 15.6$ keV.*

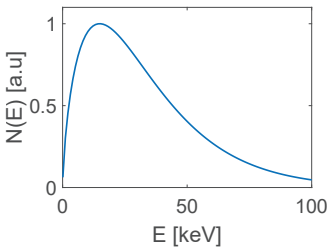

Figure 4.7. *Synchrotron spectrum for $E_c = 15.6$ keV.*

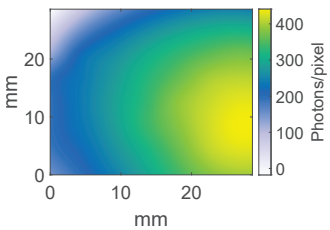

Figure 4.8. *X-ray spatial distribution, yielding 1×10^{13} photons/sr.*

For every eV of X-ray energy deposited, the X-ray camera (Andor Ikon-L SO) produces 0.274 electron-hole pairs on average. For the camera settings used in this case (high capacity mode, 1 MHz read-out, pre-amp $\times 1$), every 21.4 electron-hole pairs generate 1 camera count on average, thus every 5.9 eV of X-ray energy will generate 1 count. Since the shape of the energy spectrum is known, the number of photons per count, p, can be estimated by normalising the integrated energy spectrum to the integrated camera count, C. The number of photons per pixel (assuming $m \times n$ pixels) is given by:

$$N_p = C \cdot \frac{p}{m \cdot n} \tag{4.9}$$

and

$$N_\Omega = \frac{N_p}{d^2/s^2} \tag{4.10}$$

is the number of photons per steradian on-axis, where s is the source-detector distance and d is the pixel size. In this case, the photon yield is $N_\Omega \approx 1 \times 10^{13}$ sr^{-1}. The X-ray beam profile, together with the number of photons per pixel is shown in Figure 4.8.

There is some uncertainty in the manufacturing process of the filter foils which could influence the estimated critical energy. In the analysis described above, the thickness of the foils was assumed to be that which was specified to the manufacturer. This can be accounted for by calculating the theoretical transmission (Equation 4.7) for a randomly selected filter thickness within the manufacturing uncertainty and calculating the residual $\delta(E_c)$ (Equation 4.6) for every combination of filter thickness, essentially a Monte Carlo simulation. The results of this is shown in Figure 4.9, where a simulation was performed using 500 randomly sampled filter thicknesses for the shot which was analysed above. The deviation from the nominal filter thickness for each filter is shown in orange and green in Figure 4.9. As there are two sets of each filter, they are labelled $t1$ and $t2$. The uncertainty due to the variation in filter thickness gives an uncertainty in the critical energy of 5.2 keV (shown by the blue area in Figure 4.9). By selecting the set of filter thicknesses t that minimizes the set of $\delta(E_c)_t$ equations, a critical energy of 17.8 keV was obtained, instead of the previously obtained value of 15.7 keV.

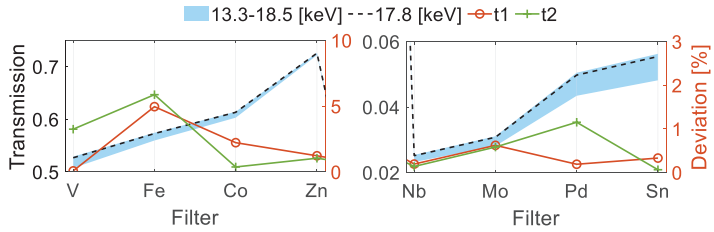

Figure 4.9. *Monte Carlo simulation for varying filter thickness. The black dashed line shows the best fitted E_c, while the blue area shows the uncertainty in transmission due to varying filter thickness. The deviations from the assumed filter thickness, $t1$ (orange), and $t2$ (green), that result in the best fitted E_c.*

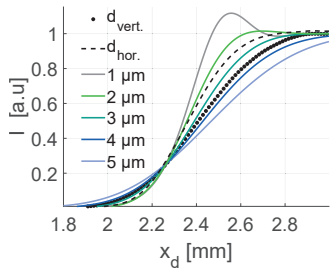

Figure 4.10. *Calculated diffraction patterns for different source sizes (solid lines) and measured values (dashed lines).*

4.2.2 X-ray source size

One way to measure the X-ray source size is to use a thin, high-Z wire, such as a tungsten wire. The diffraction pattern produced by the wire is related to the source size by [68]:

$$I_s(x_d) = \int_{-\infty}^{\infty} B(x_s)\tilde{I}(x_d + x_s\frac{r_2}{r_1})dx_s \qquad (4.11)$$

where r_1 is the source-wire distance, r_2 the wire-detector distance, x_s the transverse coordinate of the source and x_d the transverse coordinate of the detector. The source distribution is described by the Gaussian function $B(x_s)$ and the diffraction pattern from a polychromatic source is $\tilde{I}(x_d)$.

The source size is obtained by solving Equation 4.11 for several different source sizes, minimizing the RMS of the difference between the calculated and the measured diffraction pattern. Figure 4.10 shows the calculated diffraction pattern for several source sizes together with measured data. In this case, the best fit was achieved for a source size of 2.6×3.6 µm^2 in the vertical and horizontal directions respectively. It should be noted that the source size is measured to be larger in the polarization direction of the laser. This is to be expected due to direct laser acceleration, where the driving laser field can overlap with some electrons in the wake, increasing the oscillation amplitude in the direction of the polarization [9, 69].

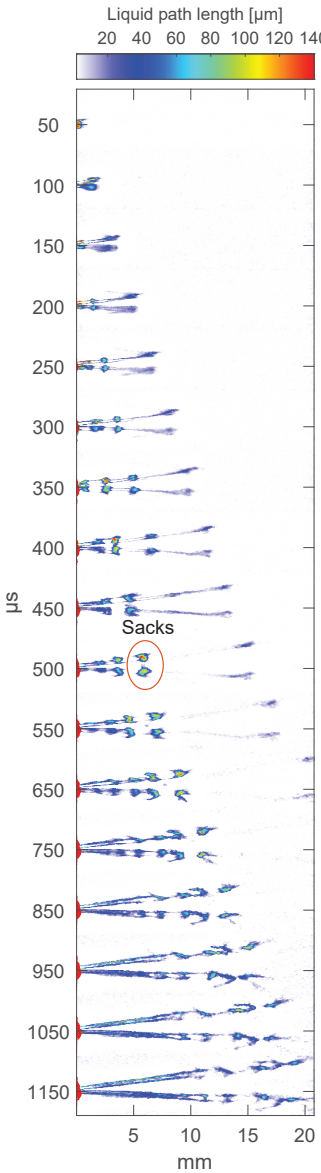

Figure 4.11. *Radiograms of a fuel injector spray at different times after injection. The colour represent the liquid path length.*

4.3 Combining X-ray radiography and optical measurements in atomizing sprays

The atomization of a spray, i.e. the process of liquid bodies breaking up into smaller drops before the rapid liquid-to-gas transition, is of great importance in many applications. This is especially true for fuel injectors in combustion engines as the efficiency of the combustion and the level of pollutants are both highly dependent on this process. One of the current challenges in measuring the liquid mass is reducing multiple light scattering to obtain quantitative values. This can be done with existing techniques using structured visible light in low-density regions [70], such as low-density sprays or at locations far away from the nozzle. However, in high-density regions optical techniques are inadequate due to multiple scattering. The refractive index of the liquid is close to unity for keV X-rays, resulting in little or no scattering and refraction which allows for much more accurate measurements compared to optical techniques.

A very bright and relatively small X-ray source with a short pulse duration is necessary to image the spray jets. The size of the X-ray source mainly limits the resolution, as a larger source introduces blurring (especially at large magnifications), while the brightness influences the contrast and the signal-to-noise ratio (SNR). The pulse duration must be short enough to not introduce motion blur, which depends on the velocity of the liquid and the image magnification, and is typically in the μs range. As a result of these requirements, the majority of studies on the liquid mass distribution in spray jets have been performed at synchrotron facilities [71–73]. The studies presented in Papers III and IV illustrate the use of a plasma-based accelerator for making quantitative measurements of the liquid path length and liquid mass. Synchrotron facilities have a high flux and repetition rate, but the X-ray beams are small and collimated. Therefore, measurements on a fuel injector spray must be made by raster scanning, while laser-plasma generated X-rays have a larger divergence, which means the beam can cover the whole region of the spray fully, with the additional benefit of image magnification.

Radiography relies on the fact that different materials have different absorption coefficients. The transmission through a material is given by the generalised Beer-Lambert law:

$$T = \int_0^\infty e^{-\alpha(E)} S(E) dE \tag{4.12}$$

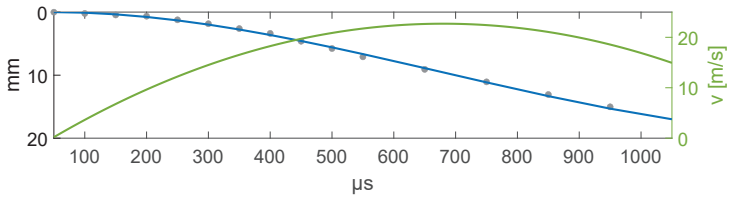

Figure 4.12. *The positions (blue) of the mass centre of the sacks indicated in Figure 4.11 together with the calculated velocity (green).*

where $\alpha(E)$ is the absorption and $S(E)$ the normalized spectrum at the detector, i.e. including losses due to materials in the beam path and the detector quantum efficiency. The absorption is $\alpha = \int_0^l \mu(E)dz$ where μ is the attenuation coefficient and l is the interaction length between the X-ray beam and the material, usually referred to as the path length. The absorption coefficient depends on the mass density $\rho(l)$ as $\mu = \rho(l)N_A\sigma_a/A$, where A is the atomic mass number and σ_a is the absorption cross-section.

The time evolution of a commercial fuel port injector (Paper IV) is shown in Figure 4.11, where each radiogram in the montage is an average of 50 images. This injector works at a relatively low pressure (4.5 bar) which results in larger liquid bodies before they break up and evaporate further away from the nozzle. The nozzle is located on the left-hand side of the image and the spray jets are moving from left to right. The false colours indicate the liquid path length. Two liquid "sacks" are formed early on, followed by two more sets of separated liquid bodies, the second of which rapidly atomizes while the third contains more mass and seem to atomize more slowly. The third set of sacks (indicated by the orange ellipse) can be followed over the recorded temporal evolution. By locating the mass centre of these sacks, their position can be tracked and a velocity can be calculated (see Figure 4.12). Furthermore, the liquid velocity within the sack does not appear to be uniform, as the sacks become elongated over time.

In the study described in Paper IV, X-ray radiography was combined and synchronized with 2-p LIF optical imaging, which provides a complementary measurement of the atomizing spray. In 2-p LIF, a combination of fluorophore and laser wavelength is chosen so that a single photon does not carry enough energy to excite the dye. The probability for fluorescence is therefore proportional to the squared laser intensity [74], as it requires two or more photons to be absorbed sim-

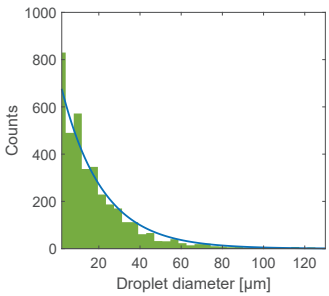

Figure 4.14. *Histogram of the counted droplets indicated in Figure 4.13 binned by droplet diameter.*

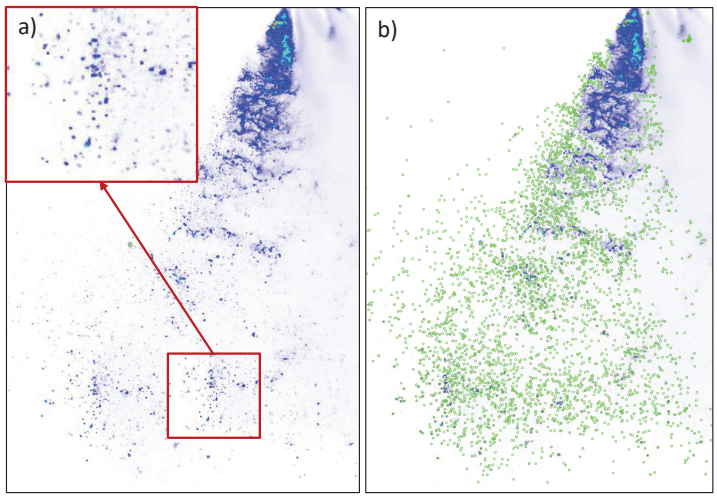

Figure 4.13. *a) A 2-p LIF image where several microscopic droplets can be seen. b) The droplets that were counted (green) and binned in the histogram in Figure 4.14.*

ultaneously. Using a cylindrical lens to focus the laser beam to a sheet, the excitation can be localized in the imaging focal plane to obtain high-resolution images. Furthermore, it also reduces the amount of multiple-scattered light detected as these photons do not carry enough energy to induce fluorescence.

Figure 4.13 shows a 2-p LIF measurement, where each droplet was automatically identified (shown in green) and its diameter measured. This was compiled into a histogram such as that shown in Figure 4.14. The droplet size is important in determining the rate of evaporation and provides complementary information to the liquid mass distribution.

4.4 X-ray tomography

As stated above, radiography can be used for non-destructive measurements of an object's projected density. However, tomography is needed to measure the local density distribution quantitatively in 3D space. In simple terms, a tomographic reconstruction uses projection images at different angles to reconstruct the object in 3D space.

The Fourier slice theorem states that [75, 76]: "The Fourier transform of a parallel projection of an object at an angle θ equals a line in a 2D Fourier transform of the object at the same angle." Thus, sampling the object over 180 degrees res-

ults in the full 2D Fourier transform and the object can be reconstructed. One, perhaps not obvious issue, is that this essentially maps an object in Cartesian space onto a polar coordinate grid in the Fourier plane and vice versa for the inverse transform. This requires some interpolation and an uncertainty in the frequency space will affect the whole image. More importantly, it means that the lower spatial frequencies have a much higher sampling density than the higher spatial frequencies, whereas, ideally, the sampling density should be uniform (see Figure 4.15). This leads to the well-known filtered back projection, where the object is reconstructed by [77]:

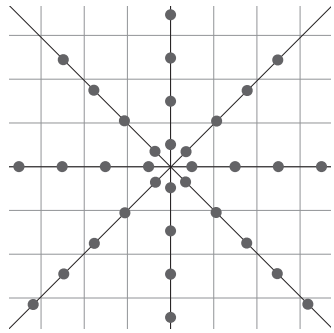

Figure 4.15. *Projection data are sampled in Cartesian space but transformed into polar space, resulting in under-sampling of higher spatial frequencies.*

$$f(x,y) = \int_0^{\pi} \int_{-\infty}^{\infty} P(\omega,\theta)|\omega| e^{i2\pi\omega(x\cos\theta + y\sin\theta)} d\omega d\theta \quad (4.13)$$

where $P(\omega,\theta)$ is the Fourier transform of the projection at angle θ. The filtered back projection applies a weighting function, $|\omega|$, to correct for the non-ideal sampling density, (see Figure 4.16), which acts as a high-pass filter. This function is also known as the inverse Radon transform (excluding the filtering term $|\omega|$), which is closely related to the Abel transform discussed in Section 2.4.1. The main difference between the two methods is that the Abel transform assumes cylindrical symmetry, while the Radon transform does not.

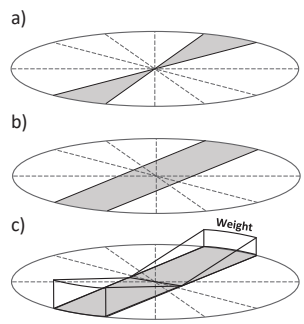

Figure 4.16. *a) Ideal Fourier space of projection data. b) Actual Fourier space obtained from projection data. c) Weighting function used to approximate the actual data in b) to the ideal case in a).*

Tomography was used to study a high-pressure gasoline direct-injection spray (200 bar) in the high-density region close to the nozzle (Paper III). In this study, the number of projection angles was kept rather low and cubic-spline interpolation was used in the sinograms to account for this. The reconstruction was computed using the filtered back projection algorithm. Figure 4.17 shows a raw radiogram, averaged over 25 shots together with five tomographic slices and contour levels at different liquid volume fractions. The liquid volume fraction is the percentage of liquid contained within a voxel.

The projected thickness obtained from phase-contrast images (see Section 4.5) of a lacewing was calculated at several angles (Paper I). A 3D reconstruction of the specimen was obtained using the filtered back projection, as shown in Figure 4.18.

4.4.1 Artefacts in tomographic reconstruction

Artefacts in a tomogram can have several different appearances and origins. They are usually categorised as streaking, shading, rings or bands. Streaking artefacts can arise from speckle noise (sharp local intensity variations) in the projection image, which

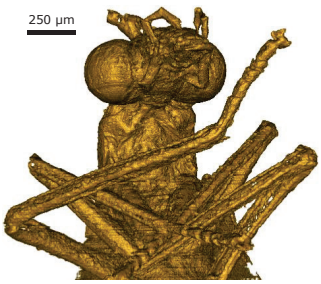

Figure 4.18. *Tomogram of a lacewing.*

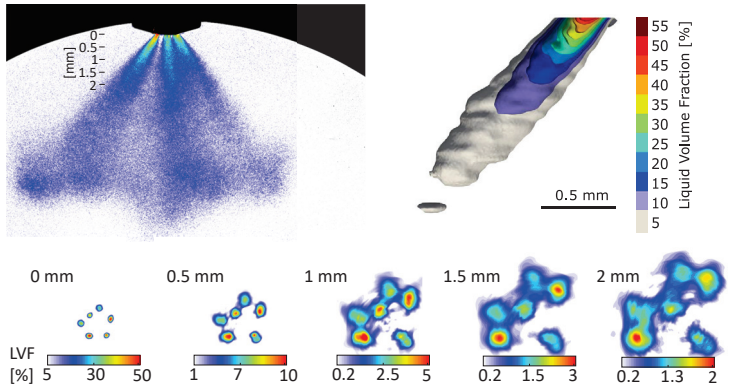

Figure 4.17. *Top left: X-ray radiogram (average of 25 shots) where the heights of the tomographic slices (bottom row) are indicated. Top right: Contour levels of the liquid volume fraction (LVF) for the left-most jet.*

will translate into streaks across the reconstructed image. This noise is further enhanced as the filtered back projection acts as a high-pass filter, reducing the SNR in the filtered projection. This artefact is common with polychromatic X-ray sources as the amount of high-energy photons is typically much lower than the amount of low-energy photons. As the signal generated on the CCD is proportional to the X-ray energy deposited, these few high-energy photons generate a stronger signal in the pixel where they are detected, resulting in Poisson noise.

Shading artefacts are similar to streaking artefacts, but whereas streaking artefacts occur for a single projection, shading artefacts occur when there is a slowly varying error over several projections. Essentially, this produces wide and smooth streaks instead of small and sharp streaks, as in streaking artefacts. As the name implies, ring artefacts appear as a ring in the final tomogram. This occurs when an error persists over several angles; for instance, a pixel on the detector that is consistently bright over all angles would appear as a ring in the tomogram.

Suppressing Poisson noise when imaging atomizing sprays poses a unique challenge, as the small droplets themselves produce a signal that resembles Poisson noise (see for instance Figure 4.17). Therefore, it is hard to obtain a calculated value on the performance of an applied filter, and in many cases it seems better to rely on the human eye. During this work, it was found that a non-local mean filter [78] works well for suppressing Poisson noise, especially for X-ray radiograms of

atomizing sprays, which was applied before the tomographic reconstruction in Figure 4.17.

As a polychromatic X-ray beam propagates through a sample, the lower-energy photons are predominantly absorbed as the attenuation coefficient rapidly increases at lower energies. This shifts the mean X-ray beam to higher energies, "hardening" the beam. This means that the intensity in the projection image is no longer proportional to the path length, which introduces beam-hardening artefacts. In fact, the measured path length is always less than the actual path length for a polychromatic X-ray source for this reason. These artefacts are generally difficult to identify as they appear as a smooth gradual density distribution with no apparent non-physical boundaries or features. In the case of significantly denser internal objects they will appear as shadows where the dense objects align. However, if the X-ray spectrum is known, these artefacts can be corrected for, as was done for all tomographic reconstructions presented here. It should be noted that only a few of the artefacts encountered in tomography are mentioned in this section. The reader is referred to [75] for a deeper discussion of the topic.

4.5 X-ray phase-contrast imaging

For an object that is only weakly absorbing, or multiple objects with similar absorption, X-ray radiography will yield very poor contrast and PCI is a more suitable technique in such cases. Radiography relies on measuring the imaginary part of the complex refractive index, $n = 1 - \delta + i\beta$, where β is the extinction coefficient, i.e. the absorption. The real part, $1 - \delta$, indicates the phase velocity (or phase change factor), which can differ for materials with similar absorption, providing much greater contrast than radiography. This is especially important in biological tissue where the absorption cross-section is very small, while the phase shift cross-section can be orders of magnitude larger. The phase shift in the X-ray wavefront, ϕ, is proportional to the projected thickness, Γ, of a traversed object and is given by [79]:

$$\phi(\mathbf{r}) = \frac{-2\pi}{\lambda}\delta \cdot \Gamma(\mathbf{r}) \tag{4.14}$$

However, this phase perturbation must be converted into an intensity perturbation in order to be measured. This can be done by various interferometric techniques [80–82], but the simplest method is based on free space propagation. If the propagation

Figure 4.19. *Projected thickness, $\Gamma(r)$, calculated using Equation 4.15. The sample is the head of a bee which was glued onto a needle. Some of the glue is visible in the upper right part of the image.*

distance is sufficiently long (generally a few metres) the phase shift translates into an intensity modulation [83]. This method is known as propagation-based or in-line PCI. Although the modulated intensity is detected, a phase-retrieval algorithm is needed to convert this information into phase information. Different situations allow the use of different algorithms [84]. In the case of a sample consisting of a single, known material, the projected thickness can be retrieved by [79]:

$$\Gamma(\mathbf{r}) = -\frac{1}{\mu}\ln\left(\mathcal{F}^{-1}\left(\mu\frac{\mathcal{F}(M^2 I_d(M\mathbf{r}))/I_0}{d\delta|\mathbf{k}|^2/M+\mu}\right)\right) \tag{4.15}$$

where M is the magnification, $\mathbf{k}$ is the spatial frequency vector, i.e. $|\mathbf{k}|=\sqrt{u^2+v^2}$ where u, v are the spatial frequencies, $\mathbf{r}$ is the transverse position vector, I_d is the intensity at the detector, I_0 the intensity before the object and d is the distance between the sample and the detector. For a polychromatic source δ and μ must be replaced by:

$$\delta_{\text{eff}} = \frac{\int S(\lambda)\delta(\lambda)d\lambda}{\int S(\lambda)d\lambda} \tag{4.16}$$

where $S(\lambda)$ is the detected X-ray spectrum and μ_{eff} is calculated in the same manner as δ_{eff}.

Figure 4.19 shows the projected thickness of the head of a bee calculated from recorded phase-contrast images. Due to the divergence of the X-ray beam, a magnification of 10.3 is obtained, which allows some finer details to be resolved, such as the hairs shown in the enlarged image. These are of the order of 7-8 µm in width. The enlarged image is visibly blurred as a results of the high magnification in combination with the finite source size. It should be noted that Equation 4.15 resembles a low-pass filter in the Fourier domain, which may also reduce the image sharpness to some extent.

Phase-contrast imaging requires a coherence length $l_c = \lambda s/\sigma$ greater than $1-10$ µm [85]. Here, σ is the size of X-ray source and s is the source-detector distance. For the results shown in Figure 4.18 and 4.19, these values were: $\sigma \approx 3$ µm, $s = 2.1$ m and $\lambda \sim 6$ Å, resulting in $l_c \sim 400$ µm. Generally, this means that the X-ray source must be very small, of the order of a few µm. The choice of X-ray source is therefore limited to either microfocus X-ray tubes, which have a relatively low X-ray flux, synchrotron facilities, or laser-plasma based sources.

In-line PCI was used in the study described in Paper I to perform tomography of a small Chrysopa (lacewing) specimen

and the projected thickness was obtained using Equation 4.15. In this study, the X-ray spectrum had a lower critical energy than in similar, previously reported studies [86, 87], which increases the sensitivity due to the inverse wavelength scaling for the phase shift. Features as small as 4 μm could be distinguished in the raw phase-contrast images while features of the order of 10 μm could be resolved in the final tomogram. The reduction in resolution is probably due to the low-pass filtering nature of Equation 4.15 and the filtered back projection, as discussed in Section 4.4.

Chapter 5

Proton and ion acceleration

The prospect of laser-driven proton and ion acceleration is largely driven by potential applications in isochoric heating, inertial confinement fusion, radiography, warm dense matter probing and hadron therapy [88, 89]. Many of these applications place stringent requirements on the ion source in terms of its energy, spectral distribution, temporal distribution, beam divergence and efficiency.

As mentioned in Section 3.11, cancer tumour control is based on the higher repairability of healthy tissue than cancerous cells. Radiotherapy using protons has the significant advantage of dose-depth control, as protons mainly deposit their energy at the Bragg peak, the position of which is energy dependent. It is therefore possible to spare healthy tissue to a much greater extent than when using other kinds of radiation and proton therapy has been shown to be less likely to cause severe side effects than photon therapy [90]. This is especially important for older and sicker patients where side effects can be problematic. However, the lateral scattering of protons can limit the dose conformality [91]. Using heavier ions will result in less scattering due to their greater mass, and carbon ions have some additional benefits as they have a higher linear energy transfer than photons and protons. The amount of energy per unit length an ionizing particle transfers is an important quantity as the relative biological effectiveness increases as this increases [92].

Despite the advantages of hadron therapy there are currently only 110 machines worldwide for light ion therapy and even fewer for heavy ion therapy [49]. This can be compared to electron and photon therapy machines, which number more than 14,000 worldwide [49]. This discrepancy can pos-

sibly be explained by the "incremental cost-effectiveness ratio", which describes the ratio between the difference in treatment efficiency and treatment cost for radiotherapy treatment and chemotherapy. The investment cost of hadron therapy is huge, as the machines are very expensive compared to equipment used for other treatment methods. The incremental cost-effectiveness ratio is commonly compared to the quality-adjusted life-years (QALY), where each year of life is multiplied by a weighting factor that reflects the quality of life. In the literature, values of $50,000 - 100,000$ USD are generally used as the cost-efficiency threshold (i.e. the amount of money that should be spent per QALY), and these values are currently too high for proton therapy. A recent study showed that, although the incremental cost-effectiveness ratio varies greatly for hadron therapy, from $54,000$ to $1,500,000$ USD /QALY, the median was $361,000$ USD, which is significantly above the threshold [93]. One way to reduce the cost per QALY for hadron therapy would be to develop alternative particle acceleration schemes that reduce the initial cost. Laser-plasma acceleration by target-normal sheath acceleration (TNSA) is a possible candidate. Although some cancers, such as ocular cancer (eye cancer) can be treated using ion energies ~ 60 MeV [94, 95], most require higher ion energies ($\sim 200 - 250$ MeV) [96]. These energies are not yet possible to reach using TNSA and a research effort is therefore required to improve the efficiency of the TNSA process or to find other particle acceleration schemes.

5.1 Principle of target-normal sheath acceleration

In TNSA, a high-intensity laser pulse interacts with a thin solid target (a foil). Due to various interactions, electrons close to the surface gain kinetic energy from the laser pulse and are accelerated into the foil. These hot electrons propagate through the bulk of the foil and escape the target rear-side, leading to the formation of a dense charge-separation sheath at the rear side of the target. This charge separation generates an electric field, of the order of TV/m, which is strong enough to ionize local atoms in any contamination on the foil surface and accelerate the ions in a direction normal to the rear surface. This contamination layer is always present unless the foil is carefully treated and typically consist of some residual water vapour and hydrocarbons. Protons are predominantly accelerated as they have the highest charge-to-mass ratio compared to

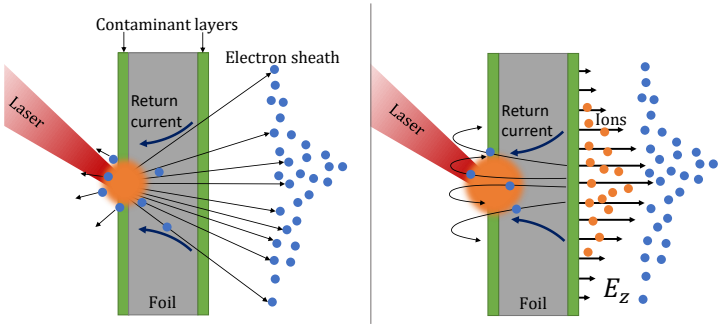

Figure 5.1. *Left: electrons close to the surface of the incident laser pulse will be driven through the foil. Right: the electric field that forms between the foil and electron sheath can reach TV/m, which ionizes any contaminants on the foil (such as water vapour). These ions will be accelerated in a direction normal to the foil surface by the strong electromagnetic field. Electrons reaching the target rear side after the formation of the sheath are reflected back towards the front surface and can be recirculated if the target is thin enough.*

any other ions and they may also shield the heavier ions from the electron sheath. After the initial formation of this sheath, any subsequent electrons reaching the rear of the target will be reflected back towards the front-side by the strong electric field and will recirculate [97]. These electrons will go back and forth through the foil, and if the density of the sheath decreases, they may escape the target rear side and help sustain it.

The large amount of hot electrons propagating through the target represents a significant current density. In response to this, a balancing return current will flow in the opposite direction and the conductivity of the material limits the fast electron transport [98].

A thinner target will result in less scattering of the hot electrons while they propagate through the bulk of the foil and will produce a more spatially localized sheath and a stronger accelerating field. For target thicknesses t of a few $\sim$ µm, the electron density in the sheath is $n_{sheath} \propto t^{-2}$ [99]. This motivates the use of ultra-thin targets (< 5 µm), which require a very high laser pulse contrast as the ASE pedestal can be intense enough to significantly deform or destroy ultra-thin targets before the main pulse arrives. Some preliminary experiments were performed at the Lund MTLF using a double plasma mirror (DPM). When the DPM was bypassed, resulting in a laser contrast of $\sim 10^{-8}$, no ions were observed for 0.5 µm foils and thinner. Figure 5.2 shows the maximum proton energy for several target thicknesses using the DPM where

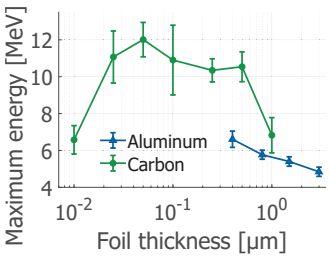

Figure 5.2. *Maximum proton energy for different foil thicknesses of aluminium and carbon using a high-contrast laser pulse, produced using a double plasma mirror.*

ions were observed down to a foil thickness of 10 nm. Note that foils thinner than 10 nm thickness were not investigated due to the lack of such targets at the time, and not due to a lack of signal. For 1.5 μm Al foils, using the DPM increased the ion flux by an order of magnitude and almost doubled the ion cut-off energy, from 3.2 MeV to 5.5 MeV (not shown here).

5.1.1 Conversion from laser energy to electron energy

The electromagnetic field from the laser is strong enough to resonantly drive a plasma wave over the plasma skin depth which will heat electrons through Landau damping [100]. However, this can only occur for a P-polarized wave at non-normal incidence when a significant pre-plasma is present [101], i.e. the plasma created by the leading edge of the laser pulse. In the case of a high laser contrast, a smaller pre-plasma is formed and vacuum heating becomes more dominant, as the electrons at the plasma surface are accelerated away from the target by the P-polarized laser field. Half a laser period later, the electrons will be accelerated towards the target and penetrate far beyond the skin depth due to their increased kinetic energy. This effect is maximized at an angle of incidence of 45° [102]. This was utilized in the study described in Paper VI.

An extension of vacuum heating occurs for relativistic laser intensities ($I > 10^{18}$ W/cm^2) through $\mathbf{J} \times \mathbf{B}$ heating, where the vacuum heated electrons quickly reach relativistic velocities and constitute a current density $\mathbf{J}$. The $\mathbf{v} \times \mathbf{B}$ term in the Lorentz force then becomes significant, and contributes to the oscillatory motion of the electrons, further increasing the electron temperature [103].

In conclusion, the efficiency of which the laser energy can be transferred to hot electrons depends on several factors, such as the laser intensity, the angle of incidence and the pre-plasma characteristics. One approach to further increase the energy of the accelerated ions is to increase the absorption of laser energy through various target designs. In the study described in Paper VI, targets with Cu nanowires of various lengths grown on gold substrates were used to improve the laser energy confinement. In addition, electrons from the edges of the nanowires may be heated through vacuum- and $\mathbf{J} \times \mathbf{B}$ heating, and be accelerated towards the target bulk by the laser field. For nanowires with optimal length (1 - 2 μm), the mean proton energy was increased by a factor of 2.

Chapter 6

Discussion and outlook

The success of laser plasma accelerators depends largely on the laser technology available. The development of several techniques, such as mode locking and CPA, has been necessary to reach the current stage. New techniques are constantly being demonstrated, and the field is rapidly expanding.

All the applications described in this thesis would benefit greatly from an increase in the laser repetition rate. The lasers available today capable of kHz repetition rate do not provide sufficient pulse energy to be relevant for applications such as VHEE radiotherapy or keV betatron X-ray generation [104]. The repetition rate of Ti:sapphire systems is currently limited by the pump lasers, the thermal load in the Ti:sapphire crystal and the gratings. One emerging and novel laser technique is the ultra-fast thin-disk laser [105], which has recently been shown to reach a pulse energy of almost 1 J at a 1 kHz repetition rate with sub ps pulse duration [106]. As mentioned in Section 3.2, in order to drive the plasma wake efficiently, the pulse duration must be matched to the plasma wavelength which is typically of the order of tens of fs. There are, however, schemes for multi-pulse LWFA that use high energy pulses with ps duration that are based on the phase modulation of the pulse into a pulse train to achieve matching condition, which has been simulated theoretically [107].

6.1 Radiotherapy

Radiotherapy using laser-plasma accelerated VHEE would benefit from an increase in repetition rate for several reasons. First, it would relax the demand on the charge variation in each

pulse. As the variations are random in nature, the standard deviation will decrease as $1/\sqrt{N}$. It is therefore preferable to administer the dose in smaller increments using more pulses, rather than in fewer pulses with large increments. Furthermore, the dose delivery time could be reduced to less than a second.

At very high dose rates ($>$ 40 Gy/s) studies have shown that the radiation damage to healthy tissue in animals is reduced, while the toxicity to the cancerous cells remain unchanged [108]. This biological effect is known as the "FLASH" effect. Several beneficial effects have been demonstrated, such as less severe skin reaction [109], reduced neurotoxicity in brain irradiation [110] and reduced levels of pulmonary fibrosis in lung irradiation [108]. In these studies, the total dose to the FLASH-irradiated group was the same as that to the conventionally treated group, and only the dose rate was changed. However, several studies have shown the absence of the FLASH effect at these high dose rates [111–113]. The mechanism behind the FLASH effect is still not fully understood. Currently available evidence points to several requirements on the radiation source for successfully inducing the effect: (i) the dose should be delivered in pulses, (ii) the total delivery time should be less than 100 ms, with at least 1 Gy per pulse (a few nC of charge) and (iii) the total dose should exceed 10 Gy [114]. Although current medical accelerators can be modified to achieve this [115], they still employ low-energy electrons which suffer from low penetration depth, as discussed in Section 3.11. Plasma accelerators can already produce beams with a mean energy above 200 MeV with a beam charge in the nC range [116, 117] but the repetition rate is still too low. Efforts are being made in the laser community to increase repetition rates, and several novel techniques are currently being investigated [118].

The ultra-short nature of laser wakefield accelerated electron beams makes it difficult to monitor the deposited dose in real time. The method currently used is based on ionization chambers, however, these have been shown to have a very low collection efficiency for higher dose rates, resulting in unreliable results [119, 120]. One solution could be to use integrating current transformers but these are relatively expensive and are sensitive to noise. A new real-time dose-monitoring system will probably have to be developed before clinical trials can be started using ultra-short VHEE beams.

6.2 Radiography of atomizing sprays

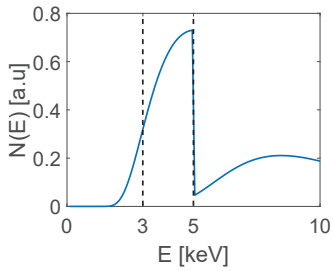

Figure 6.1. *Transmitted spectrum ($E_c = 2.7$ keV) through a 10 μm thick Ti foil.*

To increase the contrast in X-ray shadowgraphy of atomizing sprays, a contrast agent can be used that has a high absorption in the X-ray energy range of the probe beam. In the work presented in Papers III and IV, potassium iodide was added to increase the X-ray absorption. However, this changes the fluid dynamics as the viscosity and surface tension are altered. Therefore, it would be preferable not to have to use this additive while maintaining the performance. The X-ray energy of interest is generally below 4 keV as the amount of liquid being crossed by the X-ray beam is very low, together with the fact that most liquids do not absorb much at higher X-ray energies. For instance, 1 cm of ethanol gas has a transmission of ∼90 % at about 3 keV. Any higher-energy photons in the X-ray spectrum would thus mainly contribute to the Poisson noise, and they should therefore be discarded. This could be achieved using a crystal monochromator, for example, although the X-ray flux would also be reduced as only a narrow band of the spectrum would be reflected. Another option would be to use a filter, for example, a 10 μm thick Ti foil (or another suitable material) to act as a weak band-pass filter. Figure 6.1 shows a synchrotron-like spectrum with a critical energy of 2.7 keV after passing through such a filter. It can be seen that this preferentially transmits X-rays between 3 and 5 keV, which would be advantageous and easy to implement. A more complicated set-up could involve the use of a crystal to diffract the beam, followed by a square-pore microchannel plate. As the reflectivity is highly dependent on the angle of incidence, X-rays with higher energies would enter the microchannel plate at greater angles and be suppressed, while lower-energy X-rays would be transmitted, effectively functioning as a low-pass filter [121]. The cut-off energy could be tuned by changing the angle between the crystal and the microchannel plate.

Another aspect that should be improved is the X-ray flux onto the spray. In the studies performed here (Papers III, IV), the X-ray beam was larger than the spray, but collimating the beam would increase the flux. The results presented in Paper V demonstrate that it is possible to achieve highly collimated X-ray beams, reducing the divergence by at least a factor of 20 in solid angle, which would increase the flux by a similar amount. Furthermore, the ability to control the divergence would allow for the most optimal coverage for each spray as these may differ in size.

6.3 Medical X-ray phase-contrast imaging

Applications of PCI, especially in the medical setting, have been very limited so far due to the lack of suitable X-ray sources. In-line PCI requires a high transverse coherence, while other PCI methods, such as crystal interferometry or analyser-based PCI, require high monochromaticity. Furthermore, the absorption coefficient typically scales as $\mu \propto 1/E^3$ while the phase shift scales as $\phi \propto 1/E$ [122], where E is the photon energy, and in most medical applications of PCI, a significant amount of material lies between the region of interest and the source. The X-ray energy required is therefore several tens of keV. For example, PCI mammography has been successfully demonstrated with $\sim$ 20 keV X-rays from a synchrotron [123], resulting in very high sensitivity and specificity, while $\sim$ 30 keV is adequate for phase-contrast tomography [124]. PCI of cartilaginous tissue has also been demonstrated at an X-ray energy of 26 keV [125]. Although X-ray beams of these energies have been produced in wakefield accelerators [126, 127], they are usually produced using large laser systems, with a pulse energy of more than 10 J, which may not be suitable in a medical environment. Another option is to tailor the electron density profiles to optimize the betatron oscillations.

From Equation 4.4, it is evident that, in order to increase the critical energy of the X-ray beam, the electron oscillation frequency, ω_β, oscillation amplitude, r_β, or electron energy, γ, must be increased. The size of the plasma bubble can be reduced by using an electron density up-ramp, which helps to counteract dephasing, and this alone can double the critical energy of the X-ray beam. However, a greater increase can be achieved by producing a sharp, tilted density gradient inside the density up-ramp. The tilted density gradient refracts the laser pulse transversely in the plasma, which effectively results in a transverse "kick" to the electrons, increasing r_β significantly [128]. As a result, the critical energy can be increased by an order of magnitude and smaller laser systems ($\sim$ 50 TW) can be used to produce X-ray beams with critical energy of up to 50 keV, which is useful for medical applications. It should be noted that no source size measurements were performed [128], and as r_β increases, the source size is expected to also increase. As in-line PCI requires a high transverse coherence, it remains to be seen whether this source is still suitable. Other PCI methods, such as crystal interferometry or analyser-based PCI require high monochromaticity and have less stringent requirements on the transverse coherency. These may be an option if the source becomes too large. These methods also differ in

terms of sensitivity, as the in-line PCI signal is proportional to the phase shift, while for analyser- or grating-based PCI, the signal is proportional to the refraction angle. This results in in-line PCI being more sensitive to higher spatial frequencies than the other methods. Furthermore, when including imaging resolution, it has been shown that the SNR for in-line PCI is $\propto 1/E^2$ while for analyser-based PCI it is $\propto 1/E$ [129]. Analyser-based PCI is thus preferable at higher photon energies.

PCI has many applications outside the medical field, such as the analysis of structural damage or strain in materials science [85, 130], inertial confinement fusion [131] and investigations on material coating [132]. PCI has been especially successful in analysing natural materials such as wood or paper, which consist of low-Z elements with little absorption, and porous materials such as bone [133].

In conclusion, there are many potential applications for PCI, be they clinical, industrial or in various research fields. Laser-plasma-based PCI can achieve the X-ray energy necessary using relatively small laser systems together with the required transverse coherence length. As mentioned above, most applications of laser-plasma accelerators will benefit greatly from an increase in repetition rate in the laser systems, and the same applies to PCI. Furthermore, the ability to tune the X-ray energy, possibly by controlling the plasma density gradients, will make laser-plasma-based X-ray sources more flexible.

The author's contributions

I **Optimization of soft X-ray phase-contrast tomography using a laser wakefield accelerator**
In this study, betatron X-rays produced in a gas cell by LWFA were optimized and used for phase-contrast tomography of a lacewing.
I was responsible for planning the experiment and jointly responsible for the set-up and data acquisition. I analysed the majority of the data and prepared the manuscript.

II **A focused very high energy electron beam for fractionated stereotactic radiotherapy**
An electron beam produced by LWFA was focused in a radiochromic phantom using quadrupoles to evaluate the performance for stereotactic radiotherapy. I was responsible for designing the experiment, jointly responsible for the set-up and data acquisition. I performed calibrations, analysed the data and prepared the manuscript.

III **Liquid mass distribution of transient sprays measured using laser-plasma-driven X-ray tomography**
LWFA-produced betatron X-rays were used to measure the 3D liquid mass distribution in a high-pressure fuel injector spray by performing a tomography, along with complimentary two-photon light induced fluorescence data. I partially designed and planned the experiment and was jointly responsible for the set-up and data acquisition. I performed preliminary data analysis, provided input for the later data analysis and was partially responsible for preparing the manuscript.

IV **Simultaneous laser-driven X-ray and two-photon fluorescence imaging of atomizing sprays**
X-rays produced using LWFA and a supersonic gas jet were used to image the spray from a commercial fuel port injector while simultaneously acquiring 2-photon light induced fluorescence data. I was jointly responsible for the set-up and data acquisition and provided feedback on the manuscript.

V **Low-divergence femtosecond X-ray pulses from a passive plasma lens**
In this study, a passive plasma lens was used to decrease the divergence of a LWFA-produced betatron X-ray beam by more than an order of magnitude in solid angle. I was responsible for analysing gas density measurements for the passive plasma lens along with the main supersonic gas jet and provided feedback on the manuscript.

VI **Enhanced laser-driven proton acceleration using nanowire targets**
This study showed that solid targets using nanowires on the front surface can enhance the maximum proton energies in target-normal sheath acceleration up to a factor of 2 by increasing the absorption of laser energy. I was jointly responsible for the set-up and data acquisition and participated in discussions on the design of the experiment.

Acknowledgements

I would like to start by expressing my gratitude to my supervisor Dr. Olle Lundh for his guidance throughout this work while simultaneously allowing me to work independently. I would also like to thank my co-supervisor Prof. Dr. Claes-Göran Wahlström for always being open to discussions and for posing constructive questions concerning the problems at hand.

I would like to thank my local colleagues for contributing to a wonderful working environment and all the lab work: Martin Hansson for his ability to generate interesting dinner conversations and having an innate ability to explain physics even to a toddler; Henrik Ekerfelt, for his trebuchet-building skills, his great sense of humour and his computer expertise whenever needed; Jonas Björklund Svensson, who has knowledge on the most obscure topics, great taste in music and an admirable attention to detail; Isabel Gallardo González, for showing me the ropes of the lab, for always smiling and radiating positivity; Diego Guénot, for showing me the ropes of the lab, again, after I forgot what Isabel had taught me, and being like a third supervisor. You were always quick to help me in the lab and you spent many late nights contributing to this work. You also inadvertently expanded my French vocabulary when things went wrong; Alexander Permogorov, who has at least two crazy ideas every day and is always fun to be around; Cornelia Gustafsson for her contagiously positive mood, and for being easy to work with; Erik Löfquist, who is always easy-going and funny; and last, but not least, I would like to thank my office-mate for these past 4 years, Giada Cantono. Thank you for readiness to discuss physics and to listen to my problems, for teaching me how to make a proper pizza and for becoming a great friend.

I would also like to thank Anders Persson for running the TW laser, along with teaching me laser physics along the way. No matter what I asked of him, he had it ready the next day.

When the laser failed after working hours, he always answered the phone and had an immediate solution.

I am also grateful for all the international collaborators I have been fortunate enough to meet and work with: Brigitte Cros, Chris Murphy, Matthew Streeter, Brendan Kettle, Nelson Lopes, Patrizio Antici, Francesco Filippi, Sandrine Dobosz Dufrénoy, Consoli Fabrizio, Lewis Dickson, Rob Shalloo, Christopher Underwood, Michael Backhouse, Gilles Maynard, Claudia Cobo, Martina Salvadori, Simon Vallieres, Andreoli Pierluigi, Lars Zigan, Michael Wensing, Hannah Ulrich and Bastian Lehnert.

I would also like to extended my gratitude to Dr. Edouard Berrocal at the Division of Combustion Physics, Lund University, for his expertise on fuel injectors and his great personality. He was always in a great mood and was easy to work with, even when I had figures named "setup_fig_version_39.pdf".

I would also like to thank Kristoffer Petersson for the discussions concerning radiotherapy and all the feedback, from which I learned so much.

Although they did not contribute directly to this thesis, I would like to thank my close friends as they helped to keep afloat; Kristoffer Olsson, Karl Falk, Fredrik Englund, Sebastian Hjort, Robin Jönsson, Dan Nilsson, Andreas Lövgren Dahl and Jimmie Hermansson.

I would also like to thank my family for all the support, Kerstin Hedin, Rolf Svendsen, Mikaela Svendsen and Sanne Svendsen.

Last but not least, I would like to thank my fiancée Madeleine Todor, for all her support throughout the years, despite still not knowing what I do. Thank you for taking care of our son Alexander, our dog, the house and everything else, especially during my absence on many late nights.

References

1. A. W. Chao. *2001 Snowmass Accelerator R and D Report* (2002).

2. T. Tajima and J. M. Dawson. *Laser Electron Accelerator.* Physical Review Letters **43**, 267–270 (1979).

3. D. Strickland and G. Mourou. *Compression of Amplified Chirped Optical Pulses.* Optics Communications **56**, 219–221 (1985).

4. E. Esarey, P. Sprangle, J. Krall and A. Ting. *Overview of Plasma-Based Accelerator Concepts.* IEEE Transactions on Plasma Science **24**, 252–288 (1996).

5. M. J. Hogan, C. D. Barnes, C. E. Clayton, F. J. Decker, S. Deng, P. Emma, C. Huang, R. H. Iverson, D. K. Johnson, C. Joshi, T. Katsouleas, P. Krejcik, W. Lu, K. A. Marsh, W. B. Mori, P. Muggli, C. L. O'Connell, E. Oz, R. H. Siemann and D. Walz. *Multi-GeV Energy Gain in a Plasma-Wakefield Accelerator.* Physical Review Letters **95**, 054802 (2005).

6. I. Blumenfeld, C. E. Clayton, F.-J. Decker, M. J. Hogan, C. Huang, R. Ischebeck, R. Iverson, C. Joshi, T. Katsouleas, N. Kirby, W. Lu, K. A. Marsh, W. B. Mori, P. Muggli, E. Oz, R. H. Siemann, D. Walz and M. Zhou. *Energy Doubling of 42 GeV Electrons in a Metre-Scale Plasma Wakefield Accelerator.* Nature **445**, 741–744 (2007).

7. A. Gonsalves, K. Nakamura, J. Daniels, C. Benedetti, C. Pieronek, T. de Raadt, S. Steinke, J. Bin, S. Bulanov, J. van Tilborg, C. Geddes, C. Schroeder, C. Tóth, E. Esarey, K. Swanson, L. Fan-Chiang, G. Bagdasarov, N. Bobrova, V. Gasilov, G. Korn, P. Sasorov and W. Leemans. *Petawatt Laser Guiding and Electron Beam Acceleration to 8 GeV in a Laser-Heated Capillary Discharge Waveguide*. Physical Review Letters **122**, 084801 (2019).

8. W. Leemans, A. Gonsalves, H.-S. Mao, K. Nakamura, C. Benedetti, C. Schroeder, C. Tóth, J. Daniels, D. Mittelberger, S. Bulanov, J.-L. Vay, C. Geddes and E. Esarey. *Multi-GeV Electron Beams From Capillary-Discharge-Guided Subpetawatt Laser Pulses in the Self-Trapping Regime*. Physical Review Letters **113**, 245002 (2014).

9. S. P. D. Mangles, A. G. R. Thomas, M. C. Kaluza, O. Lundh, F. Lindau, A. Persson, Z. Najmudin, C.-G. Wahlström, C. D. Murphy, C. Kamperidis, K. L. Lancaster, E. Divall and K. Krushelnick. *Effect of Laser Contrast Ratio on Electron Beam Stability in Laser Wakefield Acceleration Experiments*. Plasma Physics and Controlled Fusion **48**, B83–B90 (2006).

10. H. C. Kapteyn, A. Szoke, R. W. Falcone and M. M. Murnane. *Prepulse Energy Suppression for High-Energy Ultrashort Pulses Using Self-Induced Plasma Shuttering*. Optics Letters **16**, 490–492 (1991).

11. G. G. Scott, V. Bagnoud, C. Brabetz, R. J. Clarke, J. S. Green, R. I. Heathcote, H. W. Powell, B. Zielbauer, T. D. Arber, P. McKenna and D. Neely. *Optimization of Plasma Mirror Reflectivity and Optical Quality Using Double Laser Pulses*. New Journal of Physics **17**, 033027 (2015).

12. Y. Cai, W. Wang, C. Xia, J. Liu, L. Liu, C. Wang, Y. Xu, Y. Leng, R. Li and Z. Xu. *Time-Resolved Measurements on Reflectivity of an Ultrafast Laser-Induced Plasma Mirror*. Physics of Plasmas **16**, 103104 (2009).

13. G. Pretzier, H. Jäger, T. Neger, H. Philipp and J. Woisetschläger. *Comparison of Different Methods of Abel Inversion Using Computer Simulated and Experimental Side-On Data*. Zeitschrift für Naturforschung A **47**, 955–970 (1992).

14. L. Strüder. *High Speed Imaging and Spectroscopy with Low Energy X-Rays*. 1st edition, Springer International Publishing, 2016.

15. O. Lundh, Y. Ranebo and K. Svendsen. *Dosimetry in Environments Surrounding a Laser-Plasma Accelerator*. Strålsäkerhetsmyndigheten **4**, 2000–0456 (2019).

16. G. Battistoni, T. Boehlen, F. Cerutti, P. W. Chin, L. S. Esposito, A. Fassò, A. Ferrari, A. Lechner, A. Empl, A. Mairani, A. Mereghetti, P. G. Ortega, J. Ranft, S. Roesler, P. R. Sala, V. Vlachoudis and G. Smirnov. *Overview of the FLUKA Code*. Annals of Nuclear Energy **82**, 10–18 (2015).

17. T. Böhlen, F. Cerutti, M. Chin, A. Fassò, A. Ferrari, P. Ortega, A. Mairani, P. Sala, G. Smirnov and V. Vlachoudis. *The FLUKA Code: Developments and Challenges for High Energy and Medical Applications*. Nuclear Data Sheets **120**, 211–214 (2014).

18. A. Ferrari, P. Sala, A. Fasso and J. Ranft. *FLUKA: A Multi-Particle Transport Code*. CERN Yellow report **10** (2005).

19. V. Vlachoudis. *FLAIR: A Powerful but User Friendly Graphical Interface for FLUKA*. International Conference on Mathematics, Computational Methods & Reactor Physics (2009).

20. P. Mulser and D. Bauer. *High Power Laser-Matter Interaction*. 1st edition, Springer International Publishing, 2010.

21. E. Esarey, C. B. Schroeder and W. P. Leemans. *Physics of Laser-Driven Plasma-Based Electron Accelerators*. Reviews of Modern Physics **81**, 1229–1285 (2009).

22. P. Sprangle, E. Esarey and A. Ting. *Nonlinear Interaction of Intense Laser Pulses in Plasmas*. Physical Review A **41**, 4463–4469 (1990).

23. P. Sprangle, C.-M. Tang and E. Esarey. *Relativistic Self-Focusing of Short-Pulse Radiation Beams in Plasmas*. IEEE Transactions on Plasma Science **15**, 145–153 (1987).

24. C. Ren, B. J. Duda, R. G. Hemker, W. B. Mori, T. Katsouleas, T. M. Antonsen and P. Mora. *Compressing and Focusing a Short Laser Pulse by a Thin Plasma Lens*. Physical Review E **63**, 026411 (2001).

25. P. Mulser and D. Bauer. *High Power Laser-Matter Interaction*. 1st edition, Springer International Publishing, 2010.

26. F. Grossmann. *Theoretical Femtosecond Physics*. 1st edition, Springer International Publishing, 2013.

27. N. B. Delone and V. P. Krainov. *Tunneling and Barrier-Suppression Ionization of Atoms and Ions in a Laser Radiation Field*. Physics-Uspekhi **41**, 469–485 (1998).

28. W. Hill and C. Lee. *Light-Matter Interaction: Atoms and Molecules in External Fields and Nonlinear Optics*. 1st edition, John Wiley & Sons, Ltd, 2006.

29. E. Esarey and M. Pilloff. *Trapping and Acceleration in Nonlinear Plasma Waves*. Physics of Plasmas **2**, 1432–1436 (1995).

30. M. R. Islam, E. Brunetti, R. P. Shanks, B. Ersfeld, R. C. Issac, S. Cipiccia, M. P. Anania, G. H. Welsh, S. M. Wiggins, A. Noble, R. A. Cairns, G. Raj and D. A. Jaroszynski. *Near-Threshold Electron Injection in the Laser–Plasma Wakefield Accelerator Leading to Femtosecond Bunches*. New Journal of Physics **17**, 093033 (2015).

31. S. Kalmykov, S. A. Yi, V. Khudik and G. Shvets. *Electron Self-Injection and Trapping Into an Evolving Plasma Bubble*. Physical Review Letters **103**, 135004 (2009).

32. A. G. R. Thomas. *Scalings for Radiation From Plasma Bubbles*. Physics of Plasmas **17**, 056708 (2010).

33. I. Kostyukov, A. Pukhov and S. Kiselev. *Phenomenological Theory of Laser-Plasma Interaction in "Bubble" Regime*. Physics of Plasmas **11**, 5256–5264 (2004).

34. A. Pukhov and J. M. ter Vehn. *Laser Wake Field Acceleration: The Highly Non-linear Broken-Wave Regime*. Applied Physics B: Lasers and Optics **74**, 355–361 (2002).

35. S. P. D. Mangles, G. Genoud, M. S. Bloom, M. Burza, Z. Najmudin, A. Persson, K. Svensson, A. G. R. Thomas and C.-G. Wahlström. *Self-Injection Threshold in Self-Guided Laser Wakefield Accelerators*. Physical Review Special Topics - Accelerators and Beams **15**, 011302 (2012).

36. M. Chen, Z.-M. Sheng, Y.-Y. Ma and J. Zhang. *Electron Injection and Trapping in a Laser Wakefield by Field Ionization to High-Charge States of Gases.* Journal of Applied Physics **99**, 056109 (2006).

37. A. Buck, J. Wenz, J. Xu, K. Khrennikov, K. Schmid, M. Heigoldt, J. M. Mikhailova, M. Geissler, B. Shen, F. Krausz, S. Karsch and L. Veisz. *Shock-Front Injector for High-Quality Laser-Plasma Acceleration.* Physical Review Letters **110**, 185006 (2013).

38. K. Schmid, A. Buck, C. M. S. Sears, J. M. Mikhailova, R. Tautz, D. Herrmann, M. Geissler, F. Krausz and L. Veisz. *Density-Transition Based Electron Injector for Laser Driven Wakefield Accelerators.* Physical Review Special Topics - Accelerators and Beams **13**, 091301 (2010).

39. C. Thaury, E. Guillaume, A. Lifschitz, K. T. Phuoc, M. Hansson, G. Grittani, J. Gautier, J.-P. Goddet, A. Tafzi, O. Lundh and V. Malka. *Shock Assisted Ionization Injection in Laser-Plasma Accelerators.* Scientific Reports **5**, 16310 (2015).

40. B. A. Shadwick, C. B. Schroeder and E. Esarey. *Nonlinear Laser Energy Depletion in Laser-Plasma Accelerators.* Physics of Plasmas **16**, 056704 (2009).

41. W. Lu, M. Tzoufras, C. Joshi, F. S. Tsung, W. B. Mori, J. Vieira, R. A. Fonseca and L. O. Silva. *Generating Multi-GeV Electron Bunches Using Single Stage Laser Wakefield Acceleration in a 3D Nonlinear Regime.* Physical Review Special Topics - Accelerators and Beams **10**, 061301 (2007).

42. H. Nakanishi, Y. Yoshida, T. Ueda, T. Kozawa, H. Shibata, K. Nakajima, T. Kurihara, N. Yugami, Y. Nishida, T. Kobayashi, A. Enomoto, T. Oogoe, H. Kobayashi, B. S. Newberger, S. Tagawa, K. Miya and A. Ogata. *Direct Observation of Plasma-Lens Effect.* Physical Review Letters **66**, 1870–1873 (1991).

43. C. Thaury, E. Guillaume, A. Döpp, R. Lehe, A. Lifschitz, K. T. Phuoc, J. Gautier, J.-P. Goddet, A. Tafzi, A. Flacco, F. Tissandier, S. Sebban, A. Rousse and V. Malka. *Demonstration of Relativistic Electron Beam Focusing by a Laser-Plasma Lens.* Nature Communications **6**, 6860 (2015).

44. W. Lu, C. Huang, M. Zhou, M. Tzoufras, F. S. Tsung, W. B. Mori and T. Katsouleas. *A Nonlinear Theory for Multidimensional Relativistic Plasma Wave Wakefields.* Physics of Plasmas **13**, 056709 (2006).

45. X. Xu, J. Hua, Y. Wu, C. Zhang, F. Li, Y. Wan, C.-H. Pai, W. Lu, W. An, P. Yu, M. Hogan, C. Joshi and W. Mori. *Physics of Phase Space Matching for Staging Plasma and Traditional Accelerator Components Using Longitudinally Tailored Plasma Profiles.* Physical Review Letters **116**, 124801 (2016).

46. J. van Tilborg, S. Steinke, C. Geddes, N. Matlis, B. Shaw, A. Gonsalves, J. Huijts, K. Nakamura, J. Daniels, C. Schroeder, C. Benedetti, E. Esarey, S. Bulanov, N. Bobrova, P. Sasorov and W. Leemans. *Active Plasma Lensing for Relativistic Laser-Plasma-Accelerated Electron Beams.* Physical Review Letters **115**, 184802 (2015).

47. E. B. Podgorsak. *Radiation Physics for Medical Physicists.* 2nd edition, Springer International Publishing, 2010.

48. M. J. Berger, M. Inokuti, H. H. Anderson, H. Bichsel, J. A. Dennis, D. Powers, S. M. Seltzer and J. E. Turner. *Report 37.* Journal of the International Commission on Radiation Units and Measurements **os19** (1984).

49. International Atomic Energy Agency. *Directory of Radiotherapy Centres* (Accessed on: 2021-12-16). URL `https://dirac.iaea.org`.

50. L. Papiez, C. DesRosiers and V. Moskvin. *Very High Energy Electrons (50 – 250 MeV) and Radiation Therapy.* Technology in Cancer Research & Treatment **1**, 105–110 (2002).

51. A. Lagzda, D. Angal-Kalinin, J. Jones, A. Aitkenhead, K. J. Kirkby, R. MacKay, M. V. Herk, W. Farabolini, S. Zeeshan and R. M. Jones. *Influence of Heterogeneous Media on Very High Energy Electron (VHEE) Dose Penetration and a Monte Carlo-Based Comparison with Existing Radiotherapy Modalities.* Nuclear Instruments and Methods in Physics Research Section B: Beam Interactions with Materials and Atoms **482**, 70–81 (2020).

52. K. Kokurewicz, E. Brunetti, G. H. Welsh, S. M. Wiggins, M. Boyd, A. Sorensen, A. J. Chalmers, G. Schettino, A. Subiel, C. DesRosiers and D. A. Jaroszynski. *Focused Very High-Energy Electron Beams as a Novel Radiotherapy Modality for Producing High-Dose Volumetric Elements.* Scientific Reports **9**, 10837 (2019).

53. L. Whitmore, R. I. Mackay, M. van Herk, J. K. Jones and R. M. Jones. *Focused VHEE (Very High Energy Electron) Beams and Dose Delivery for Radiotherapy Applications.* Scientific Reports **11**, 14013 (2021).

54. C. DesRosiers, V. Moskvin, M. Cao, C. Joshi and M. Langer. *Lung Tumor Treatment with Very High Energy Electron Beams of 150-250 MeV as Compared to Conventional Megavoltage Photon Beams.* International Journal of Radiation Oncology, Biology, Physics **72**, S612 (2008).

55. E. Schüler, K. Eriksson, E. Hynning, S. L. Hancock, S. M. Hiniker, M. Bazalova-Carter, T. Wong, Q.-T. Le, B. W. J. Loo and P. G. Maxim. *Very High-Energy Electron (VHEE) Beams in Radiation Therapy; Treatment Plan Comparison Between VHEE, VMAT, and PPBS.* Medical Physics **44**, 2544–2555 (2017).

56. C. DesRosiers, V. Moskvin, M. Cao, C. J. Joshi and M. Langer. *Laser-Plasma Generated Very High Energy Electrons in Radiation Therapy of the Prostate.* In *Commercial and Biomedical Applications of Ultrafast Lasers VIII* volume 6881 pages 49 – 62. International Society for Optics and Photonics SPIE (2008).

57. T. Fuchs, H. Szymanowski, U. Oelfke, Y. Glinec, C. Rechatin, J. Faure and V. Malka. *Treatment Planning for Laser-Accelerated Very-High Energy Electrons.* Physics in Medicine and Biology **54**, 3315—3328 (2009).

58. O. Lundh, C. Rechatin, J. Faure, A. Ben-Ismaïl, J. Lim, C. D. Wagter, W. D. Neve and V. Malka. *Comparison of Measured with Calculated Dose Distribution From a 120-MeV Electron Beam From a Laser-Plasma Accelerator.* Medical Physics **39**, 3501–3508 (2012).

59. E. Y. L. Marroquin, J. A. H. González, M. A. C. López, J. E. V. Barajas and O. A. García-Garduño. *Evaluation of the Uncertainty in an EBT3 Film Dosimetry System Utilizing Net Optical Density.* Journal of Applied Clinical Medical Physics **17**, 466–481 (2016).

60. *Accuracy Requirements and Uncertainties in Radiotherapy.* Number 31 in Human Health Series. 1st edition, International Atomic Energy Agency, 2016.

61. E. Esarey, B. A. Shadwick, P. Catravas and W. P. Leemans. *Synchrotron Radiation From Electron Beams in Plasma-Focusing Channels.* Physical Review E **65**, 056505 (2002).

62. J. Rafelski. *Relativity Matters, From Einstein's EMC2 to Laser Particle Acceleration and Quark-Gluon Plasma.* 1st edition, Springer International Publishing, 2017.

63. J. C. Wood. *Betatron Radiation From Laser Wakefield Accelerators and Its Applications.* Imperial College, London, 2017.

64. S. Corde, K. T. Phuoc, G. Lambert, R. Fitour, V. Malka, A. Rousse, A. Beck and E. Lefebvre. *Femtosecond X Rays From Laser-Plasma Accelerators.* Reviews of Modern Physics **85**, 1–48 (2013).

65. O. Lundh, J. Lim, C. Rechatin, L. Ammoura, A. Ben-Ismaïl, X. Davoine, G. Gallot, J.-P. Goddet, E. Lefebvre, V. Malka and J. Faure. *Few Femtosecond, Few Kiloampere Electron Bunch Produced by a Laser–Plasma Accelerator.* Nature Physics **7**, 219–222 (2011).

66. P. Kirkpatrick. *Theory and Use of Ross Filters. II.* Review of Scientific Instruments **15**, 223–229 (1944).

67. S. Fourmaux, S. Corde, K. T. Phuoc, P. M. Leguay, S. Payeur, P. Lassonde, S. Gnedyuk, G. Lebrun, C. Fourment, V. Malka, S. Sebban, A. Rousse and J. C. Kieffer. *Demonstration of the Synchrotron-Type Spectrum of Laser-Produced Betatron Radiation.* New Journal of Physics **13**, 033017 (2011).

68. I. N. Tilikin, T. A. Shelkovenko, S. A. Pikuz and D. A. Hammer. *Determination of the Size of a Radiation Source by the Method of Calculation of Diffraction Patterns.* Optics and Spectroscopy **115**, 128–136 (2013).

69. I. G. González, H. Ekerfelt, M. Hansson, T. L. Audet, B. Aurand, F. G. Desforges, S. D. Dufrénoy, A. Persson, X. Davoine, C.-G. Wahlström, B. Cros and O. Lundh. *Effects of the Dopant Concentration in Laser Wakefield and Direct Laser Acceleration of Electrons.* New Journal of Physics **20**, 053011 (2018).

70. E. Kristensson, E. Berrocal and M. Aldén. *Quantitative 3D Imaging of Scattering Media Using Structured Illumination and Computed Tomography.* Optics Express **20**, 14437–14450 (2012).

71. W. Cai, C. F. Powell, Y. Yue, S. Narayanan, J. Wang, M. W. Tate, M. J. Renzi, A. Ercan, E. Fontes and S. M. Gruner. *Quantitative Analysis of Highly Transient Fuel Sprays by Time-Resolved X-Radiography.* Applied Physics Letters **83**, 1671–1673 (2003).

72. X. Liu, K.-S. Im, Y. Wang, J. Wang, M. W. Tate, A. Ercan, D. R. Schuette and S. M. Gruner. *Four Dimensional Visualization of Highly Transient Fuel Sprays by Microsecond Quantitative X-Ray Tomography.* Applied Physics Letters **94**, 084101 (2009).

73. A. Tekawade, B. A. Sforzo, K. E. Matusik, K. Fezzaa, A. L. Kastengren and C. F. Powell. *Time-Resolved 3D Imaging of Two-Phase Fluid Flow Inside a Steel Fuel Injector Using Synchrotron X-Ray Tomography.* Scientific Reports **10**, 8674 (2020).

74. K. Palikaras and N. Tavernarakis. *Multiphoton Fluorescence Light Microscopy.* In eLS, John Wiley & Sons, Ltd, 2015.

75. J. Hsieh. *Computed Tomography Principles, Design, Artifacts, and Recent Advances.* 2nd edition, John Wiley & Sons, Ltd, 2009.

76. R. Bracewell. *Strip Integration in Radio Astronomy.* Australian Journal of Physics **9**, 198 (1956).

77. P. Grangeat. *Tomography.* 1st edition, John Wiley & Sons, Ltd, 2009.

78. A. Buades, B. Coll and J.-M. Morel. *A Non-local Algorithm for Image Denoising.* In *2005 IEEE Computer Society Conference on Computer Vision and Pattern Recognition (CVPR'05)* volume 2 pages 60–65 (2005).

79. D. Paganin, S. C. Mayo, T. E. Gureyev, P. R. Miller and S. W. Wilkins. *Simultaneous Phase and Amplitude Extraction From a Single Defocused Image of a Homogeneous Object.* Journal of Microscopy **206**, 33–40 (2002).

80. C. David, B. Nöhammer, H. H. Solak and E. Ziegler. *Differential X-Ray Phase Contrast Imaging Using a Shearing Interferometer.* Applied Physics Letters **81**, 3287–3289 (2002).

81. R. Fitzgerald. *Phase-Sensitive X-Ray Imaging.* Physics Today **53**, 23–26 (2000).

82. H. Miao, A. Panna, A. A. Gomella, E. E. Bennett, S. Znati, L. Chen and H. Wen. *A Universal Moiré Effect and Application in X-Ray Phase-Contrast Imaging.* Nature Physics **12**, 830–834 (2016).

83. S. W. Wilkins, T. E. Gureyev, D. Gao, A. Pogany and A. W. Stevenson. *Phase-Contrast Imaging Using Polychromatic Hard X-Rays.* Nature **384**, 335–338 (1996).

84. A. Burvall, U. Lundström, P. A. C. Takman, D. H. Larsson and H. M. Hertz. *Phase Retrieval in X-Ray Phase-Contrast Imaging Suitable for Tomography.* Optics Express **19**, 10359–10376 (2011).

85. P. Cloetens, M. Pateyron-Salomé, J. Y. Buffière, G. Peix, J. Baruchel, F. Peyrin and M. Schlenker. *Observation of Microstructure and Damage in Materials by Phase Sensitive Radiography and Tomography.* Journal of Applied Physics **81**, 5878–5886 (1997).

86. S. Kneip, C. McGuffey, F. Dollar, M. S. Bloom, V. Chvykov, G. Kalintchenko, K. Krushelnick, A. Maksimchuk, S. P. D. Mangles, T. Matsuoka, Z. Najmudin, C. A. J. Palmer, J. Schreiber, W. Schumaker, A. G. R. Thomas and V. Yanovsky. *X-Ray Phase Contrast Imaging of Biological Specimens with Femtosecond Pulses of Betatron Radiation From a Compact Laser Plasma Wakefield Accelerator.* Applied Physics Letters **99**, 093701 (2011).

87. J. Wenz, S. Schleede, K. Khrennikov, M. Bech, P. Thibault, M. Heigoldt, F. Pfeiffer and S. Karsch. *Quantitative X-Ray Phase-Contrast Microtomography From a Compact Laser-Driven Betatron Source.* Nature Communications **6**, 7568 (2015).

88. A. Macchi, M. Borghesi and M. Passoni. *Ion Acceleration by Superintense Laser-Plasma Interaction.* Reviews of Modern Physics **85**, 751–793 (2013).

89. H. Daido, M. Nishiuchi and A. S. Pirozhkov. *Review of Laser-Driven Ion Sources and Their Applications.* Reports on Progress in Physics **75**, 056401 (2012).

90. B. C. Baumann, N. Mitra, J. G. Harton, Y. Xiao, A. P. Wojcieszynski, P. E. Gabriel, H. Zhong, H. Geng, A. Doucette, J. Wei, P. J. O'Dwyer, J. E. Bekelman and J. M. Metz. *Comparative Effectiveness of Proton vs Photon Therapy as Part of Concurrent Chemoradiotherapy for Locally Advanced Cancer.* JAMA Oncology **6**, 237–246 (2020).

91. A. Pompos, M. Durante and H. Choy. *Heavy Ions in Cancer Therapy.* JAMA Oncology **2**, 1539–1540 (2016).

92. O. Mohamad, B. Sishc, J. Saha, A. Pompos, A. Rahimi, M. Story, A. Davis and D. Kim. *Carbon Ion Radiotherapy: A Review of Clinical Experiences and Preclinical Research, with an Emphasis on DNA Damage/Repair.* Cancers **9**, 66 (2017).

93. N. P. Brodin, R. Kabarriti, C. B. Schechter, M. Pankuch, V. Gondi, S. Kalnicki, M. K. Garg and W. A. Tomé. *Individualized Quality of Life Benefit and Cost-Effectiveness Estimates of Proton Therapy for Patients with Oropharyngeal Cancer.* Radiation Oncology **16**, 19 (2021).

94. A. Courdi, J.-P. Caujolle, J.-D. Grange, L. Diallo-Rosier, J. Sahel, F. Bacin, C. Zur, P. Gastaud, N. Iborra-Brassart, J. Hérault and P. Chauvel. *Results of Proton Therapy of Uveal Melanomas Treated in Nice.* International Journal of Radiation Oncology*Biology*Physics **45**, 5–11 (1999).

95. E. S. Gragoudas. *Proton Beam Irradiation of Uveal Melanomas: The First 30 Years The Weisenfeld Lecture.* Investigative Ophthalmology & Visual Science **47**, 4666–4673 (2006).

96. E. Sengbusch, A. Pérez-Andújar, P. M. DeLuca and T. R. Mackie. *Maximum Proton Kinetic Energy and Patient-Generated Neutron Fluence Considerations in Proton Beam Arc Delivery Radiation Therapy.* Medical Physics **36**, 364–372 (2009).

97. Y. Ping, R. Shepherd, B. F. Lasinski, M. Tabak, H. Chen, H. K. Chung, K. B. Fournier, S. B. Hansen, A. Kemp, D. A. Liedahl, K. Widmann, S. C. Wilks, W. Rozmus and M. Sherlock. *Absorption of Short Laser Pulses on Solid Targets in the Ultrarelativistic Regime.* Physical Review Letters **100**, 085004 (2008).

98. A. R. Bell, A. P. L. Robinson, M. Sherlock, R. J. Kingham and W. Rozmus. *Fast Electron Transport in Laser-Produced Plasmas and the KALOS Code for Solution of the Vlasov–Fokker–Planck Equation*. Plasma Physics and Controlled Fusion **48**, R37–R57 (2006).

99. M. Roth and M. Schollmeier. *Ion Acceleration-Target Normal Sheath Acceleration*. CERN Yellow Report **2016-001**, 231–270 (2017).

100. J. P. Freidberg, R. W. Mitchell, R. L. Morse and L. I. Rudsinski. *Resonant Absorption of Laser Light by Plasma Targets*. Physical Review Letters **28**, 795–799 (1972).

101. K. Estabrook and W. L. Kruer. *Properties of Resonantly Heated Electron Distributions*. Physical Review Letters **40**, 42–45 (1978).

102. P. Gibbon and A. R. Bell. *Collisionless Absorption in Sharp-Edged Plasmas*. Physical Review Letters **68**, 1535–1538 (1992).

103. W. L. Kruer and K. Estabrook. *J×B Heating by Very Intense Laser Light*. Physics of Fluids **28**, 430–432 (1985).

104. D. Guénot, D. Gustas, A. Vernier, B. Beaurepaire, F. Böhle, M. Bocoum, M. Lozano, A. Jullien, R. Lopez-Martens, A. Lifschitz and J. Faure. *Relativistic Electron Beams Driven by Khz Single-Cycle Light Pulses*. Nature Photonics **11**, 293–296 (2017).

105. A. Giesen, H. Hügel, A. Voss, K. Wittig, U. Brauch and H. Opower. *Scalable Concept for Diode-Pumped High-Power Solid-State Lasers*. Applied Physics B **58**, 365–372 (1994).

106. C. Herkommer, P. Krötz, S. Klingebiel, C. Wandt, D. Bauer, K. Michel, R. Kienberger and T. Metzger. *Towards a Joule-Class Ultrafast Thin-Disk Based Amplifier at Kilohertz Repetition Rate*. In *Conference on Lasers and Electro-Optics* page SM4E.3. Optical Society of America (2019).

107. O. Jakobsson, S. Hooker and R. Walczak. *GeV-Scale Accelerators Driven by Plasma-Modulated Pulses From Kilohertz Lasers*. Physical Review Letters **127**, 184801 (2021).

108. V. Favaudon, L. Caplier, V. Monceau, F. Pouzoulet, M. Sayarath, C. Fouillade, M.-F. Poupon, I. Brito, P. Hupé, J. Bourhis, J. Hall, J.-J. Fontaine and M.-C. Vozenin. *Ultrahigh Dose-Rate Flash Irradiation Increases the Differential Response Between Normal and Tumor Tissue in Mice.* Science Translational Medicine **6**, 245ra93 (2014).

109. S. Field and D. Bewley. *Effects of Dose-rate on the Radiation Response of Rat Skin.* International Journal of Radiation Biology and Related Studies in Physics, Chemistry and Medicine **26**, 259–267 (1974).

110. P. Montay-Gruel, K. Petersson, M. Jaccard, G. Boivin, J.-F. Germond, B. Petit, R. Doenlen, V. Favaudon, F. Bochud, C. Bailat, J. Bourhis and M.-C. Vozenin. *Irradiation in a Flash: Unique Sparing of Memory in Mice After Whole Brain Irradiation with Dose Rates Above 100 Gy/s.* Radiotherapy and Oncology **124**, 365–369 (2017).

111. M. Oppelt, M. Baumann, R. Bergmann, E. Beyreuther, K. Brüchner, J. Hartmann, L. Karsch, M. Krause, L. Laschinsky, E. Leßmann, M. Nicolai, M. Reuter, C. Richter, A. Sävert, M. Schnell, M. Schürer, J. Woithe, M. Kaluza and J. Pawelke. *Comparison Study of in Vivo Dose Response to Laser-Driven Versus Conventional Electron Beam.* Radiation and Environmental Biophysics **54**, 155–166 (2015).

112. E. Beyreuther, M. Brand, S. Hans, K. Hideghéty, L. Karsch, E. Leßmann, M. Schürer, E. R. Szabó and J. Pawelke. *Feasibility of Proton Flash Effect Tested by Zebrafish Embryo Irradiation.* Radiotherapy and Oncology **139**, 46–50 (2019).

113. L. M. L. Smyth, J. F. Donoghue, J. A. Ventura, J. Livingstone, T. Bailey, L. R. J. Day, J. C. Crosbie and P. A. W. Rogers. *Comparative Toxicity of Synchrotron and Conventional Radiation Therapy Based on Total and Partial Body Irradiation in a Murine Model.* Scientific Reports **8**, 12044 (2018).

114. J. D. Wilson, E. M. Hammond, G. S. Higgins and K. Petersson. *Ultra-High Dose Rate (FLASH) Radiotherapy: Silver Bullet or Fool's Gold?* Frontiers in Oncology **9**, 1563 (2020).

115. M. Lempart, B. Blad, G. Adrian, S. Bäck, T. Knöös, C. Ceberg and K. Petersson. *Modifying a Clinical Linear Accelerator for Delivery of Ultra-High Dose Rate Irradiation*. Radiotherapy and Oncology **139**, 40–45 (2019).

116. J. P. Couperus, R. Pausch, A. Köhler, O. Zarini, J. M. Krämer, M. Garten, A. Huebl, R. Gebhardt, U. Helbig, S. Bock, K. Zeil, A. Debus, M. Bussmann, U. Schramm and A. Irman. *Demonstration of a Beam Loaded Nanocoulomb-Class Laser Wakefield Accelerator*. Nature Communications **8**, 487 (2017).

117. J. Götzfried, A. Döpp, M. Gilljohann, F. Foerster, H. Ding, S. Schindler, G. Schilling, A. Buck, L. Veisz and S. Karsch. *Physics of High-Charge Electron Beams in Laser-Plasma Wakefields*. Physical Review X **10**, 041015 (2020).

118. F. Albert, M. E. Couprie, A. Debus, M. C. Downer, J. Faure, A. Flacco, L. A. Gizzi, T. Grismayer, A. Huebl, C. Joshi, M. Labat, W. P. Leemans, A. R. Maier, S. P. D. Mangles, P. Mason, F. Mathieu, P. Muggli, M. Nishiuchi, J. Osterhoff, P. P. Rajeev, U. Schramm, J. Schreiber, A. G. R. Thomas, J.-L. Vay, M. Vranic and K. Zeil. *2020 Roadmap on Plasma Accelerators*. New Journal of Physics **23**, 031101 (2021).

119. M. McManus, F. Romano, N. D. Lee, W. Farabolini, A. Gilardi, G. Royle, H. Palmans and A. Subiel. *The Challenge of Ionisation Chamber Dosimetry in Ultra-Short Pulsed High Dose-Rate Very High Energy Electron Beams*. Scientific Reports **10**, 9089 (2020).

120. A. Subiel, V. Moskvin, G. H. Welsh, S. Cipiccia, D. Reboredo, C. DesRosiers and D. A. Jaroszynski. *Challenges of Dosimetry of Ultra-Short Pulsed Very High Energy Electron Beams*. Physica Medica **42**, 327–331 (2017).

121. Z. Cao, F. Jin, J. Dong, Z. Yang, X. Zhan, Z. Yuan, H. Zhang, S. Jiang and Y. Ding. *Soft X-Ray Low-Pass Filter with a Square-Pore Microchannel Plate*. Optics Letters **38**, 1509–1511 (2013).

122. A. Bravin, P. Coan and P. Suortti. *X-Ray Phase-Contrast Imaging: From Pre-clinical Applications Towards Clinics*. Physics in Medicine and Biology **58**, R1–R35 (2013).

123. E. Castelli, M. Tonutti, F. Arfelli, R. Longo, E. Quaia, L. Rigon, D. Sanabor, F. Zanconati, D. Dreossi, A. Abrami, E. Quai, P. Bregant, K. Casarin, V. Chenda, R. H. Menk, T. Rokvic, A. Vascotto, G. Tromba and M. A. Cova. *Mammography with Synchrotron Radiation: First Clinical Experience with Phase-Detection Technique.* Radiology **259**, 684–694 (2011).

124. L. Brombal. *X-Ray Phase-Contrast Tomography.* 1st edition, Springer International Publishing, 2020.

125. P. Coan, F. Bamberg, P. C. Diemoz, A. Bravin, K. Timpert, E. Mützel, J. G. Raya, S. Adam-Neumair, M. F. Reiser and C. Glaser. *Characterization of Osteoarthritic and Normal Human Patella Cartilage by Computed Tomography X-Ray Phase-Contrast Imaging.* Investigative Radiology **45**, 437–444 (2010).

126. J. M. Cole, J. C. Wood, N. C. Lopes, K. Poder, R. L. Abel, S. Alatabi, J. S. J. Bryant, A. Jin, S. Kneip, K. Mecseki, D. R. Symes, S. P. D. Mangles and Z. Najmudin. *Laser-Wakefield Accelerators as Hard X-Ray Sources for 3D Medical Imaging of Human Bone.* Scientific Reports **5**, 13244 (2015).

127. X. Wang, R. Zgadzaj, N. Fazel, Z. Li, S. A. Yi, X. Zhang, W. Henderson, Y.-Y. Chang, R. Korzekwa, H.-E. Tsai, C.-H. Pai, H. Quevedo, G. Dyer, E. Gaul, M. Martinez, A. C. Bernstein, T. Borger, M. Spinks, M. Donovan, V. Khudik, G. Shvets, T. Ditmire and M. C. Downer. *Quasi-Monoenergetic Laser-Plasma Acceleration of Electrons to 2 GeV.* Nature Communications **4**, 1988 (2013).

128. M. Kozlova, I. Andriyash, J. Gautier, S. Sebban, S. Smartsev, N. Jourdain, U. Chulagain, Y. Azamoum, A. Tafzi, J.-P. Goddet, K. Oubrerie, C. Thaury, A. Rousse and K. T. Phuoc. *Hard X Rays from Laser-Wakefield Accelerators in Density Tailored Plasmas.* Physical Review X **10**, 011061 (2020).

129. P. C. Diemoz, A. Bravin and P. Coan. *Theoretical Comparison of Three X-Ray Phase-Contrast Imaging Techniques: Propagation-Based Imaging, Analyzer-Based Imaging and Grating Interferometry.* Optics Express **20**, 2789–2805 (2012).

130. J.-Y. Buffière, E. Maire, P. Cloetens, G. Lormand and R. Fougères. *Characterization of Internal Damage in a MMCp Using X-Ray Synchrotron Phase Contrast Microtomography.* Acta Materialia **47**, 1613–1625 (1999).

131. S. Fourmaux, E. Hallin, A. Krol, J. L. Bourgade and J. C. Kieffer. *X-Ray Phase Contrast Imaging of Spherical Capsules*. Optics Express **28**, 13978–13990 (2020).

132. Y. S. Kashyap, A. Agrawal, P. Sarkar, M. Shukla, T. Roy and A. Sinha. *Study of Pyro-Carbon Coated Alumina Kernel Using Mixed Contrast Transfer Based X-Ray Phase Retrieval Technique*. NDT & E International **44**, 41–46 (2011).

133. S. C. Mayo, A. W. Stevenson and S. W. Wilkins. *In-Line Phase-Contrast X-ray Imaging and Tomography for Materials Science*. Materials **5**, 937–965 (2012).